Fabrication and analysis of nanostructures in the quantum material $SrRuO_3$

Gennadii Laskin

Max Planck Institut für Festkörperforschung
Universität Stuttgart
2019

Fabrication and analysis of nanostructures in the quantum material $SrRuO_3$

Von der Fakultät Mathematik und Physik der Universität Stuttgart
zur Erlangung der Würde eines Doktors
der Naturwissenschaften (Dr. rer. nat.) genehmigte Abhandlung

Vorgelegt von
Gennadii Laskin
aus Tyumen, Russland

Hauptberichter:	Prof. Dr. Jochen Mannhart
Mitberichter:	Prof. Dr. Martin Dressel
Tag der mündlichen Prüfung:	18.11.2019

Max Planck Institut für Festkörperforschung
Universität Stuttgart
2019

Contents

List of Abbreviations

AFM - Atomic Force Microscopy

DFT - Density Functional Theory

EBL - Electron Beam Lithography

EDX - Energy-dispersive X-ray analysis

MBE - Molecular Beam Epitaxy

MPMS - Magnetic Properties Measurement System

PLD - Pulsed Laser Deposition

PMMA - Poly(methyl methacrylate)

PPMS - Physical Properties Measurement System

RHEED - Reflection High-Energy Electron Diffraction

RSM - Reciprocal Space Map

RSO - Reciprocating Sample Option

SEM - Scanning Electron Microscopy

SQUID - Superconducting Quantum Interference Device

STEM - Scanning Transmission Electron Microscopy

TEM - Transmission Electron Microscopy

UHV - Ultra-high vacuum

VSM - Vibrating-Sample Magnetometer

XRD - X-Ray Diffraction

Zusammenfassung

Der nanoskalige Einschluss von Materialien in einer oder mehreren Dimensionen ermöglicht die Realisierung von Eigenschaften, die in anderen Substanzen in der Natur nicht existieren. Es macht solche Objekte als Systeme zur Untersuchung neuer physikalischer Effekte und für mögliche Anwendungen in Geräten äußerst interessant. Neue Perspektiven auf diesem Gebiet ergeben sich, wenn man die Verwendung von Materialien mit inhärent korrelierten Elektronensystemen in Betracht zieht. Diese Substanzen besitzen sogar im ausgedehnten dreidimensionelen Körper reiche Phasendiagramme mit einer Vielzahl konkurrierender Grundzustände. Es wird erwartet, dass die Fülle der funktionellen Eigenschaften die Physik von Nanoobjekten bereichert, die aus solchen Materialien hergestellt werden. In dieser Arbeit verwende ich das Top-Down-Prinzip, um 0D- und 1D-beschränkte Nanostrukturen aus korreliertem ferromagnetischem metallischem Perowskit $SrRuO_3$ zu erstellen und zu untersuchen. Ein besonderer Schwerpunkt liegt auf der Modifikation der magnetischen Eigenschaften, die beim Einschluss der Dünnschicht in die nanostrukturierte Form passiert.

In Kapitel 3, das die Grundlage für diese Forschung darstellt, entwickle ich die Technologie zur Strukturierung komplexer epitaktisch gewachsener Heteroschichten. Durch eine Kombination aus Elektronenstrahllithographie und Trockenätzen mit Ar-Ionen ist es mir gelungen, Nanostrukturen mit Größen kleiner 20 nm herzustellen, die für diese Materialklasse bisher unerreicht waren. Das Top-Down-Prinzip ermöglicht die Erzeugung von Nanostrukturen mit beliebigen Konfigurationen und Formen. Gleichzeitig bietet die Stabilität des Prozesses die Möglichkeit, große Flächen mit bis zu mehreren Milliarden Elementen pro Probe zu strukturieren.

Das zweite Highlight des dritten Kapitels ist die Optimierung der Wachstumsbedingungen von $SrRuO_3$ auf (100) $SrTiO_3$, um mittels Laserstrahlverdampfens als Wachstumstechnik die höchstmögliche Materialqualität zu erzielen. Wir implementieren eine neu entwickelte Technologie des *in situ* thermischen Temperns, um die Substratoberfläche für das epitaktische Wachstum vorzubereiten. Die Technologie ermöglicht eine höhere Qualität und bessere Reproduzierbarkeit des gewachsenen Materials im Vergleich zur üblicherweise verwendeten chemischen Behandlung von Substraten.

Die Eigenschaften sowohl der ursprünglichen Dünnschichten als auch der Nanopunkten von $SrRuO_3$ werden in Kapitel 4 mit verschiedenen Methoden untersucht. Ich zeige, dass die Qualität unserer Dünnschichten mit den besten Schichten in der Literatur vergleichbar ist oder diese sogar übertrifft. Nach den Strukturierungsprozessen behält das Material die epitaktische Struktur bei und entwickelt keine sichtbaren Defekte oder toten Schichten bis zu Strukturgrößen von 30 nm. Dieses Ergebnis ist entscheidend, da es beweist, dass Epitaxieschichten aus komplexen Materialien auf solch kleinen Skalen strukturiert werden können, während die strukturelle Integrität erhalten bleibt.

Die Ergebnisse der SQUID-Magnetometrie an den Nanopunkte werden in Kapitel 5 vorgestellt. Ich zeige, dass sich die magnetischen Eigenschaften von $SrRuO_3$ nach der Strukturierung in vielerlei Hinsicht ändern werden. Ein faszinierender Effekt ist die Erhöhung der Curie-Temperatur T_C des ferromagnetischen Phasenübergangs der Nanopunkten mit Größen kleiner 200 nm. Obwohl eine Modifikation von T_C in nanostrukturierten Proben nicht überraschend ist, wird normalerweise nur eine Abnahme von T_C beobachtet, die mit der Verringerung der Anzahl der nächsten Nachbarn verbunden ist, wenn sich eine der Dimensionen des Systems mehreren Nanometern nähert. In meinen Proben sehe ich einen allmählichen Anstieg von T_C mit abnehmender Punktgröße, beginnend mit $T_C = 149 \pm 1\,\mathrm{K}$ in Dünnschichten und Punkten $> 200\,\mathrm{nm}$ und Erreichen eines Maximums von $T_C \approx 157\,\mathrm{K}$ bei einer Punktgröße von 35-40 nm. Um ein solches Verhalten aufzuklären, untersuche ich die strukturellen Eigenschaften der Nanopunkte mithilfe einer STEM-basierten geometrischen Phasenanalyse. Diese zeigt eine Verringerung der epitaktischen Kompression bei kleinen Punkten. Die Verminderung des Kompression geht mit der Reduzierung der Punktgröße zu und geschieht auf derselben Längenskala wie der beobachtete Anstieg von T_C. Literaturdaten, die eine Abhängigkeit des Magnetismus in $SrRuO_3$ von der Menge der angewandten Kompression zeigen, bestätigen diese Interpretation.

Durch Analyse des Verhaltens der Hystereseschleifen der Nanopunkte verfolge ich die Entwicklung von $M(B)$ mit abnehmender Strukturgröße. Ich sehe, dass die Hysteresekurven ab einer Punktgröße von $\approx 10\,\mu\mathrm{m}$ und kleiner von der Dünnschichtform abweichen. Ich beobachte eine allmähliche Verringerung des Verhältnisses von Remanenz zu Sättigungsmagnetisierung von $M_{rem}/M_{sat} = 0.85$ in den Dünnschichten auf $M_{rem}/M_{sat} = 0.51$ und $M_{rem}/M_{sat} = 0.44$ in 200 und 50 nm Punkten. In der Messung ist das Magnetfeld orthogonal zur Probenebene orientiert. Das zeigt, dass sich die magnetische Leichtachse in einem anderen Winkel ausrichtet. Aus der Steigung der Hysteresekurven bei kleinen Feldern schätze ich die Werte des Anisotropiefelds und der Anisotropiekonstante und schließe daraus, dass sie nach der Strukturierung in der gleichen Größenordnung bleiben. Um das Verhalten der magnetischen Anisotropie in den Punkten quanti-

tativ zu beschreiben, müssen jedoch andere experimentelle Methoden verwendet werden. Ich stelle auch fest, dass eine Modifikation des hysteretischen Verhaltens im Bereich der Magnetfelder von ≈ 0 bis 2.5 T mit wechselnder Periodizität der Punkte stattfindet, das eine Wechselwirkung zwischen den Punkten impliziert. Durch die SQUID-Messungen allein konnte nicht festgestellt werden, ob diese Effekte von entmagnetisierenden Schachbrettzuständen oder von Wirbel- oder Multidomänenzuständen innerhalb der Punkte stammen.

Neben der Erforschung von Nanopunkten untersuchte ich auch den elektrischen Transport in Nanodrähten aus $SrRuO_3$, wie in Kapitel 6 beschrieben. Für diese Proben wurde (110) $DyScO_3$ als Substratmaterial verwendet, um Leckströme zu vermeiden, die in $SrTiO_3$ auftreten, das mit Ionen beschossen wurde. Ich habe erfolgreich Drähte mit Breiten bis zu 30 nm und einer Dicke von 12 nm hergestellt und gezeigt, dass das Material leitfähig und ferromagnetisch bleibt. $R(T)$-Kurven, die in einem Temperaturbereich bis zu 2 K gemessen wurden, zeigen dieselben charakteristischen Merkmale wie die entsprechenden Dünnschichten. Die Drähte sind robust und halten eine Leistung von bis zu $\approx 300\,\mu$W aus, das einem Strom von $I \approx 300\,\mu$A und einem Spannungsabfall von $U \approx 1$ V entspricht. Die Eigenschaften von $I(V)$ Kurven sind glatt mit einer Nichtlinearität, die durch den Effekt der Widerstandserwärmung verursacht wird. Bei einer Leistung von $P \approx 50\,\mu$W wird bei Nanodrähten aller Größen eine kleine Anomalie beobachtet, die im dI/dV-Signal gut sichtbar ist. Die Anomalie tritt anscheinend auf, wenn die lokale Temperatur des Drahtes die des ferromagnetischen Phasenübergangs übersteigt.

Die Ergebnisse dieser Arbeit zeigen, dass es möglich ist, mithilfe eines Top-Down-Prinzips und konventioneller Elektronenstrahllithographie epitaktische Nanostrukturen aus komplexen Materialien mit Strukturgrößen von nur etwa 10-20 nm unter Beibehaltung ihrer funktionellen Eigenschaften herzustellen. Gleichzeitig bleibt die Materialstruktur frei von größeren Defekten und toten Schichten, die die Nanostruktur-Eigenschaften verschlechtern. Am Beispiel eines Materials zeige ich neue interessante Merkmale in einzelnen oder schwach wechselwirkenden Nanostrukturen, die durch räumliche Begrenzung und die daraus folgenden elektronischen und strukturellen Modifikationen verursacht werden. Darüber hinaus ergeben sich bei stark wechselwirkenden Ensembles zahlreiche weitere Möglichkeiten bis hin zu künstlichen Festkörpern, die sich aus solchen nanostrukturierten Objekten zusammensetzen. Wir erwarten viele Möglichkeiten für die Herstellung und Erforschung solcher Systeme, die aus verschiedenen Materialkombinationen aus der breiten Familie von Substanzen mit korrelierten Elektronensystemen bestehen.

Chapter 1

Introduction

1.1 Quantum confinement, correlated electrons and magnetism

We live in a three-dimensional world. At least that is what we know from our daily experience. Laws of nature are closely bound to dimensionality. It defines the strength and character of interactions between objects, laws of electromagnetic radiation, etc. [1, 2]. Some researchers even argue that the three-dimensional world is the only possible one in which complex systems can exist [3].

In solid state physics, the problem of dimensionality is no less important than in cosmology or general relativity. Properties of solids are defined by the movements and interactions of electrons that make them up. Of course, the intrinsic dimensionality of space does not change for these particles. But it is possible to confine electrons in one or more dimensions by varying the material structure or applying external conditions through electromagnetic fields or patterning. This allows to reduce the number of degrees of freedom effectively available for electrons and to significantly modify the properties of the electron systems.

Already in the 1960s, the role and importance of size effects in so-called mesoscopic systems (i.e., objects that have sizes intermediate between single atoms or molecules and bulk) was first analyzed by studying absorption spectra of excitons [4, 5]. The first confinement experiments were done in the field of III-V semiconductor materials which was rapidly developing at the time. Researchers found that size effects may significantly affect the density of states, the size of the band gap, the behavior of excitons, phonon distributions and many other characteristics of semiconductors [6].

Materials may be confined in multiple dimensions – 2D confinement is realized in thin films [7, 8], at interfaces [9–11] or in layered materials [12, 13]; 1D

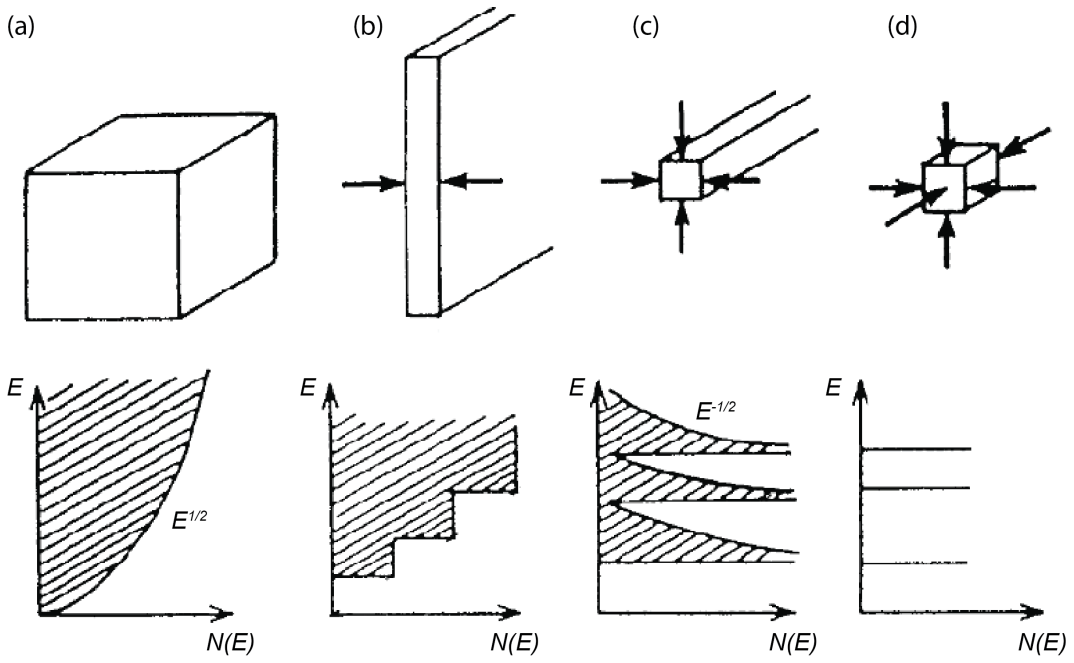

Figure 1.1: Schematic illustration of the effects of spatial confinement on the spectral density of states of a free electron system. (a) unmodified bulk state, (b) confinement in 2D, (c) 1D, (d) 0D. The gradual transformation from the $\sqrt{E}$ dependence of the density of states in the bulk form to a set of separate atomic-like energy levels in 0D case is shown. Modified from [6].

confinement is possible in nanolines [14]; and 0D confinement results in quantum dots, also dubbed as artificial atoms [15]. Furthermore, upon confinement in one or several dimensions, materials demonstrate properties that increasingly deviate from their bulk form [6]. Figure 1.1 shows schematically what happens to the density of states of a semiconductor upon various types of confinement. Of course, the exact form and features of such a transformation depend uniquely on the material, but in general it can be thought of as a gradual transition from the continuous density of states to a set of discrete energy levels observed in 0D objects. Such an energy structure resembles the one which exists in isolated atoms which is the reason to call such objects "artificial atoms" [16].

Low-dimensional semiconductor systems have been extensively studied for several decades and have already found widespread applications in various research fields and even commercial devices [17–20]. Conventional semiconductors represent "mean-field" systems in which interactions between electrons are negligible compared to their kinetic energy. In such materials, the interaction of a single electron with the other electrons can be described as a movement in an averaged,

mean potential. Modern solid state physics is exploring a broad class of compounds in which such an approach no longer holds. These are correlated materials in which individual electron-electron interactions can no longer be neglected [21]. Even in their bulk form, the complexity of the electron behavior in such systems produces competing ground states with different symmetries that gives rise to a much larger variety of possible functional behavior and novel, interesting physics. This may include, but is not limited to, various magnetic phases, ferroelectricity, high-temperature superconductivity, and Mott insulator behavior. Often, a large number of such phases may exist in a single material, generating complex phase diagrams [22].

As has been mentioned above, effects of spatial confinement may modify the properties and behavior of electron systems significantly and introduce complexity and electron correlations even in relatively simple compounds. In complex, intrinsically correlated compounds, however, the effects of such a confinement have been explored to a much smaller extent.

Recently, more and more research groups focus on studying 2D confined correlated systems. This includes interfaces between different materials giving rise to 2D electron liquids and gases [23], ultrathin films generating quantum well effects [8], superlattices with cross-talking layers [24], etc. In most cases, however, the investigations do not go beyond 2D confinement. There are only scarce reports on what happens with correlated systems confined in more dimensions - quantum wires or quantum dots. The reason for this is the high complexity of such materials. Only recently, growth techniques such as pulsed laser deposition or molecular beam epitaxy have developed to an extent that allows the growth of high-quality layers of these substances. Patterning them to smaller dimensions remains a challenge.

In this work, we make the next step below the 2D confinement and explore correlated systems confined in more dimensions. Of special interest for us is the case of quantum dots. Questions that motivate this research are: how do properties of intrinsically correlated systems change upon confinement to low-dimensional structures? What new interesting effects can be generated in these complex correlated compounds as compared to confined mean-field systems?

Several successful attempts have been made by other research groups to fabricate such devices. For example, in the group of J. Levy at the University of Pittsburgh, USA, an AFM-based technique was developed to modify properties of the $LaAlO_3/SrTiO_3$ interface using the interaction between the sample surface and the tip of an atomic force microscope [25, 26]. They found that local voltage pulses applied to a three-unit-cell-thick layer of $LaAlO_3$ grown on $SrTiO_3$ can switch the interface from its normally insulating to a conducting state creating areas of conductivity. This can be done with an outstanding spatial resolution

of just a few nanometers. Such structures, however, are unstable and deteriorate rapidly in air and under the light irradiation. A different set of ways to create such nanoobjects is based on bottom-up self-assembling techniques utilizing such methods as chemical solution deposition [27] or diffusion controlled growth on mixed termination substrates [28]. These powerful approaches permit the creation of structures with sizes down to dozens of nanometers. However, they do not provide control over the form or arrangement of the objects, which is essential for creating complex systems of nanoobjects.

Here, we want to fabricate confined systems of correlated materials in a controllable manner with the aim to create ensembles of interacting devices and even build artificial solids of such objects. In this work, we develop the top-down approach based on electron beam lithography to fabricate nanodevices. It allows us to create nanostructures of arbitrary two-dimensional form and mutual arrangement. Such an approach has been applied before to pattern various correlated systems [29–31]. The structure sizes, however, were much larger than what is expected to enter the quantum confinement regime. We succeed in fabricating nanodots with diameters as small as 15 nm which is several times smaller than previously reported. As a model system for the study, we choose $SrRuO_3$ epitaxially grown on (100) $SrTiO_3$ and (110) $DyScO_3$. For several reasons this is the material of choice. First, one of the most important requirements for successful quantum confinement is the material purity. Impurities or defects in the substance act as inelastic scattering centers that result in the loss of quantum coherence. It is therefore of major importance to use materials that can be grown with high purity and low defect concentrations. $SrRuO_3$ is such a compound. Due to its many remarkable properties, such as unconventional electrical transport and ferromagnetism, it is one of the most studied and used perovskite compounds, the growth of which is relatively well understood [32]. Second, the ferromagnetism inherent in $SrRuO_3$ is straightforward to measure and that provides further insights into the material structure. Ferromagnetism is also a function of electron correlations and it is interesting to study how magnetic properties can be modified in such confined magnetic systems. As described below, the ferromagnetic properties of $SrRuO_3$ are sensitive to the material purity, stoichiometry and applied strain. This allows, by measuring the magnetism, to observe how the material structure changes during the nanodevice fabrication process and to draw conclusions about the formation of defects and dead layers.

1.2 Structure of this work

This thesis is devoted to the fabrication and study of nanodevices fabricated of the intrinsically correlated and ferromagnetic $SrRuO_3$. Both, nanodots and

nanolines are investigated. For nanodots the focus is directed to the study of the magnetic properties, for nanolines it is aimed on the properties of the electrical transport.

The current chapter gives the basic introduction and motivation for the research project and describes the properties of the materials used in the devices.

Chapter 2 is devoted to the theoretical background of the work. This research lies at the intersection of several areas of physics - confined quantum systems, nanoscience, correlated materials and magnetism. A brief introduction aims to provide the necessary background knowledge and literature review for the understanding of the content of the following chapters. It also intends to identify points of contact between the research fields.

Chapter 3 describes the procedure of sample fabrication covering all its steps - from the substrate cleaning to the patterning of the nanodevices. It also describes the experimental techniques involved in the fabrication process such as pulsed laser deposition, electron beam lithography, ion milling, etc.

In Chapter 4, various physical properties of the samples are examined at different stages of the sample preparation process. This includes the analysis of structural (AFM, XRD) and electrical properties of the $SrRuO_3$ thin films grown on (100) $SrTiO_3$ and (110) $DyScO_3$ as well as the properties of the nanodots and nanolines. Magnetic properties of the samples are discussed separately in the following chapter.

Chapter 5 presents the main results of the thesis. It is entirely devoted to the studies of the magnetic properties of the nanostructured $SrRuO_3$. We compare the material properties before (in the thin film form) and after the patterning into nanodots. This reveals how the material is modified upon patterning and what new effects appear in the confined material as compared to the bulk form. Interesting behavior and phenomena in the nanodots such as an enhancement of the Curie temperature, the modification of hysteretic properties, and others are described here.

Chapter 6 concentrates on $SrRuO_3$ nanolines. We fabricate nanolines of $SrRuO_3$ with widths down to 30 nm and perform electrical transport measurements on the structure. We show that down to such sizes the material preserves its functional properties remaining conductive and ferromagnetic.

Chapter 7 is the last chapter that interprets the main experimental output of the work. Results are put together and discussed in the context of the future development and perspectives of this new emerging field of low-dimensional structures of intrinsically correlated materials.

1.3 Materials

1.3.1 $SrRuO_3$

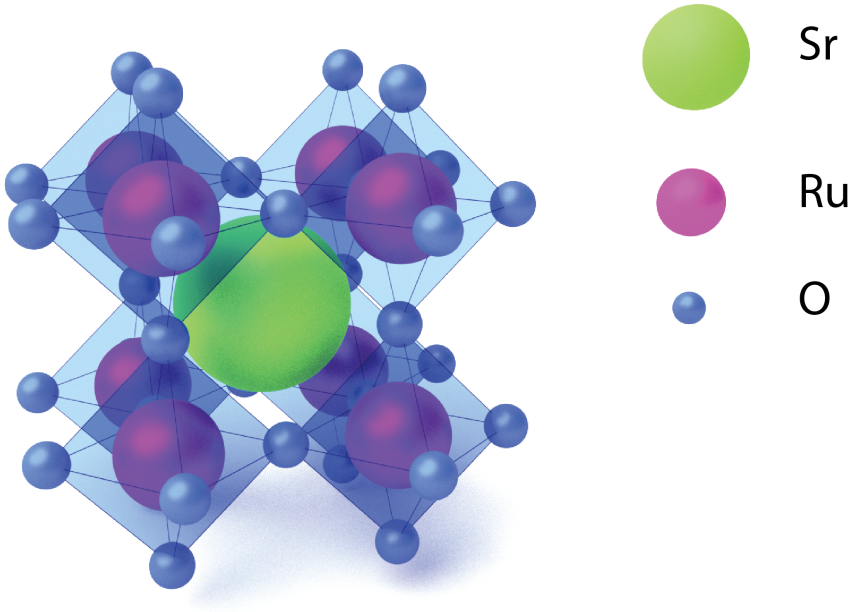

Figure 1.2: Schematic illustration of the perovskite atomic structure using the example of $SrRuO_3$. *A*-site Sr ion is located in the center and surrounded by *B*-site ions of Ru. Ru and O form RuO_6 octahedra. This structure is typical for all compounds used in this work ($SrTiO_3$, $SrRuO_3$, $DyScO_3$). Unit cell distortions caused by the tilt of the RuO_6 octahedra are neglected.

$SrRuO_3$ is in many respects a remarkable material. It belongs to a family of quasi-cubic ABO_3 perovskite oxides. In the bulk form, above 677 °C it exhibits the cubic symmetry but experiences a sequence of phase transitions with decreasing symmetry upon cooling - to a tetragonal phase at 677 °C and finally to an orthorhombic structure at 547 °C in which it remains down to low temperatures [33]. According to some studies, the transition temperatures in thin films are different. For example, for films grown on (100) $SrTiO_3$ the orthorhombic-tetragonal and the tetragonal-cubic transitions occur at 350 °C and 600 °C, respectively [34]. At low temperature, the rotations of RuO_6 octahedra produce an enlarged unit cell which has the lattice parameters $a = 5.5670$ Å, $b = 5.5304$ Å and $c = 7.8446$ Å [35], corresponding to a pseudo-cubic lattice parameter of $a = 3.93$ Å. The excellent chemical stability of $SrRuO_3$ together with crystal parameters well-suitable for epitaxial growth on $SrTiO_3$, and its electrical conductivity make it a preferable bottom electrode or a stable functional layer in

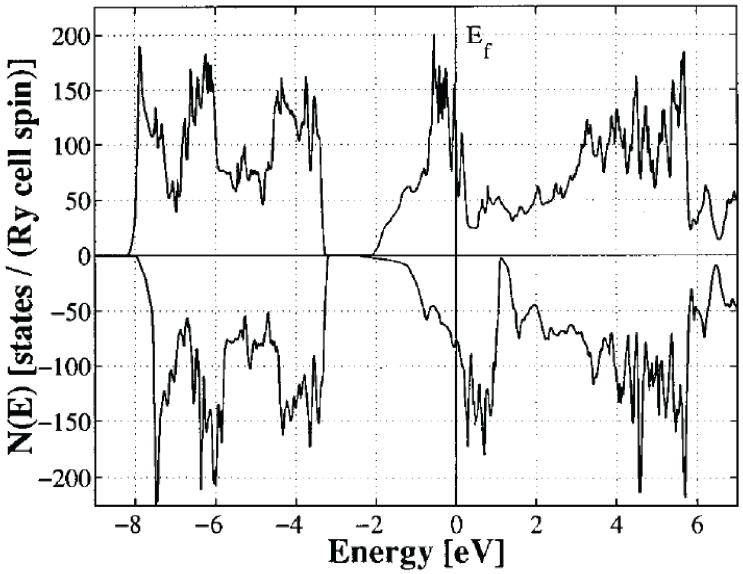

Figure 1.3: Electronic structure of $SrRuO_3$ calculated by spin-density functional theory. Majority and minority spin bands are plotted upward and downward, respectively. From [37].

numerous different oxide heterostructures [36].

$SrRuO_3$ exhibits metallic behavior due to a partially filled band associated with Ru $4d(t_{2g})$ orbitals hybridized with O $2p$ levels [37]. Its electronic transport properties are unusual and controversial. According to various studies, indications of bad metal behavior [37], Fermi-liquid behavior in samples with low residual resistivity [38] and non-Fermi-liquid behavior in samples with higher degree of disorder [39, 40] are observed. $SrRuO_3$ has a rather high carrier concentration of the order of $10^{22}\,\mathrm{cm}^{-3}$ [41] and a relatively high conductivity of about $300\,\mu\Omega{\cdot}\mathrm{cm}$ in the bulk at room temperature [37]. The conductivity of thin films depends on the substrate material and the growth technique and normally lies in the range of $100 - 400\,\mu\Omega{\cdot}\mathrm{cm}$ [42]. Infrared conductivity measurements reveal a temperature-dependent effective mass in the range of $m^* = (1\text{-}6)\,m_e$ [43].

The density of states of $SrRuO_3$ was first calculated by Allen et al. [37] and Singh [44] using first principle calculations (see Fig. 1.3). The large Stoner band splitting of $\approx 1\,\mathrm{eV}$ makes $SrRuO_3$ a strong itinerant ferromagnet (the degree of itineracy is $q \approx 1.3$). Due to the large crystal field, $SrRuO_3$ is expected to stabilize in the low-spin configuration with a magnetic moment of $2\,\mu_\mathrm{B}$ per Ru atom. Experimentally observed magnetic moments are, however, lower - $1.1 - 1.68\,\mu_\mathrm{B}$ (depending on the crystal structure) which is attributed to electron delocalization [44, 45]. Nevertheless, this magnetic moment is one of the largest

among all $4d$ compounds. Up to date, there is only scarce evidence of a high-spin configuration in $SrRuO_3$ [46].

The Curie temperature of the material is relatively high - $T_C = 160 \pm 10\,\mathrm{K}$ in the bulk [47]. For thin films, the value of T_C is smaller and depends on numerous factors such as the substrate material, the film thickness and the growth technique. On (100) $SrTiO_3$, one of the highest values of $T_C = 150\,\mathrm{K}$ are achieved by MBE growth (the film thickness of 85 nm) which is $\approx 10\,\mathrm{K}$ smaller than in the bulk [48]. Good ferromagnetic properties are combined with a strong uniaxial magnetocrystalline anisotropy. For thin films grown on $SrTiO_3$, the easy axis lies in the (100) plane and is oriented at an angle of $\sim 45\,^\circ$ to the film normal [49], rotating to $\sim 30\,^\circ$ at low temperatures at a rate of $\sim 0.1\,\mathrm{deg/K}$ [42]. The reported values of the anisotropy field are, however, controversial and span a range from 2 to 12 T [32]. As was first reported in [50], the magnetic properties of $SrRuO_3$ films also depend on the film thickness - the authors find that ferromagnetism (including both T_C and the magnetic moment) starts to decay with reducing film thickness below 10 unit cells to completely disappear below 4 unit cells [51]. On the other hand, measurements of single-unit-cell-thick layers of $SrRuO_3$ embedded in $SrTiO_3$ and $SrRuO_3/SrTiO_3$ superlattices [52] reveal that the material remains ferromagnetic and conducting down to this extreme thickness limit. The reason for such a large spread in reported properties is presumably the purity of the grown films, significantly affecting their properties. Magnetic domains in $SrRuO_3$ form stripes with widths from $\sim 200\,\mathrm{nm}$ to several μm with a domain wall width of $\sim 3\,\mathrm{nm}$ [53]. Usually, the domains are oriented along the b axis of the lattice.

Another major parameter influencing the properties of $SrRuO_3$ is its stoichiometry. It is especially relevant for PLD grown films as there is no direct way to vary the stoichiometry of the target. The most common off-stoichiometry for $SrRuO_3$, especially PLD grown, are Ru vacancies which are caused by the high Ru vapor pressure. Even a small Ru deficiency in the films affects their properties and results in an increase of the unit cell volume and a reduction of T_C [54]. For this reason, the optimization of growth parameters is the essential step in obtaining high quality structures. Some research groups use Ru-rich $SrRuO_3$ PLD targets to compensate the loss of Ru during growth [55]. In our work, however, a careful optimization of growth parameters sufficed to achieve high quality films.

Strain is also one of the mechanisms known to influence magnetic properties of $SrRuO_3$. Using *ab-initio* DFT calculations, it was shown that uniaxial and epitaxial strain in $SrRuO_3$ significantly alter its magnetism [56] . Studies of $SrRuO_3$ grown on different substrates demonstrate that the magnetic properties differ depending on the amount of strain in thin films [57]. Furthermore, $SrRuO_3$ films released from their substrates show a 10 K higher T_C of 160 K [58]. Another study showed that a $SrTiO_3$ capping layer grown on $SrRuO_3$ epitaxial films de-

posited on $DyScO_3$ modifies the oxygen octahedral structure in the $SrRuO_3$ with a corresponding increase of T_C [59].

$SrRuO_3$ is a material with moderate electron correlations. The correlations originate from the extended nature of the $4d$ orbitals in this material and manifest themselves in various effects. For example, a comparison of DFT band structure calculations with the band structures obtained from photoemission spectroscopy and bremstrahlung-isochromat spectroscopy reveals that the peaks in the density of states associated with t_{2g} levels are significantly broadened as the result of electron-electron correlations [60]. Other measurements show that the low-temperature resistivity minima often observed in $SrRuO_3$ originate from weak localization and electron interaction [61]. Others confirm this result and show that this effect is not related to the magnetic properties as it is also present in structurally disordered thin film samples without magnetic order [62]. P. B. Allen *et al.* also find evidence of electron correlations in specific heat measurements of $SrRuO_3$ bulk single crystals where they discover a strong enhancement of the Sommerfeld constant $\gamma_{expt}/\gamma_{theor} = 3.7$ compared to theoretical predictions [37]. They argue that such an enhancement is caused by Coulomb correlation effects or by spin fluctuations.

1.3.2 $SrTiO_3$

In many respects, substrates are no less important than the material of interest. It is the substrate that defines the strain induced in the structure and the interaction with the substrate can significantly influence the functional properties of the film. $SrTiO_3$ can be considered the working horse of all perovskite substrates. Historically, it became important as a substrate for the growth of the high-temperature superconductor YBCO [63] and since then has remained popular in the family of perovskite substrate materials. Its cubic structure, chemical stability, well-understood properties and the lattice constant, suitable for many materials, make it the substrate of choice for a large fraction of heterostructures [64]. $SrRuO_3$ is no exception.

$SrTiO_3$ has a cubic unit cell with a lattice parameter of 3.905 Å that provides a compressive strain of $s = (d_{SRO} - d_{STO})/d_{SRO} = 0.64\%$ for an epitaxial $SrRuO_3$ film grown on it. Well-developed methods of surface treatment (either chemical or thermal) allow to prepare $SrTiO_3$ with a singly terminated surface (rich in Sr oxide or in Ti oxide) that also has a large impact on the properties of the deposited film. At 105 K, $SrTiO_3$ reveals a phase transition from cubic to tetragonal with a symmetry reduction from Pm3m to I4/mcm [65, 66].

A wide band gap of 3.2 eV [67] grants $SrTiO_3$ good insulating properties which, however, change to semiconducting if the material is doped with oxygen vacan-

cies [68, 69]. Oxygen vacancies also endow $SrTiO_3$ with magnetic properties. Depending on the concentration of oxygen vacancies, the material may exhibit paramagnetic or ferromagnetic behavior [70, 71]. Oxygen vacancies may form through various processes, such as high-temperature reduction in an oxygen poor environment [72], exposure to ion fluxes [73] or chemical treatment [74]. In case the insulating properties are crucial for the structure, these processes have to be avoided. The fabrication process used to produce nanostructures for our study includes Ar milling which also creates oxygen vacancies in $SrTiO_3$. Since both conductivity and magnetism play an important role in this work, it is important to take these properties of the material into account. Paramagnetic contributions from the substrate can be dealt with as they become significant only at low temperatures. The appearance of conductivity, however, is more crucial and spoils electrical transport measurements. For that reason, for some devices, $SrTiO_3$ has to be replaced with another substrate which remains insulating even after Ar milling.

1.3.3 $DyScO_3$

$DyScO_3$ belongs to a new class of rear-earth perovskite scandate ($ReScO_3$) substrate materials [75–77]. The necessity to use $DyScO_3$ as an alternative substrate for $SrRuO_3$ growth for nanoline devices is explained in detail in Sec. 6.1. In general, scandate substrates are good candidates for $SrRuO_3$ growth due to a very favorable range of pseudo-cubic lattice parameters from 3.93 Å to 4.05 Å, the range which is not covered by any other commercially available substrates [78]. Such a gradual variation of the pseudo-cubic lattice parameter is possible because of the Sc-O-Sc angle changing from 139° to 144° depending on the rare-earth element [78]. Similar to other scandates, $DyScO_3$ has an orthorhombically distorted perovskite unit cell with lattice parameters $a = 5.444$ Å, $b = 5.721$ Å, $c = 7.906$ Å and belongs to the 62-P_{nma} space group [79]. The (110) surface of such substrate represents a square mesh with a lattice spacing of $a = 3.944$ Å.

At $T = 1273$ K, $DyScO_3$ undergoes a structural phase transition from orthorhombic to cubic [78]. This value is, however, beyond the temperature range of most applications. The material is well insulating with a band gap of $\approx$ 5.9 eV [80] and a large dielectric constant [81]. The thermal expansion is slightly anisotropic due to the rotation of the ScO_6 octahedra. On average, however, the coefficient of thermal expansion is close to that of other perovskites, which is convenient for its application as a substrate material for epitaxial perovskite films [78].

$DyScO_3$, as well as other rear-earth scandates, is strongly paramagnetic with a saturation magnetization of up to $M_s \approx 8\,\mu_B$/Dy at low temperature [82]. The crystallographic easy axis is oriented along the [100] and the hard axis along the

[001] directions. At a temperature of $T_N \approx 3.1\,\mathrm{K}$ the material experiences a phase transition to the anti-ferromagnetic state. This relatively low temperature, however, does not affect most applications.

Strong magnetism of $DyScO_3$ is important for its applications as a substrate for magnetic films as the magnetization coming from the substrate itself can completely mask the one of a thin film. For this reason, $DyScO_3$ is not suitable for the investigation of magnetic properties in $SrRuO_3$ structures. However, because it stays insulating after the ion irradiation, it can be used for several applications, such as the study of the electrical transport in $SrRuO_3$ nanolines.

Chapter 2

Background knowledge

2.1 Magnetism at the nanoscale

Magnetic properties can be substantially altered when the substances are structurally restricted in space on the micrometer and nanometer scales. Size changes may cause modifications of the crystal and domain structures, the magnetic anisotropy, the density of states, and of other properties. In this section, we give a brief overview of these modifications which are essential for understanding the behavior of magnetic nanodots and nanolines.

Historically, the science of magnetic nanostructured materials has been developed mainly for 3d (Fe, Co, Ni) and 5d (Gd) ferromagnetic metals, their alloys and compounds [83]. With the rapid advance of the semiconductor technology, a wide range of magnetic semiconductors have been discovered. These materials can be divided into two main families. The first family comprises dilute magnetic semiconductors (DMSs) based on traditional semiconductors doped with transition metals, for example GaAs or InSb doped with Mn [84,85]. The second family consists of doped oxides such as ZnO, MgO, TiO_2 [85].

Despite the very different structure and chemistry, these classes of magnetic materials share some common behavior upon the size restriction. Nanostructured systems can be classified into two-dimensional (2D), one-dimensional (1D) and zero-dimensional (0D) structures. In the following, we describe for these three cases which modifications of the magnetic properties can be observed.

2D confinement. Two-dimensional magnetic structures include thin films, monolayers, interfaces and superlattices. Modification of the magnetic properties in these structures can involve several mechanisms. For example, materials that are not ferromagnetic in bulk but close to the Stoner criterion [86] may become ferromagnetic when grown as thin films. Examples are V, Cr, Mn, Ru, Pt [83]. This may happen via an interaction with the substrate or due to a reduced band-

width and the resulting increase of the density of states. Also, structural phases with magnetic order may become energetically more favorable when growing thin films on suitable substrates [87]. For example, the crystal structure of Co which is hcp in the bulk changes to fcc and bcc when Co is grown on Cu and GaAs, respectively [88]. These metastable phases possess different band structure and exchange splitting and, therefore, reveal different magnetic properties. Another possible spot for stabilization of metastable phases are misfit dislocations and patches appearing when growing on substrates with a large lattice mismatch.

Near the Curie temperature T_C, the magnetization of a conventional ferromagnet can be described by [89]:

$$M \sim \left(1 - \frac{T}{T_C}\right)^{\beta}, T \to T_C \tag{2.1}$$

where β is the critical exponent which depends on the dimensionality of the system and the number of degrees of freedom for spins. According to the Ising model for nearest neighbor interacting spins, the value of the critical exponent should equal $\beta = 0.325$ and $\beta = 0.125$ for three- and two-dimensional lattices of spins, respectively [90,91]. Therefore, the temperature dependence of the magnetization is expected significantly differ for these two cases. With decreasing film thickness, the transition between the regimes is rather abrupt and happens about 6 unit cells layer thickness for 3d ferromagnetic materials [91]. Another well-known and universal phenomenon is the reduction of T_C with reducing film thickness. The effect is related to reducing the number of nearest neighbors and the corresponding destabilization of the magnetic order [92]. In first approximation, this effect does not depend on the material and can be described by another critical exponent α and normalized to bulk T_C [83]:

$$\frac{T_C(n)}{T_C(\infty)} = 1 - \left(\frac{n_0}{n}\right)^{\alpha}, n \to \infty \tag{2.2}$$

with $\alpha = 1.56$ as predicted by the Ising model. According to this formula, T_C reduces by half at ~ 5 unit cells and the complete disappearance of the ferromagnetic properties at the thickness of one unit cell is expected. This effect is observed not only in thin films but also in nanolines [93] and quantum dots [92]. The behavior of the magnetic anisotropy also changes upon thickness reduction. Normally, for thin films the magnetic easy axis lies in the film plane, governed by the shape anisotropy (this rule, however, is not universal, $SrRuO_3$ being one of the exceptions). At the thickness of ~ 5 unit cells, the interface or surface anisotropy comes into play that reorients the easy axis in the out-of-plane direction [94–97]. The fact that magnetic properties change in many respects close to a thickness of five unit cells implies that the exchange interaction with the second nearest neighbors makes a significant contribution to the magnetic behavior [83].

1D confinement. One-dimesional magnetic structures, i.e., nanolines and atomic steps, can be described in a similar manner as two-dimensional structures. The difference is that equations, for example for the exchange energies, have to be formulated in a cylindrical geometry rather than a planar one. All effects taking place in two dimensions can be also extended to the one-dimensional case. Additional effects like the appearance of curvature-induced anisotropy [98] or longitudinal domain walls may take place [99]. As a result of the cylindrical geometry, special azimuthal magnetic domain structures may appear [100]. The mechanism for this structure formation is similar to the one described below for nanodots. In the context of spintronics applications, great attention was attracted to the phenomenon of domain wall motion occurring in nanolines under the influence of an external magnetic field or a spin-polarized current through the line. The common approach to describe the domain wall motion is the solution of the Landau-Lifshitz-Gilbert equation for adiabatic and non-adiabatic spin-torques [101]:

$$\dot{\mathbf{m}} = -\gamma_0(\mathbf{m} \times \mathbf{H}) + \alpha(\mathbf{m} \times \dot{\mathbf{m}}) - (\mathbf{u} \cdot \bigtriangledown)\mathbf{m} + \beta\mathbf{m} \times [(\mathbf{u} \cdot \bigtriangledown)\mathbf{m}], \tag{2.3}$$

where γ is the gyromagnetic ratio, α is the damping parameter, β is the non-adiabatic coefficient and $\mathbf{u}$ is the spin-polarized current velocity.

0D confinement. In nanoparticles fabricated of magnetic materials, one can observe drastic changes of magnetic properties that happen several times when the particle size approaches different fundamental lengths. The most important of these lengths are the crystalline anisotropy length (l_K), the applied-field length (l_H), and the magnetostatic length (l_S), defined as [102]:

$$l_K = \sqrt{J/K}; \quad l_H = \sqrt{2J/HM_S}; \quad l_S = \sqrt{J/2\pi M_S^2} \tag{2.4}$$

where J defines the exchange interaction, K is the magnetic anisotropy constant, H is the value of an applied magnetic field and M_S is the saturation magnetization. For most magnetic substances these lengths are in a range of 1-100 nm.

l_K is a measure of a length scale at which the magnetic anisotropy becomes relevant. The value of l_K may also define the domain wall width. For nanoparticles, the description of the magnetic anisotropy is rather complex as in addition to the crystalline anisotropy, which is common for bulk, other contributions become relevant. The magnetocrystalline anisotropy originates from the spin-orbit coupling and is intrinsic to the material itself and to its crystal structure. When the magnetocrystalline anistropy is present in a substance, it is energetically favorable for the magnetization to be oriented along one (in the case of uniaxial anisotropy) of the crystallographic directions (for $SrRuO_3$ it is the (001) planes). The uniaxial anisotropy energy can be described as $E = K \sin^2\theta$, where θ is the angle between the magnetization and the easy axis. For epitaxially-grown nanoparticles, other

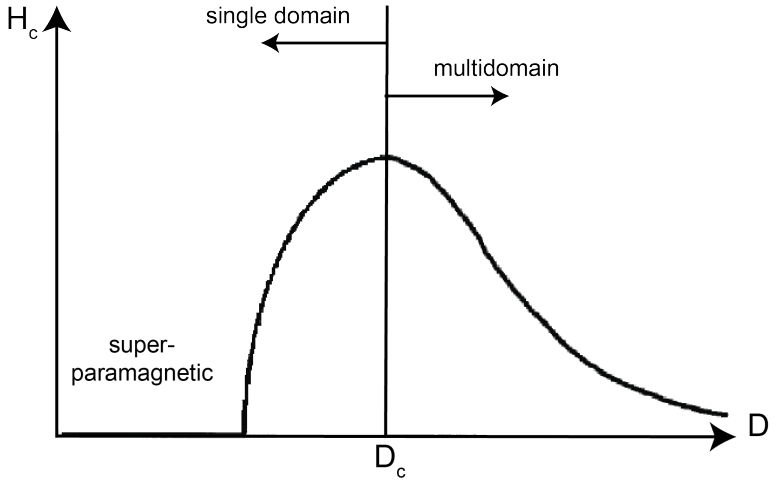

Figure 2.1: Schematic illustration of the behavior of the coercivity as a function of the particle size. A transition between multidomain, single domain and superparamagnetic states upon size reduction is observed. Modified from [102].

common contributions to the anisotropy energy are the shape anisotropy and the stress anisotropy. The shape anisotropy becomes relevant when the shape of a material is not spherical. It is caused by the demagnetizing fields which appear in the material. For example, in a long needle made of ferromagnetic material, it is more favorable for the magnetization to be oriented along the long axis of the needle as this orientation significantly reduces the demagnetizing field. For nanoparticles, the shape anisotropy can be rather strong and it is the only type of anisotropy, the value of which can be comparable to the crystalline anisotopy [103]. The stress anisotropy is relevant when a magnetic crystal is subjected to a strain which is often the case for epitaxially grown layers. It may also appear as the result of the application of an external pressure, a rapid cooling, etc [103].

Bulk ferromagnets are usually divided into a set of magnetic domains separated by domain walls. This configuration reduces the amount of the external stray field, and thus saves energy. The structure of the magnetic domains is intrinsic to a material and can be diverse. In large particles, the coercivity to large extent is governed by the nucleation and motion of the magnetic domains rather than by other factors. With reducing the particle size, it becomes more favorable to reduce the number of the domains and, at some critical length D_c, switch to a single domain regime (see Fig. 2.1) [102]. In multi-domain particles, the coercive field increases with decresing size. At sizes smaller than D_c, however, it falls down. For different materials, the value of D_c varies in the range of $\sim 10 - 200\,\mathrm{nm}$ [104]. If the shape anisotropy is present, particles can remain single domain at larger sizes. With reducing the size further down, the nanoparticle spins become more easily affected by thermal fluctuations and may begin to flip randomly. The characteristic time of such flips is called the Neel relaxation

time [105]:

$$\tau_N = \tau_0 \exp \frac{KV}{k_B T}, \tag{2.5}$$

which depends on the particle volume V, its magnetic anisotropy K, temperature T and the τ_0 time constant characteristic for the material. Then, if the measurement time is much larger than τ_N, the particle appears paramagnetic with no coercivity and no net magnetization without the external magnetic field. As τ_N depends exponentially on a particle volume, superparamagnetism is normally observed only in very small particles at sizes of just several nanometers.

Several magnetic particles, if located close to each other, may interact by means of the dipole-dipole interaction [106–108]. For a simplified case, the magnetic field created by a particle with a size l at a distance r can be written as:

$$H_d = \frac{2mr}{[r^2 - (l/2)^2]^2}; \quad H_d = \frac{m}{[r^2 - (l/2)^2]^{3/2}}, \tag{2.6}$$

along the line of the dipole and perpendicular to it, respectively [103]. As can be seen, the dipole interaction decreases as the function of $1/r^3$ and becomes negligible at distances larger than several μm. However, if particles are formed in dense arrays with distances between particles comparable to their size, the interaction between them can influence the magnetic behavior of the system significantly.

Another interesting effect which can be observed in magnetic nanoparticles is the formation of complex magnetic structures, e.g., vortex or closure domain states. The mechanism of the vortex state formation is schematically illustrated in Fig. 2.2(a) [109]. Such structures may be energetically favorable for small nanoobjects as they allow to decrease the amount of the external stray field and thus reduce the energy of the system. Usually they exist only at relatively small magnetic fields as the external influence quickly drives the system to the saturated state. The formation and the exact character of such structures depends on many factors, such as the nanoobject shape, size and aspect ratio, and external fields [103].

Demagnetized states appearing in arrays of interacting nanoobjects have the same underlying mechanism as the vortex states, i.e., the minimization of the system stray field to save energy. Only in this case, the elements of the structure are whole nanoobjects (see Fig. 2.2(b)). The minimization of energy here can be achieved by the formation of anti-ferromagnetic checkerboard states with a part of the magnetic moments oriented upside and an another part downside. These states depend strongly on the magnetic anisotropy of the system and appear mainly when the magnetic easy axis is oriented in the out-of-plane direction [103].

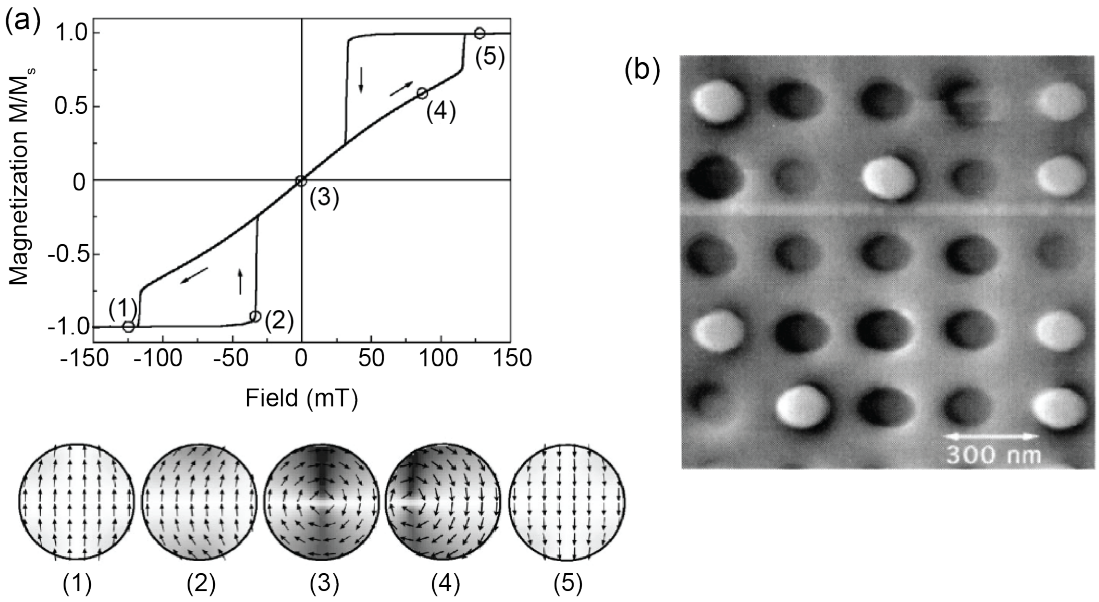

Figure 2.2: (a) Schematic illustration of the process of magnetic vortex formation. At a high magnetic field (1,5), the magnetic system is saturated and all magnetic moments are aligned ferromagnetically. At zero field (3), the energetically favorable magnetic vortex state is observed. At moderate fields (2,4), intermediate regimes take place. (b) Magnetic force microscopy image of an array of interacting magnetic dots of Co at room temperature forming a demagnetized checkerboard state. Adapted from [109, 110].

2.2 Electron correlations

The origin of many interesting physical effects and of a broad spectrum of functional properties of substances lies in the interaction between electrons. Even the behavior of relatively simple mean field materials with a weak intrinsic electron interaction can be substantially enriched by the enhancement of electron correlations which is one of the motivations behind studying various nanodimensional systems.

For many simple metallic compounds, the behavior of electrons can be described in terms of the free electron model according to which electrons in solids move independently and do not interact with each other [111]. Though the model is extremely successful in describing a large number of effects, it fails in many systems when the individual interactions between electrons can no longer be neglected. This may be the case in low-dimensional systems or in complex materials with extended and strongly overlapping orbitals.

The first attempt to take into account the interaction between electrons was done by Wigner in 1934 who proposed the term "correlation energy" [112]. He described it as a lowering of the electronic energy value by introducing Coulomb correlations into a Hartree-Fock wavefunction. Later, Hubbard suggested his simple yet powerful and elegant model which expanded the concept to more complex systems of transition and rear-earth metals with partially filled d- and f-bands [113]. In the framework of the Hubbard model, the behavior of electrons in a periodic potential is described as a hopping between atomic lattice cites governed by two parameters - the kinetic energy of particles t, also called the hopping integral, and the interaction strength U – the Coulomb repulsion between particles at the same atomic site. The correlation strength can be characterized by the ratio U/t. In the limit where $U/t \ll 1$, the system is reduced to a common tight binding behavior. The opposite case of $U/t \gg 1$ represents a set of isolated magnetic moments, a Mott insulator. The region of values between these extremes comprises interesting phases, including ferromagnetic and antiferromagnetic behavior.

More generally, the Coulomb repulsion and the hopping term can be substituted by the electron interaction energy E_{int} and the kinetic energy E_{kin}, respectively [114]. Coulomb repulsion U, exchange energies, bosonic or multiple particle-hole excitations make a major contributions to E_{int}, whereas the electrons' bandwidth characterizes E_{kin}. The case of $E_{kin}/E_{int} \gtrsim 1$ corresponds to mean-field materials, the opposite case to correlated electron systems. Even in compounds with intrinsically small interaction between electrons, electron correlations can be induced by reducing E_{kin}. The effective band width can be reduced by spatial confinement, depletion of the electron system by a gate field or creation of Landau levels by application of magnetic fields to 2D electron systems.

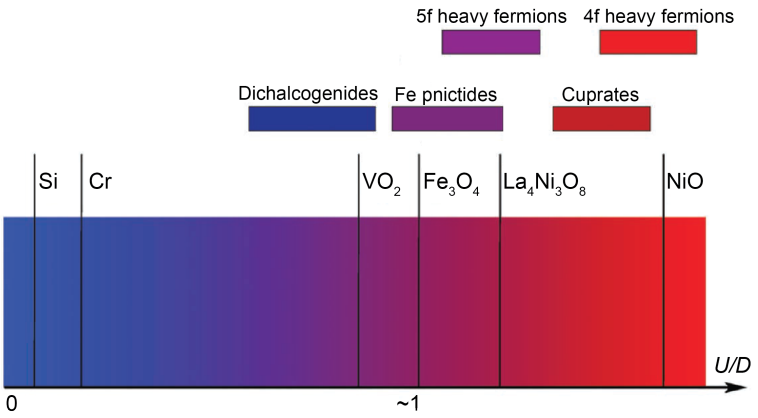

Figure 2.3: Examples of materials with inherently correlated electron systems plotted as a function of U/D where U is the strength of Coulomb interaction between electrons and D is the electron bandwidth. Modified from [21].

These approaches are successfully utilized in a large number of devices. On the other hand, high E_{int} can be provided by the substance itself which is the case for materials with intrinsically correlated electron systems.

Correlated materials exist in a great variety (a few examples are shown in Fig. 2.3) and possess a broad spectrum of functional properties originating from the interplay between the electron-electron interactions, lattice and band structure, and magnetic degrees of freedom. This produces such fascinating phenomena as the high-temperature superconductivity [115] and the metal-insulator transitions [116, 117]. A large number of relevant energy scales generates rich phase diagrams of competing ground states with different symmetries [118]. The transition between the ground states can be performed by tuning one or the other parameter of the electron system which shifts the balance towards one of the competing states.

Despite the great interest, the problem of theoretical description of correlated materials remains relevant due to a high complexity of these systems.

2.3 Confined electron systems

As most physical models, the concept of the band structure is an approximation. When one describes a movement of electrons in solids, usually an infinite periodic potential is considered [119]. It gives good results in the bulk when dimensions of the system constitute millions of unit cells. Such an approach, however, no longer holds if the system is confined to an effectively finite length scale in one or more dimensions. In this case, the behavior of the electrons may significantly deviate from expectations based on bulk models.

Historically, the studying and the theoretical description of low-dimensional systems has gone hand in hand with the semiconductor science. The effects appearing in such confined objects cause a large interest not only scientifically but with respect to device applications. Size effects may modify most of the physical characteristics of the system as practically all of them are sensitive to band structure modifications. Quantum confinement takes place when the length scale of at least one of the dimensions of the system approaches the Fermi wavelength or the inelastic mean free path of the electrons.

Low-dimensional systems are usually classified into three categories: 2D systems which include thin films, superlattices and interfacial layers; 1D systems such as nanoscale lines and chain atomic structures; and 0D systems such as quantum dots, clusters and colloids. These three cases can be thought of as a confinement of an electron system in higher dimensions, causing a gradual modification of its electronic structure. A schematic illustration of such modifications for a free electron system is shown in Fig. 1.1 of Ch. 1.

In the most studied category – 2D systems – the amount of data collected is tremendous. Such materials are fabricated from all common classes of solids starting from widely used two-dimensional electron gasses in AlGaAs layers [120] and finishing with complex correlated materials [7, 10] and atomic layers such as graphene [121] or MoS_2 [122]. In a simple case of a two-dimensional free electron gas, the motion of the electrons can be described as [123]:

$$E = E_n + \frac{\hbar^2}{2m}(k_x^2 + k_y^2), \tag{2.7}$$

where k_x and k_y are the wave vector components for motion in the system plane, m is the effective mass of the carriers and E_n are quantized energy levels arising from the quantum confinement perpendicular to it. The density of states in the limit of low temperatures can be then represented as:

$$D_{2D}(E) = \frac{m}{\pi\hbar^2}\sum_n (E - E_n)\Theta(E - E_n) \tag{2.8}$$

where Θ is the Heaviside step function. The density of states is therefore given by a set of steps as function of energy, the steps of height $m/\pi\hbar^2$ being located at E_n. A comprehensive review of the properties of simple 2D electron systems and existing theoretical models describing them can be found in [124]. More complex phenomena appearing in thin films and at interfaces of correlated materials are summarized in [7,10]. Recent advances in growth techniques of complex materials such as pulsed laser deposition of molecular beam epitaxy made it possible to grow even unit-cell-thick layers of these substances that preserve the material functionality [52].

For one-dimensional electron systems, the description is similar with the difference that their electrons are confined in the radial direction with the energy values $E_{m,n}$ as bottoms of one-dimensional subbands:

$$D_{1D}(E) = \frac{1}{\pi\hbar}\sum_{m,n}\sqrt{\frac{2m}{E-E_{m,n}}}\Theta(E-E_{m,n}) \tag{2.9}$$

As well as the previous case, one-dimensional systems have been fabricated in great variety using different methods [125–127] including magnetic nanolines [101], nanoline heterostructures [128] and especially interesting for applications carbon nantobues [129].

The most interesting case for this work is the case of zero-dimensional systems also known as quantum dots or artificial atoms [15, 130]. Quantum dots are usually fabricated by confining a material in one dimension by growth and then restricting it in two perpendicular directions by etching or an electrostatic potential. Following the discussion above, the density of states for such objects is just a set of δ-functions as there is no free movement possible in any direction. Such a spectrum resembles the energy structure of a single atom and a quantum state of a dot can be described by a coherent many-body wavefunction with a single macroscopic phase. This defines one of the common names of the system. First quantum dots were realized in I-VII and II-VI semiconductor compounds [131] in which the influence of the size effects on the excitonic absorption spectra was discovered. Later, quantum dots were fabricated from various classes of compounds and their potential as model systems for studying basic quantum mechanical effects (which can be used for example for qubits applications [132]) was understood. One of the most interesting features of such devices is the possibility to tune their properties by changing size constraints or applying gate fields. In devices, semiconductor quantum dots are used as light emitters [133] and single electron transistors [130]. The field of application for the new class of quantum dots fabricated of correlated materials is yet to be revealed [114, 134, 135].

Chapter 3

Sample fabrication

3.1 Technological process overview

The fabrication of oxide nanostructures is a complex process that consists of numerous steps. In the beginning of this chapter I give a basic and short overview of the technological process used for the fabrication, describing the main ideas behind it. In the following sections, every technological step will be discussed in more detail.

The process of nanostructuring for complex oxides, developed during my work, is based on the patterning of pulsed laser deposition (PLD) grown epitaxial thin films using a hard mask patterned with electron beam lithography (EBL). In the first step of the process, a substrate ($SrTiO_3$ (100) and $DyScO_3$ (110) were used) is chemically cleaned and then annealed *in situ* at a high temperature in a UHV chamber with O_2 background pressure, to form an atomically flat, single-phase terminated surface [136] and to prepare it for the epitaxial growth of a thin film (see Sec. 3.2). After the preparation, a thin film of $SrRuO_3$ is epitaxially grown on the substrate in the same chamber using PLD (see Sec. 3.3).

In the next step, the film is patterned into nanostructures using EBL (see Sec. 3.4). The patterning utilizes the top-down approach which allows to create systems of nanostructures with high reproducibility. At the same time, their form and arrangement may be varied as desired. For this to be done, a layer of e-beam resist, spin-coated on the sample surface, is exposed to a focused electron beam and developed creating a negative mask for a future nanostructure (see Sec. 3.4). On top of this mask, a thin layer (about 10-20 nm) of amorphous Al_2O_3 is deposited by PLD. After the resist lift-off, the resulting structure of Al_2O_3 serves as a positive hard mask for dry etching with Ar ions. That removes uncovered parts of $SrRuO_3$, ending up with the desired $SrRuO_3$ nanostructure. In the last step, if necessary, the residual Al_2O_3 can be etched away using a weak basic

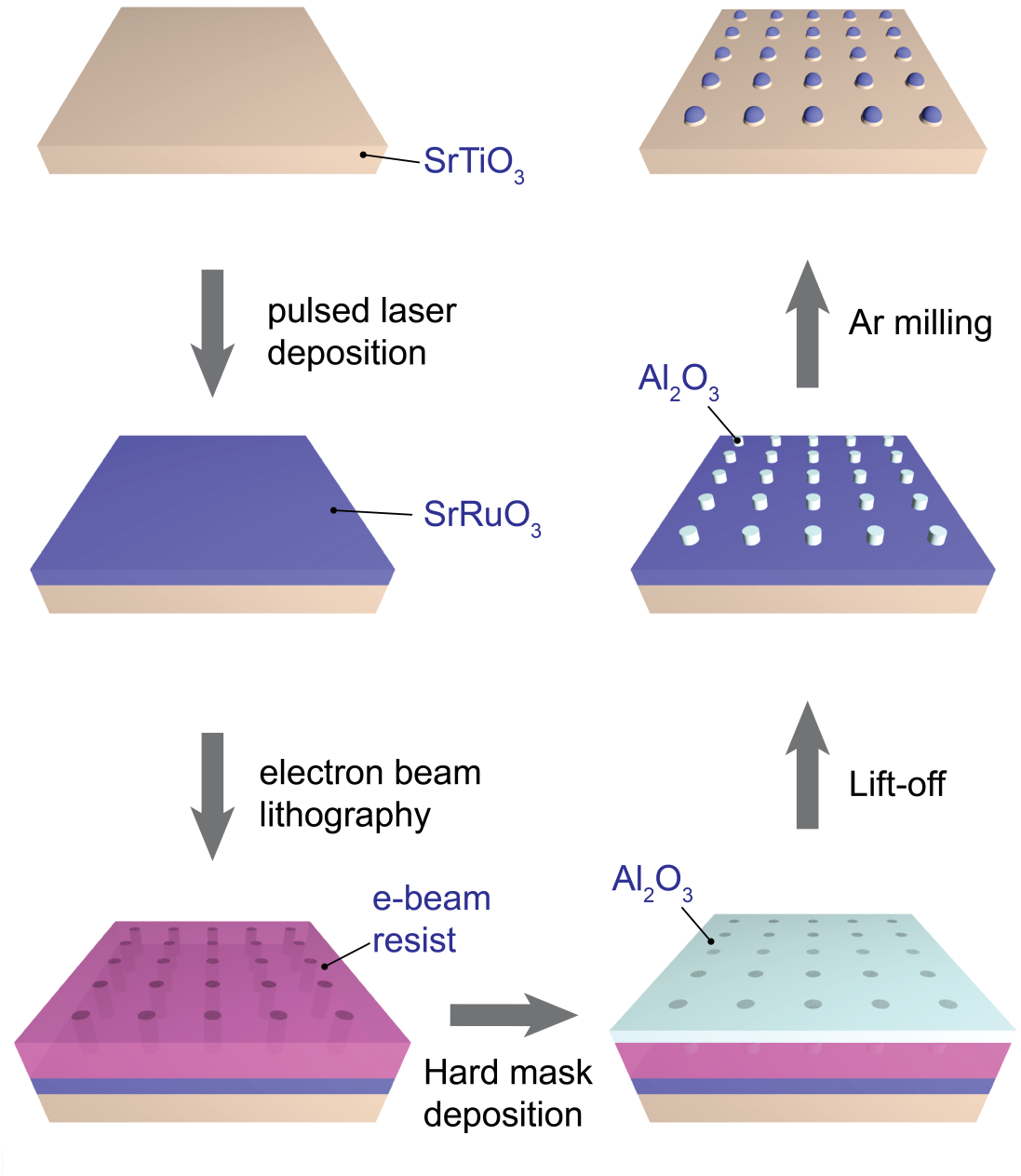

Figure 3.1: Overview of the sample fabrication process.

solution.

The fabrication process in graphical representation is shown in Fig. 3.1.

For the two types of nanostructures (nanodots and nanolines) fabricated during my work, two different substrate materials - $SrTiO_3$ (100) and $DyScO_3$ (110) - were used. This was necessary for the following reasons. $SrTiO_3$ is a commonly used substrate due to its high stability and the cubic lattice with the bulk lattice parameter of 3.905 Å matching many other frequently used perovskite materials, including $SrRuO_3$ (the lattice mismatch of $SrTiO_3$ with the pseudo-cubic lattice of $SrRuO_3$ is 0.64 %). However, one property of $SrTiO_3$ makes its challenging for some applications involving electronic transport. Oxygen vacancies that are intrinsic to $SrTiO_3$ and the formation of which is greatly facilitated under the influence of some factors (for example, Ar milling, used in this work), make the material electrically conducting that creates undesirable leakage currents during measurements. For this reason, for nanoline samples, $SrTiO_3$ was replaced by $DyScO_3$ that remains perfectly insulating after ionic irradiation.

3.2 Substrate treatment

As was explained in Section 1.1, one of the main challenges for fabrication of complex heterostructures is to achieve a high quality and purity of the materials. For this, it is of crucial importance to ensure that the substrate surface is clean enough to grow highly pure epitaxial layers.

All substrates used in this work were delivered by two vendors - CrysTec (Germany, [137]) and Shinkosha (Japan, [138]) - as 5×5 or 10×10 mm^2 rectangular pieces of one-side polished material with thicknesses of 0.5 or 1 mm. The substrate cleaning procedure was the same for all materials and consisted of the following steps:

- Gentle wiping of the substrate surface using lens paper moistened with isopropanol;
- Consecutive cleaning in acetone (10 min), isopropanol (10 min) and ultra pure water (10 min) using an ultrasonic bath;
- Drying with a nitrogen gun.

For the cleaning, substrates were placed in a teflon holder able to contain up to nine substrates and then immersed into a plastic or glass beaker filled with a corresponding liquid. All beakers were used only for one type of solvent to avoid cross-contamination.

After the cleaning, substrates have to be annealed and terminated to provide atomically flat single-phase surface required for epitaxial growth. This can be

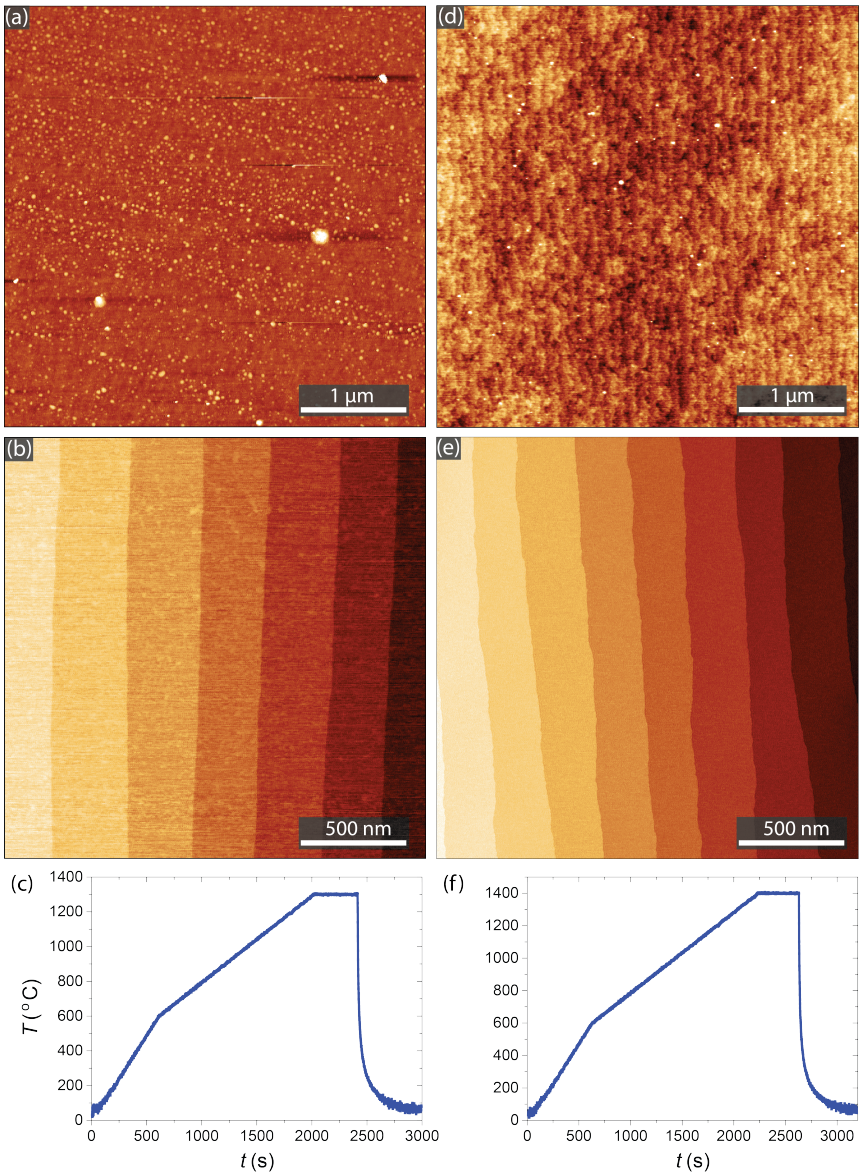

Figure 3.2: Topographic AFM images of a $SrTiO_3$ (100) substrate (a) before and (b) after the high-temperature annealing in the vacuum chamber. (d,e) The same for a $DyScO_3$ (110) substrate. (c,f) The corresponding temperature profiles during annealing.

done in two ways. A typical and widely used method of substrate preparation [139, 140] implies chemical etching using a buffered HF solution followed by a long-time annealing in an oven with molecular oxygen at ambient pressure. This method was used to prepare substrates during the first half of this work. However, this technique has a number of disadvantages: it is time consuming due to the

approximately eight-hour-long annealing, it takes place *ex situ* and it requires the use of the highly hazardous HF acid.

To solve these problems and to increase the efficiency, a new method of substrate termination was developed by colleagues in our group [136]. It consists in the *in situ* annealing of a substrate right before the epitaxial growth in a UHV chamber using a CO_2 laser system with a wavelength of 9.27 μm at low molecular oxygen background pressure. At this wavelength, many oxide materials are not transparent. Therefore, it is possible to directly couple a substrate to the radiation, in contrast to the case of heating with infrared semiconductor lasers which require the use of a back-plate. The temperature and pressure during annealing differ depending on the substrate material. For the two substrate materials used in this work, the annealing parameters were the following: for $SrTiO_3$ (100) the peak temperature of the anneal was kept at 1300 °C with a O_2 pressure of 0.08 mbar. For $DyScO_3$ (100) these parameters - 1400 °C and 0.08 mbar. Examples of corresponding temperature profiles are shown in Fig. 3.2(c,f). Substrates are first gradually heated to the desired annealing temperature at a rate of 1-2 K/s. After achieving the peak temperature, the substrate is kept at it for a certain time, after which the temperature is either gradually reduced to match the growth conditions or sharply quenched to take a snapshot of the surface. The annealing time for both substrate types was 200 s. Figure 3.2(a-d) depicts how substrate surfaces transform after the treatment for $SrTiO_3$ (100) and $DyScO_3$ (110). As received substrates were polished by the vendor with a surface roughness of about 2 nm (Fig. 3.2(a,d)). After the annealing, the substrate surface converts to atomically flat terraces of one unit cell height (Fig. 3.2(b,e)). The width of the terraces depends on the substrate miscut and varies from substrate to substrate from about 50 nm to several micrometers. Besides the advantages listed above, this method also allows to grow $SrRuO_3$ films with improved magnetic properties compared to chemically treated substrates, as shown in Section 5.2, which again indicates better surface quality. In the following description, results obtained with *in situ* annealed substrates are demonstrated, unless noted otherwise.

3.3 Thin films epitaxy

3.3.1 Growth system overview

After the cleaning and *in situ* annealing procedures, a substrate is ready for the epitaxial growth which is done using the pulsed laser deposition (PLD) technique. The PLD chamber is a part of a larger vacuum system which includes several growth and processing modules. An overview of the system is given in Figure 3.3. Two glove boxes with nitrogen atmosphere are used as the entrance to the

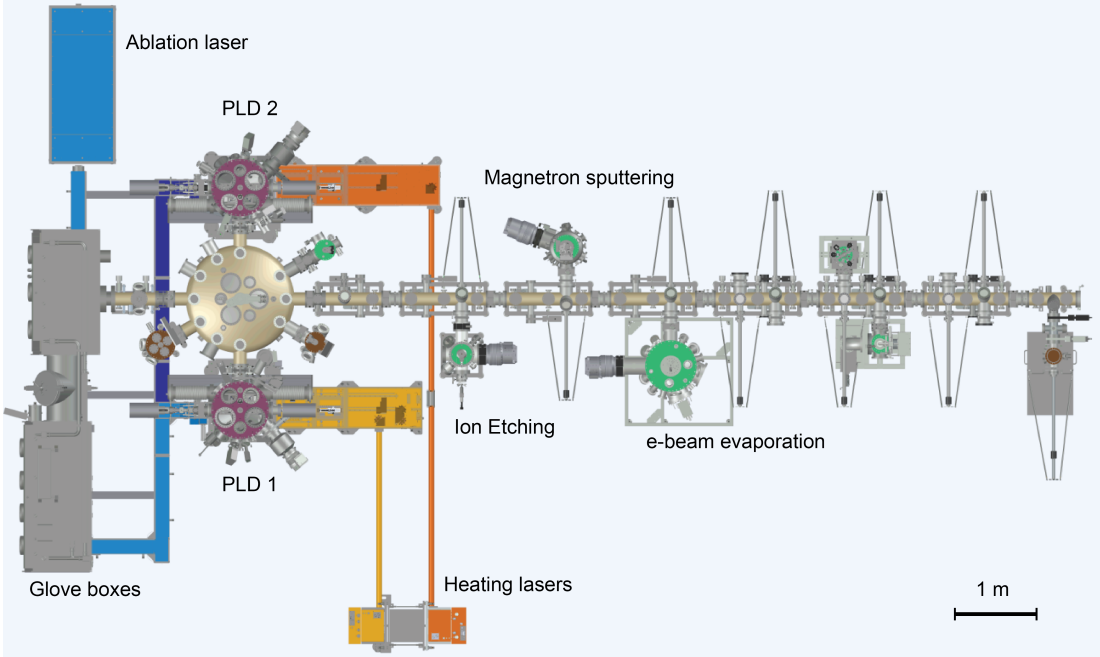

Figure 3.3: Schematic top-view image of the deposition system including pulsed laser deposition, sputtering and dry etching modules.

system. One of the glove boxes is used for target preparation - polishing and cleaning of materials to be deposited - and mounting them in target holders (see Fig. 3.4(b)). In the second glove box, substrates are mounted onto tantalum sample holder plates (see Fig. 3.4(a)) and loaded into a load-lock chamber where they are pumped down for transferring into the UHV environment. From the load-lock, samples and targets are transferred into one of two PLD modules, storage chambers or a linear transport tunnel using a radial module equipped with a robotic arm.

The linear transport tunnel is connected to chambers for Ar milling, e-beam evaporation and magnetron sputtering. The description of the Ar milling module, which was essential for this work, is presented in Sec. 3.4.3. Between all modules, including the PLD chambers, the samples can be transferred without breaking the vacuum.

3.3.2 Target preparation

One of the important parameters for successful epitaxy is the quality of the target material. Prior to deposition, targets have to be cleaned and polished, which is done in a nitrogen-filled glove box. The polishing procedure consists of the following steps:

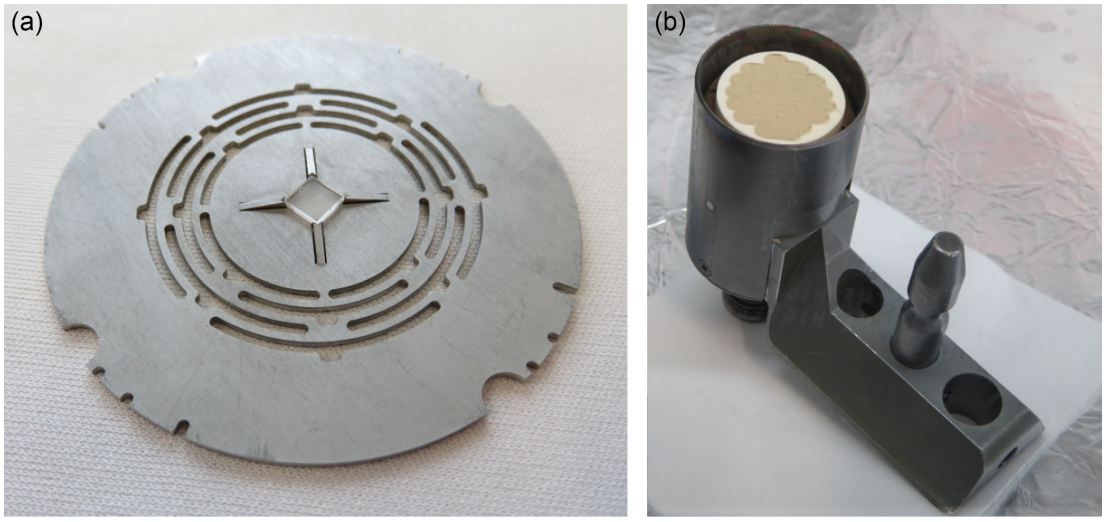

Figure 3.4: (a) A tantalum plate used to transfer substrates between the epitaxy system modules. A $5 \times 5\,\mathrm{mm}^2$ $SrTiO_3$ substrate is mounted in the middle. (b) A holder for PLD targets with an Al_2O_3 target installed. The target diameter is 1 inch. The ablation path on the target surface is visible.

- The target is released from a target holder and its surface is polished on a fine SiC sand paper to remove all visible defects and traces from former ablations;
- The material is then sonicated in isopropanol to remove dust and other contaminants;
- After that the target is annealed at low temperature (about 80 °C) to dry and degas it.
- The target is mounted back onto the target holder and its new height is measured to adjust the target position during deposition.

The last step of the preparation is done in the PLD chamber directly before the growth - the target surface is pre-ablated to remove possible residual contaminants and provide a smooth homogeneous surface for the ablation. The pre-ablation is done at the same pressure and laser fluence that are used for the epitaxial growth. The number of ablation cycles depends on the material and usually ranges between one and three.

It is important to mention that numerous laser pulses incident on the same location of a target may cause damage and modifications of the target material. For example, it was shown [141] that long ablation of an Al target causes an increase of the particulates density in the film. Also, a deterioration of magnetic

properties was noticed in $SrRuO_3$ thin films deposited from a target subjected to multiple ablation cycles without polishing of its surface (see Sec. 5.2 for more details). To avoid this, the target surface was polished and cleaned every time prior to the deposition session.

3.3.3 Pulsed laser deposition of $SrRuO_3$

Pulsed laser deposition is one of the most popular techniques for epitaxial growth of complex materials [142,143]. It was first realized soon after invention of lasers in the 1960's [144] but gained its popularity and widespread use in the late 1980's after it was applied to the growth of high-T_c superconductors, such as YBCO [145]. A big advantage of PLD that allows its application to the growth of a wide range of complex substances - from pure elements to biological compounds - is the highly stoichiometric transfer of material that is achieved when a laser pulse of high fluence is absorbed by a small volume of the target material causing its ablation [146]. The ablated species are then transferred through a plasma plume to a substrate with almost the exact target stoichiometry, in contrast to the thermal evaporation process, where the flux of every constituent element depends on its vapor pressure. PLD has become especially popular for the growth of complex oxide materials as the molecular oxygen gas, present in the chamber during deposition, helps not only to reduce the kinetic energy of the ablated species in the plume and prevent the surface damage, but also provides the reactivity necessary for oxidation processes. The background pressure during growth can be varied in a wide range, from UHV to several millibars, which also provides an advantage over other methods in growing materials, some of which rapidly lose oxygen at low pressure [146].

A schematic image of the PLD deposition process is shown in Figure 3.5. A tantalum sample holder plate with a mounted substrate is placed on a heating stage directly under the target and set to a target-substrate distance of 56 mm. The chamber is then filled with molecular oxygen, after which the substrate is annealed at high temperature as described in Sec. 3.2. After the high-temperature anneal, the substrate is gradually cooled to the deposition temperature at a rate of 1 K/s. For the deposition, the target is ablated using a KrF excimer laser with a wavelength of 248 nm. A target-substrate distance is set to 56 mm. After every laser pulse, the target is shifted laterally according to a pre-defined path to use a large surface area of the target. Two consequent ablation spots may overlap with each other by a defined value. The substrate temperature during growth is measured on its back surface using a pyrometer and controlled with the help of a feedback loop. The pressure in the chamber can be adjusted by varying the gas flow and the pumping speed using a variable shutter in front of the turbo pump.

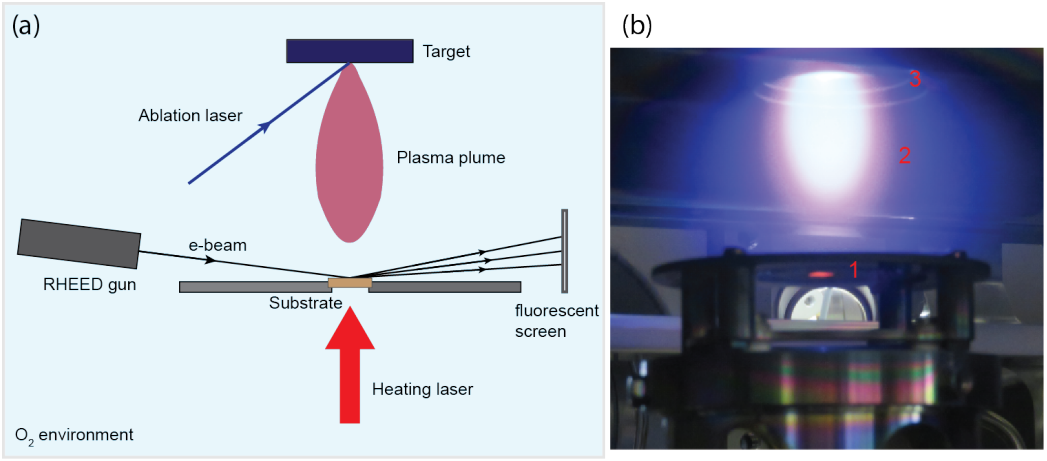

Figure 3.5: (a) Schematic illustration of the PLD deposition process. (b) Photograph of the ablation process where (1) denotes a heated substrate, (2) a plasma plume, (3) a target of $SrRuO_3$.

Specific deposition parameters depend on the substrate and target materials and desired film properties. Important parameters to control are: substrate temperature during deposition (T), type of gas and its pressure (P), energy density of the laser beam on a target (F), and laser pulses repetition rate (f).

For $SrRuO_3$, the deposition parameters were optimized to obtain optimized magnetic properties together with a smooth film topography. Sec. 5.2 presents a detailed discussion of the magnetic properties. The resulting optimized deposition parameters for two substrates - $SrTiO_3$ (100) and $DyScO_3$ (110) - are listed in Table 3.1. The growth rate is specified in the amount of laser shots necessary to deposit one-unit-cell-thick layer of material. This number is approximate as it also depends on the condition of a target. A description and characterization of the grown films are given in Sec. 4.1.

3.3.4 RHEED

Important real-time information on the substrate surface and the growing film has been obtained using reflection high energy electron diffraction (RHEED). The technique was first applied by Nishikawa and Kikuchi [147] in 1928 to analyze properties of a cleaved calcite surface. In the 1980's, after RHEED found widespread application to characterize thin film growth, RHEED growth oscillations were discovered by Harris, Joyce and Dobson [148].

In RHEED, a beam of high-energy electrons (typical energies are 5-50 keV), accelerated by an electron gun, reflects from a smooth substrate surface at a glancing angle of about 1° and falls onto a phosphorous screen creating a diffraction

Table 3.1: PLD deposition parameters of $SrRuO_3$ for substrates used in this work. (old) - deposition parameters used by previous generations of growers, (chem.) - parameters optimized for chemically terminated substrates, (*in situ*) - pararmeters optimized for *in situ* annealed substrates.

Substrate	T, °C	O_2 P, mbar	F, J/cm^2	f, Hz	Overlap, %	Growth rate, pulses/u.c.
$SrTiO_3$ (old)	660	0.1	1.2	1	50	≈ 45
$SrTiO_3$ (chem.)	700	0.08	2.1	1	50	≈ 28
$SrTiO_3$ (*in situ*)	680	0.08	2.5	1	50	≈ 22
$DyScO_3$ (*in situ*)	700	0.015	2.5	1	50	≈ 19

pattern. The pattern can be analyzed to obtain information about properties of the substrate, such as the surface reconstruction and roughness [149,150]. Also, it gives access to information about migration kinetics that can be used to monitor the crystal growth in real time [151, 152].

Depending on the kinetics of adatoms on the substrate surface during growth, an interplay of different growth regimes can be observed. In a simplified (however, not entirely correct) description, two growth modes may be distinguished. During layer-by-layer (also known as Frank-van der Merwe) growth [153, 154], material nucleates on the surface forming separate two-dimensional islands that grow in size until the entire layer is complete. The formation of a new layer does not start before the previous one is finished. When the layer-by-layer growth occurs, periodic oscillations can be observed in a RHEED intensity profile. Modulation of the intensity in this case is caused by changing surface roughness during the substrate coverage with a new layer. One oscillation corresponds to the completion of one-unit-cell-thick layer of material. On the other hand, during step-flow growth [155], adatoms have enough energy to reach energetically favorable positions at surface steps and material nucleates as terrace diffusion without the formation of distinct islands. In that case, growth oscillations are not observed.

Our RHEED system produces an electron beam with 30 kV energy. Figure 3.6 shows how the RHEED diffraction pattern of a $SrTiO_3$ (100) substrate evolves during heating to 1300 °C (Fig. 3.6(a-d)), cooling to the deposition temperature of 680 °C (Fig. 3.6(e)) and with the growth of a 12-nm-thick $SrRuO_3$ thin film (Fig. 3.6(f)). Rectangles show the areas where the RHEED intensities have been measured. The data is recorded for sample #168. Figure 3.6(g) shows a

recorded intensity profile for the same sample from window #2 (red). No growth oscillations were observed for this sample, which may be due to step-flow growth or imprecise alignment of the electron beam. Figure 3.6(h) depicts an intensity evolution from a different sample (#41), demonstrating good growth oscillations with layer-by-layer growth.

From the comparison of these two intensity profiles, it is seen that the noise level and the stability of patterns can differ substantially. This highly depends on the electron beam settings, substrate position on a sample plate, its stability and orientation, and external conditions in a laboratory, such as electric and magnetic fields and mechanical vibrations. In general, the outcome of a particular growth is difficult to predict.

The analysis of intensity profiles also reveals that there is a transition in the growth mode of $SrRuO_3$ which happens at about 110 s in Fig. 3.6(h). This is presumably related to a termination conversion of $SrRuO_3$ from RuO_2 to SrO during growth of the first unit cell [156, 157]. After the transition, the film grows with the rate of approximately 20-22 laser shots per one unit-cell-thick layer.

3.4 Patterning

In this section, I describe the technological processes that allowed for the creation of nanostructures from thin films. For the description, I concentrate on the patterning of nanodots samples, as it constitutes the major part of my work. Fabrication of nanolines is discussed separately in Chapter 6. Detailed recipes for the patterning of all fabricated structures are given in Appendix A.

3.4.1 Electron beam lithography

Basics

Electron beam lithography is a patterning technique based on the irradiation of a properly sensitive resist material with a focused beam of electrons [158]. Before the exposure, a sample is covered with a thin (the usual thickness ranges from several dozens to several hundreds nm) layer of an e-beam resist, normally by spin coating. The sample is then placed in a UHV chamber, where the e-beam resist layer is irradiated with a focused electron beam. Interaction between electrons in the beam and the resist material causes the chemical modification of the latter (e.g., by breaking its molecules). This allows to remove the modified (in case of positive resist) or unmodified (in case of negative resist) material with a special solvent, which is called developer. Thereby, after the exposure and developing, the remaining e-beam resist may serve as a positive or negative mask for the desired nanostructure.

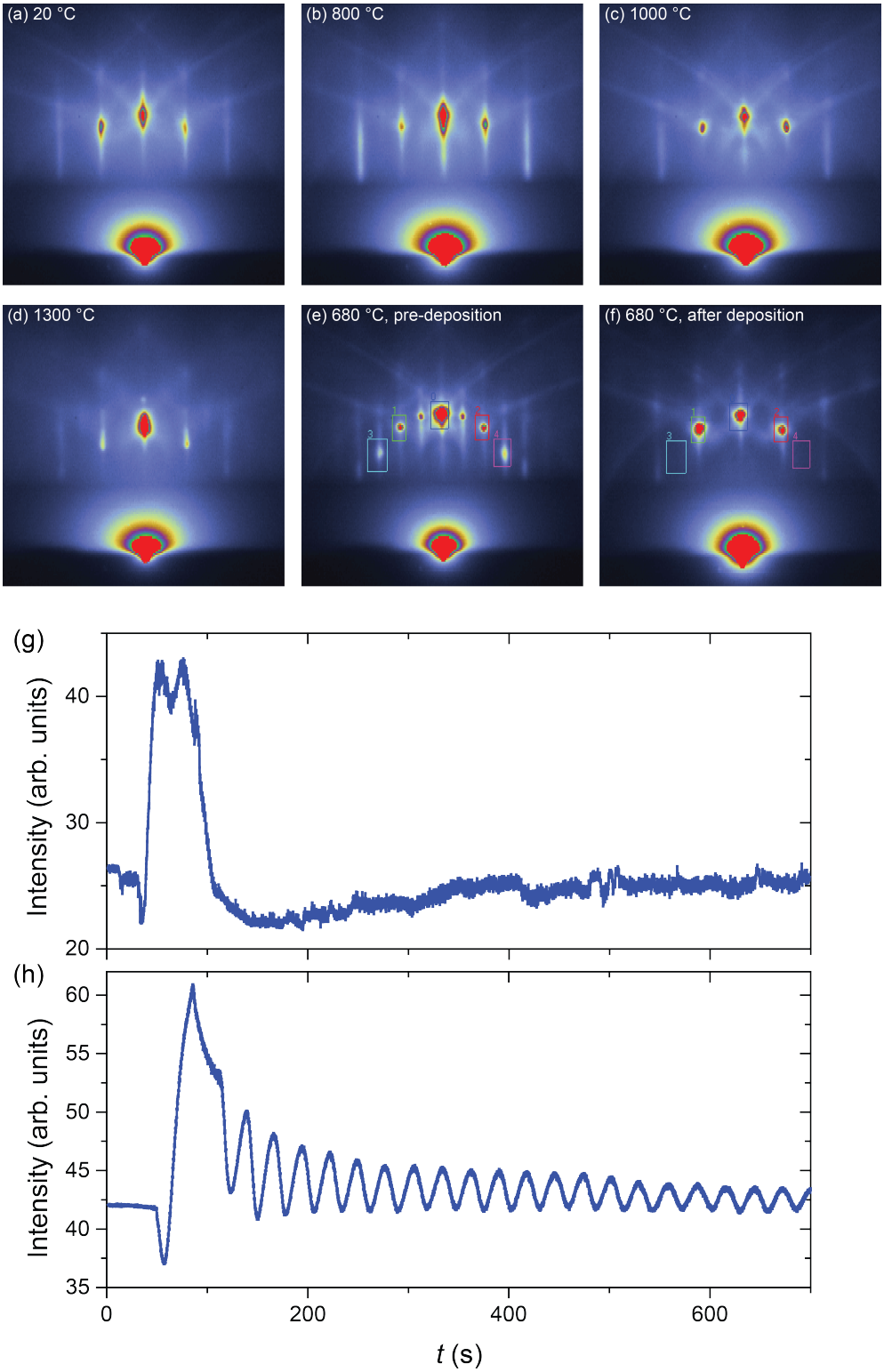

Figure 3.6: (a-f) Evolution of the RHEED pattern for a $SrTiO_3$ (100) substrate during a high-temperature annealing (a-d) and consequent growth of a $SrRuO_3$ film (sample #168) (e-f). The rectangles indicate the areas of the RHEED intensity monitoring. (g) Intensity record taken during growth for the same sample, intensity window #2. (h) Intensity record for a different sample illustrating good growth oscillations (sample #41).

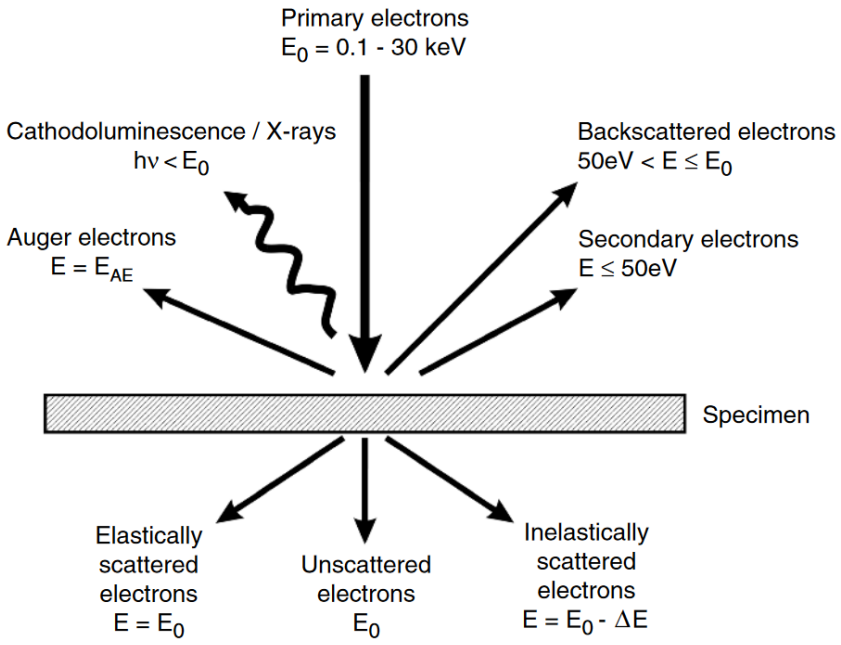

Figure 3.7: The different types of secondary radiation caused by the interaction of the primary electron beam with the sample. Adapted from [159].

Using modern electron optics systems, the electron beam can be focused to several nanometers in diameter. However, the final resolution of the exposure is largely determined by other factors. The usual energy of the electron beam is in the range of several dozens keV. Electrons of such high energy penetrate not only into the resist layer but also deep into the underlying substrate and scatter there in a volume that, depending on the energy, can reach up to several hundred μm^3. The interaction between electrons and the substrate material triggers many physical processes [159]. This includes several types of secondary radiation (see Fig. 3.7), among which secondary and back-scattered electrons and x-rays influence the resist in the vicinity of the point of incidence of the beam. The amount, area and impact of this additional exposure depend on the beam energy, substrate material, dwell time of the beam and resist system. Besides this, e-beam resists which consist of long polymer molecules introduce additional limitation of the resolution depending on the size of these molecules [160]. Such an abundance of significant factors renders the optimization of exposure parameters non-trivial and unique for every structure and material system.

Starting from a clean sample, the e-beam lithography requires the following technological steps to be performed:

- The sample is spin-coated with a single or multilayer of e-beam resist. The thickness of the layer is determined by the time and velocity of spinning as

well as by the resist material and the concentration of the resist solution.

- Optionally, an additional layer of a special conducting polymer may be used to help dissipate the volume charge developing during exposure. If used, this second layer is spun on top of the first one.
- The sample is baked out on a hot plate to polymerize the resist material.
- The sample is loaded into a UHV chamber and exposed by an electron beam according to the design layout.
- After the exposure, the resist is developed, removing exposed parts of the layer for a positive resist. After this the sample is ready for etching or hard mask deposition.

Exposures were done in a 100 keV electron beam lithography system JEOL JBX6300 [161]. The rather high voltage yields electrons that penetrate deeper into substrate, which reduces the amount of secondary radiation absorbed by the resist, improving the resolution. The system is located in a dedicated clean room, with a mechanically and temperature-stabilized environment as well as shields against electromagnetic radiation, which minimizes the influence of external factors on the exposure process and reduces drifts.

E-beam resists

Since different resist compounds have different properties, the choice of a system for a particular experiment depends on the characteristics of a nanostructure, such as feature size, density, area, desired hard mask thickness, post-processing steps, etc. During this work, two resist materials were used. The first one is a widely used positive resist poly(methyl methacrylate) (PMMA, Allresist GmbH, Germany [162]). It can be deposited as a single or double layer. In the latter case, the underlying layer consists of a softer resist material. This layer is more sensitive to electrons to allow for an undercut profile after the development. This undercut reduces the resolution, but facilitates the lift-off process due to easier access of solvent to the resist. Therefore, such a system is good for large structures such as markers and contacts. The second resist material used is poly(α-methyl styrene-co-α-chloroacrylate methylester) (CSAR, Allresist GmbH, Germany [163]). This resist provides superior resolution and requires smaller exposure dose. It, therefore, is more suitable for fine small scale structures. This resist was used for exposing the nanodots and nanolines.

Since both $SrTiO_3$ and $DyScO_3$ are insulating materials, it is necessary to spin-coat an additional layer of conducting polymer on top of the resist. The layer helps to carry away the surface charge developing in the insulators during exposure and

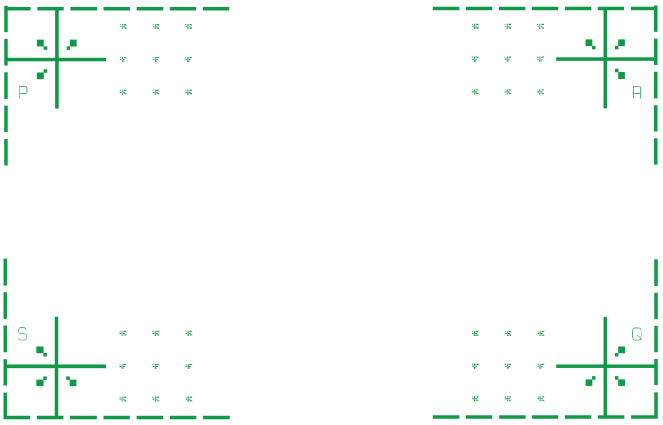

Figure 3.8: The system of four global marks used for exposure layers alignment. Marks are positioned in corners of the exposure field.

therefore significantly reduces structural distortions. A water soluble Espacer 300Z (Showa Denko, USA [164]) was used for this task. The layer was removed before the developing by several seconds of DI water rinse.

After the exposure, resists are developed by immersing into a developer liquid for a definite time. For a certain resist material different developers may be used which also influences the output of the patterning.

Markers

For structures of higher complexity multiple exposures are required. This can be necessary, for example, when nanostructures of functional materials have to be contacted by metallic electrodes. In this case, a system of global markers has to be created on the substrate to provide references for the alignment of different exposure layers with respect to each other. The mark system used in my work is shown in Fig. 3.8. Four marks are placed in corners of the exposure area, to be used for coarse adjustment. For fine adjustment, every large mark is accompanied with a 3×3 system of smaller marks. Their positions relative to large marks are known. A plurality of those is necessary because every mark can be used only once, as it is exposed and destroyed during the alignment procedure. The set-up allows for automatic mark alignment, however, all alignments were done manually in this work.

Layouts

All structure designs and layouts were created using the eLine software (Raith, v. 5.0). The designs were then processed in the GeniSys Beamer software to generate the data format required for the e-beam writer.

The two main types of structures used are arrays of nanodots and nanolines both patterned in $SrRuO_3$. In this section, layouts for nanodots samples are

described. For nanolines, the principles are similar and the corresponding sample designs are shown in Chapter 6.

Nanodots of $SrRuO_3$ were fabricated mainly in rectangular arrays. As explained in Sec. 5.1.4, the dots were measured using SQUID magnetometry. Since, due to the limitations of the fabrication process, the coverage of a substrate with dots is not large - 5-10% of the area depending on the dot size - the area covered with arrays has to be as large as possible to provide an adequate amount of material for the measurement. Ideally, the entire substrate area should be structured. This requirement imposes rather demanding constraints on the exposure. Due to the substantial exposure area and number of elements, the exposure process requires large time (up to several days). It is, therefore, important to provide for this long duration the stability of exposure parameters. The set-up is well isolated and shielded providing the stable environment for the exposure. Parameters of the electron beam and electron optics, however, may drift over time. Therefore, during long exposures, it is necessary to perform drift and distortion corrections. These were done after every hour of exposure using standard built-in routines of the e-beam writer.

An important problem is the exposure time. It depends not only on the total exposure area but also on the number of elements in a layout. Every arbitrary design needs to be converted into a set of elementary polygons that the writer can understand. This conversion can be done in the Beamer software using different fracturing methods. Fig. 3.9 demonstrates a couple of examples of fracturing - "conventional" (Fig. 3.9(b)) and "curved" (Fig. 3.9(c)) for a circular shape of 200 nm diameter. It is seen that in both cases a circle is divided into a large number of rectangles and trapezoids. Due to significantly increased number of elements after fracturing, the exposure time for samples with circular dots can reach up to several days, which makes it challenging to maintain the system parameters stable during the exposure. On the other hand, rectangular shapes are not fractured and remain single elements after the layout conversion. Together with the fact that for very small objects, close to the resolution limit of the lithography, the shape of the final structure is rounded independent on the designed shape, it makes rectangles a preferred design for the dots. This allows to reduce the exposure time of standard samples from approximately 50 to 10 hours.

Since nanodot arrays are intended for magnetometry measurements, no contacts are required for their structure. This reduces the number of required exposures to just a single one. Dots are grouped into arrays of 200-300 μm size (i.e., to fit the maximum size of the writer's writing field) and the arrays are then multiple times repeated to cover the entire substrate surface, excluding regions close to the edges where the resist thickness and the substrate quality are usually degraded. Two examples of structure layouts for the nanodot arrays are shown

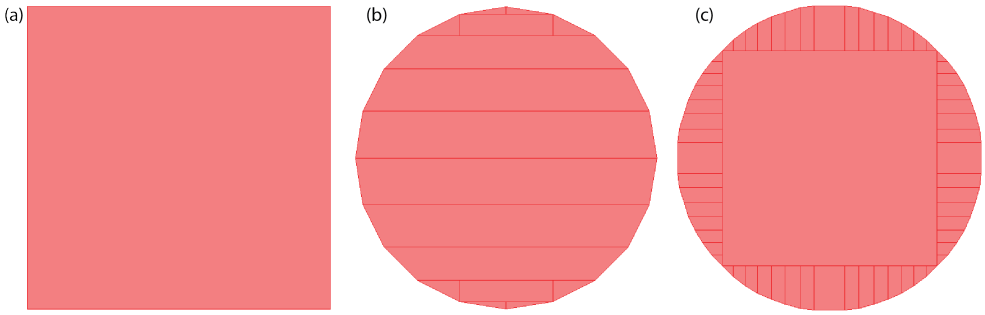

Figure 3.9: Illustration comparing different fracturing methods for rectangular and circular shapes as presented by the GeniSys Beamer software. (a) Rectangles remain as single element after any fracturing method, (b) "Conventional" fracturing for a 200 nm diameter circle, (c) "Curved" fracturing for the same circle.

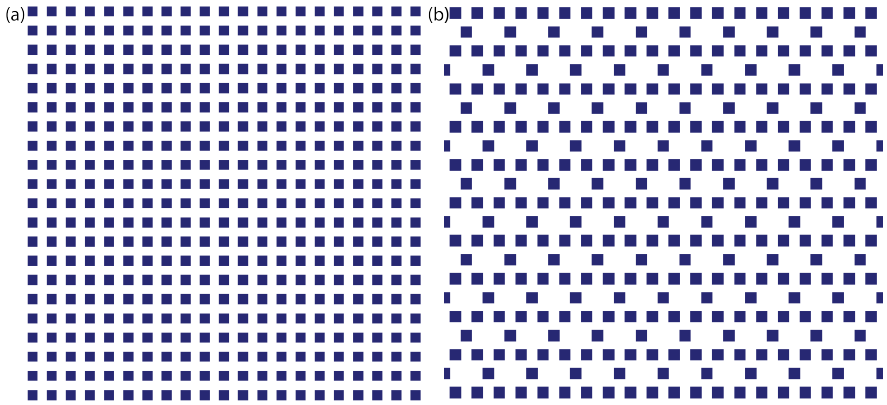

Figure 3.10: Two examples of layouts for nanodots arrays: (a) rectangular lattice, (b) Kagome lattice. The diameter of dots in the arrays is 50 nm.

in Fig. 3.10.

3.4.2 Hard mask deposition

After exposure and resist developing, the sample is loaded into the PLD setup and a thin ($\approx$ 10-20 nm) layer of amorphous Al_2O_3 is deposited on it. This layer serves as a hard mask layer for the ion milling with Ar ions which will be performed afterwards. Al_2O_3 is the material of choice for this layer because it has a low ion milling rate that allows to reduce the thickness of the hard mask and of the resist. As an amphoteric substance it can also be easily dissolved in many bases or acids if necessary.

The PLD deposition parameters for the process are listed in Table 3.2. The values of fluence and repetition rate are moderate due to the fact that the material is deposited on top of a resist layer which is an organic substance and can be

Table 3.2: PLD deposition parameters of amorphous Al_2O_3 for the hard mask layer

Material	T, °C	O_2 P, mbar	F, J/cm^2	f, Hz	Overlap, %
Al_2O_3	room temperature	8×10^{-5}	1.5	3	50

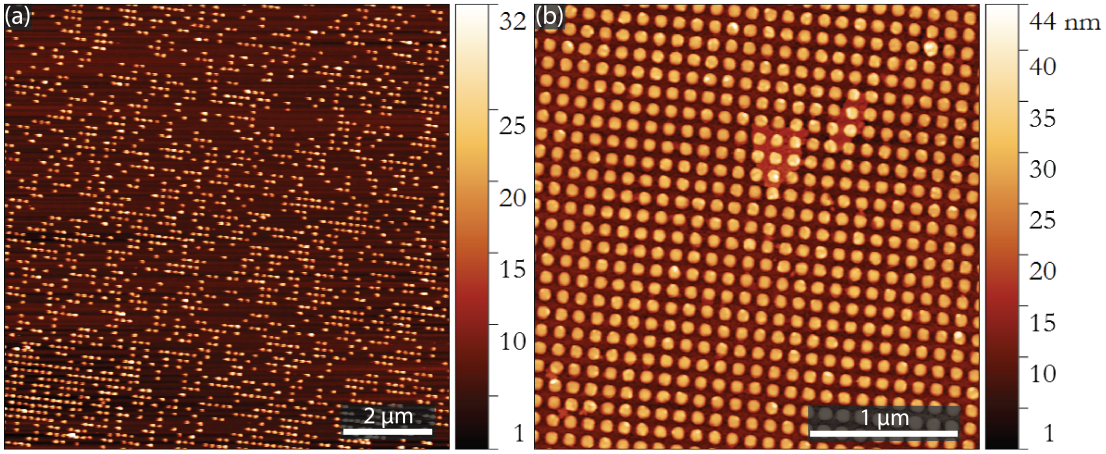

Figure 3.11: AFM images of Al_2O_3 hard masks structured on top of a $SrRuO_3$ film using (a) double-layer PMMA resist and (b) CSAR resist. Both structures consist of similar arrays of 50-nm-diameter dots. This comparison demonstrates the much higher performance of the CSAR resist.

sensitive to heating. Additionally, to improve the layer uniformity, the substrate can be azimuthally rotated during deposition. However, no differences in the layer quality were noticed for cases with and without rotation.

When the deposition is finished, the remaining resist layer, with the Al_2O_3 deposited on top of it, has to be removed to leave only the required hard mask structure on the sample surface. This is done by chemically dissolving it in a remover solution. To facilitate the process, low power ultrasound and moderate heating can be used. After the lift-off, the substrate is additionally cleaned in acetone and isopropanol and exposed to an oxygen plasma to remove residuals of the resist.

A couple of examples of the resulting structure are shown in Fig. 3.11. The structure in Fig. 3.11(a) has been fabricated using a double layer of PMMA resist, while for the structure of Fig. 3.11(b) a CSAR resist has been used. Both dot arrays contain dots with similar diameters of 50 nm. It can be seen that arrays fabricated using PMMA are highly irregular with a substantial part of the structure being missing. This is a general problem that originates from the fact that the $SrTiO_3$ used for the substrate, is an insulator. It therefore

Table 3.3: Standard parameters for the Ar ion etching of $SrRuO_3$

Parameter	Value
Ar flow, sccm	8
Ar pressure, mbar	4×10^{-5}
Discharge voltage, V	41
Beam voltage, V	500
Accelerator voltage, V	100
Beam current, mA	10

tends to accumulate surface charge during exposure. The charge can significantly distort the electron beam causing its deflection, defocusing and, as consequence, degradation of the structure profile. This effect becomes even more relevant with increasing density of a structure. Ultimately, it limits the reachable density as the charge does not have enough time to dissipate. Here comes an important advantage of the CSAR resist to play. The CSAR resist requires by a factor of two smaller exposure dose, that helps to reduce the charging effect, increase the possible density and overall quality of the structure.

3.4.3 Ar milling

After the hard mask has been created on top of a $SrRuO_3$ film, dry etching with a flux of ionized argon is used to pattern the film. This is done using an Ar milling set-up connected to the radial transport line of the epitaxy system. The set-up consists of a UHV chamber equipped with a Kaufman ion source [165] (KDC 40), powered with a source controller (Model KSC1202). The low pressure flux of argon through the source is controlled by a multi gas controller (MKS 647C). A flux of argon atoms is ionized in the discharge chamber by electrons with an energy corresponding the discharge voltage of 41 V. The ion beam is then accelerated towards the sample by a total voltage of 600 V (500 V beam voltage + 100 V accelerator voltage). Ions bombard a sample surface, sputtering the material away. Standard parameters of the process are summarized in Table 3.3.

In the ion-etch chamber, the sample is glued or clamped to a copper or tantalum plate which is placed in the chamber upside down and pressed against a block of metal for cooling. No active cooling is implemented. Since high-energy ions can significantly heat the sample, the etching process is realized in cycles. The surface is exposed to the ion flux for 10 seconds, after which the flux is blocked by a shutter for 20 seconds to cool the sample. The process is then repeated until the desired etching time is reached.

The etching rate can be nonuniform. This can result either from the nonlinearity during a single etching session or from the spread between separate

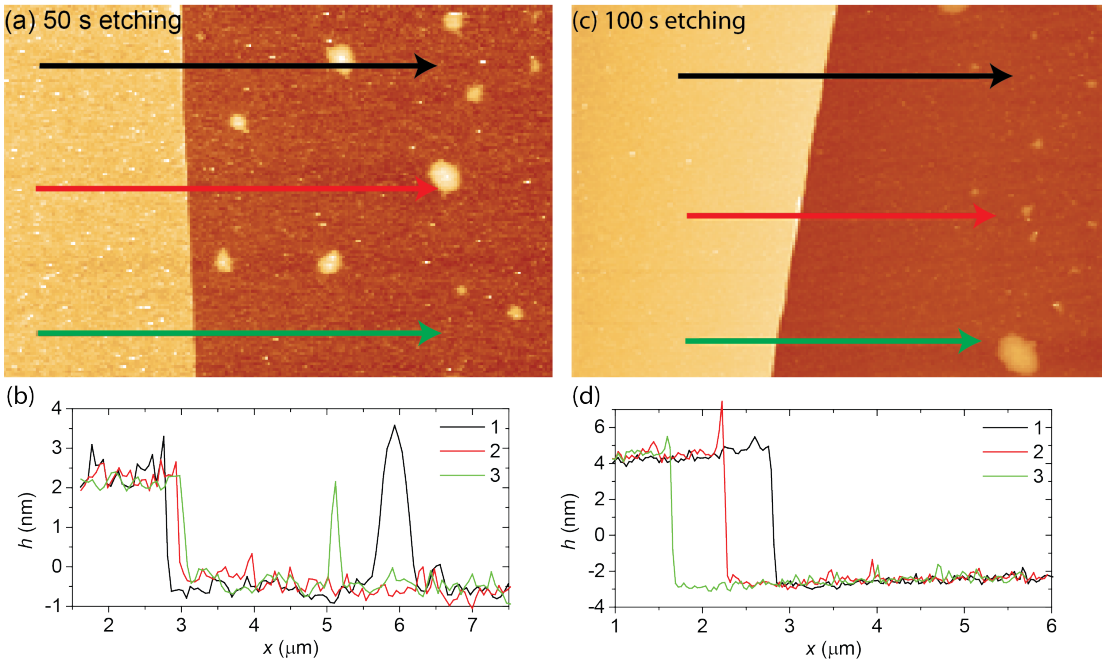

Figure 3.12: AFM images showing results of two Ar milling tests performed on $SrRuO_3$ thin films during (a) 50 s (sample #71) and (b) 100 s (sample #72). The etching was done through a hand-deposited photoresist mask covering a half of a sample. The corresponding height profiles are measured in three positions and shown below.

sessions. Figure 3.12 shows two examples of Ar milling tests performed on $SrRuO_3$ films through a hand-deposited photoresist masks. The film in Fig. 3.12(a,b) has been etched during 50 s and the film in Fig. 3.12(c,d) - during 100 s. Uniform steps of ≈ 2.7 nm and ≈ 7.5 nm are formed correspondingly. That gives etching rates of 3.24 nm/min and 4.5 nm/min, i.e. with almost 30% difference. To take this spread into account, the etching was performed with a margin of $\approx 30\%$ to ensure that the $SrRuO_3$ is etched through its entire thickness.

Chapter 4

Material characterization

This chapter focuses on the physical properties and the morphology of thin films and nanodots of $SrRuO_3$ as fabricated in this thesis. These samples have been structurally analyzed using various techniques to study their properties and assess their quality. Among these techniques are atomic force microscopy (AFM), scanning transmission electron microscopy (STEM), x-ray diffraction (XRD) and electrical transport measurements. Magnetometry measurements, which are undoubtedly also essential for the characterization, are described separately in Chapter 5 as they lead to the major scientific results of this thesis. All results shown here have been obtained using films grown on *in situ* thermally annealed substrates (see Sec. 3.2).

4.1 Thin films of $SrRuO_3$

The quality of nanopatterned devices is largely influenced by the quality of the thin films they are patterned from. Hence, close attention has to be given to the properties of the $SrRuO_3$ thin films prior to patterning.

The epitaxial films of $SrRuO_3$ were grown by pulsed laser deposition on (100) $SrTiO_3$ for nanodot samples and on (110) $DyScO_3$ for nanoline samples. The necessity to use different substrate materials for the two types of structures is explained in Sec. 3.1.

4.1.1 $SrRuO_3/SrTiO_3$ (100)

AFM characterization of the samples

Atomic force microscopy has been performed for every $SrRuO_3$ film right after the growth as it is the fastest method to obtain information about the film surface and morphology. The most common types of signals that the standard AFM

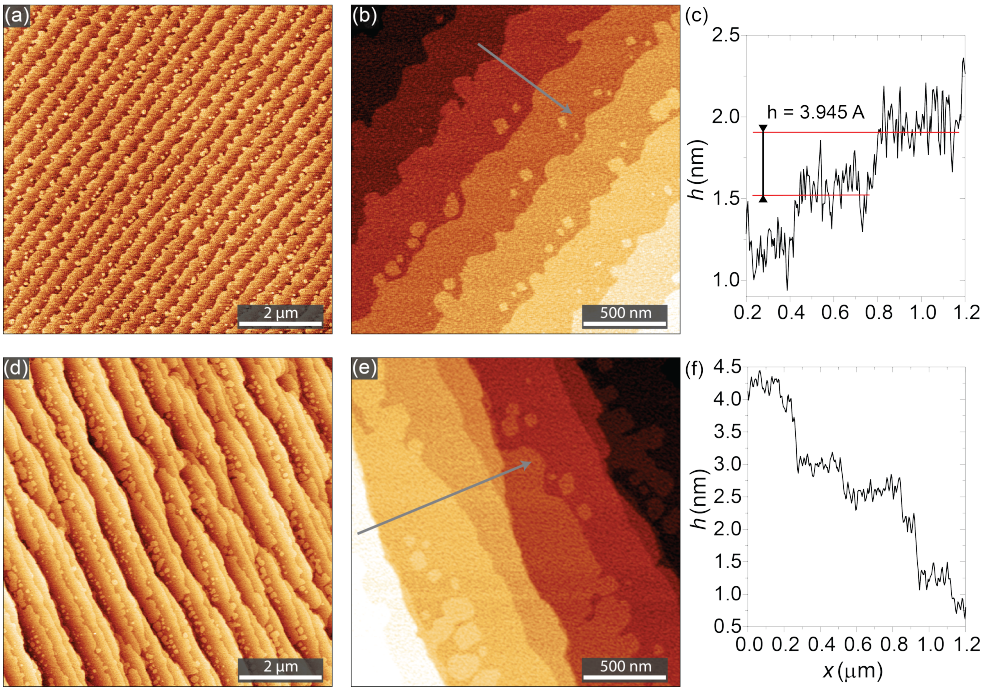

Figure 4.1: Different types of $SrRuO_3/SrTiO_3$ (100) film topographies measured by AFM. (a, b) Standard terrace structure (sample #153). (d, e) More complex terrace structure demonstrating step bunching morphology (sample #150). The thickness of both films is $\approx 12\,\text{nm}$. (c,f) Height profiles corresponding to the gray arrows on the images.

allows to collect are the surface topography and the phase contrast which carries information about variations in the film composition. Usually, a smooth film surface with well defined atomic steps is an indication of the stable layer-by-layer or step flow growth regimes which are desirable for good epitaxy.

AFM was performed using a commercial Cypher S microscope (Asylum Research, Oxford Instruments [166]) equipped with the ARC 2 controller. Scans were done by using AC imaging in air with AC160TS cantilevers (Olympus) with a resonant frequency of $\sim 300\,\text{kHz}$ and a spring constant of $\sim 42\,\text{N/m}$.

AFM was done as soon as possible after the extraction of the films from the UHV to avoid the contamination of the film surface by hydrocarbons in ambient environment [36,167]. Two typical examples of topographic AFM images measured for 12-nm-thick $SrRuO_3$ films grown on (100) $SrTiO_3$ are shown in Fig. 4.1. Figure 4.1(a,b) (sample #153) indicates a growth with a smooth surface and well-pronounced terraces with both the surface roughness and the step height of $\approx 3.945\,\text{Å}$ that corresponds to the out-of-plane lattice constant of $SrRuO_3$. The topography of the film shown in Fig. 4.1(c,d) (sample #150) is more complex.

Here, step bunching is observed which is an indication of unstable step flow growth [168, 169]. Despite the topography differences, both samples are characterized by indistinguishable transport and magnetic properties.

XRD

X-ray diffraction (XRD) is a powerful technique that allows to determine crystal lattice parameters of crystalline samples. XRD data have been measured in-house on the Empyrean set-up (Cu Kα line, $\lambda = 1.541$ Å) and at the Max Planck Institute beam line which is a part of the synchrotron radiation facility ANKA (Angströmquelle Karlsruhe, KIT, Germany, $\lambda = 1.239$ Å). Figure 4.2(a) shows a wide range $\theta/2\theta$ scan of a 10-nm-thick $SrRuO_3$ film grown on (100) $SrTiO_3$ (sample # 143) performed in-house. The first four $SrTiO_3$ peaks from the (h00) family are well visible. The peaks correspond to the diffraction maxima of $\lambda = 1.541$ Å on a cubic crystal with the lattice periodicity of 3.905 Å matching the lattice parameter of $SrTiO_3$. $SrRuO_3$ peaks are located close to the left from the corresponding $SrTiO_3$ ones. Figure 4.2(b) shows a close up view on the (004) $SrTiO_3$ and the corresponding (440) $SrRuO_3$ peaks measured at ANKA for a similar film (sample # 200). The $SrRuO_3$ peak is shifted by $\approx 0.9°$ towards smaller angles, which indicates a larger out-of-plane lattice parameter. That fits the out-of-plane lattice elongation caused by the Poisson effect and the bi-axial in-plane compressive strain applied to the film from the substrate. The peak broadening appears due to the small thickness of the film and well pronounced thickness fringes are visible. The thickness and the out-of-plane lattice parameter of the film can be extracted from the Laue intensity oscillations [170]:

$$I(Q) \sim \frac{sin^2(\frac{1}{2}NQc)}{sin^2(\frac{1}{2}Qc)} \tag{4.1}$$

where c is the out-of-plane lattice parameter, N is the film thickness, $Q = 4\pi sin\theta/\lambda$ is the reciprocal lattice vector. The fitting procedure yields $c = 3.943$ Å and $N \approx 10$ nm. The measured thickness oscillations decay faster as compared to the simulated Laue curve. This is due to the roughness of the film surface.

Figure 4.3(a) shows four reciprocal space maps (RSM) measured in-house for different φ angle orientations of the substrate for a 12-nm-thick $SrRuO_3$ film (sample # 121). The intense central maximum in the upper part of the maps corresponds to the ($\bar{1}03$) $SrTiO_3$ diffraction peak. Vertically elongated peaks below correspond to $SrRuO_3$. The peaks are shifted in Q_z indicating a larger out-of-plane lattice parameter. The in-plane lattice parameters along Q_x have the same value confirming that the film is fully epitaxially strained. Figure 4.3(b) shows the line-by-line averaged intensity profiles along the Q_z direction extracted from the RSM maps. It can be seen that the $SrRuO_3$ peak positions are shifted in

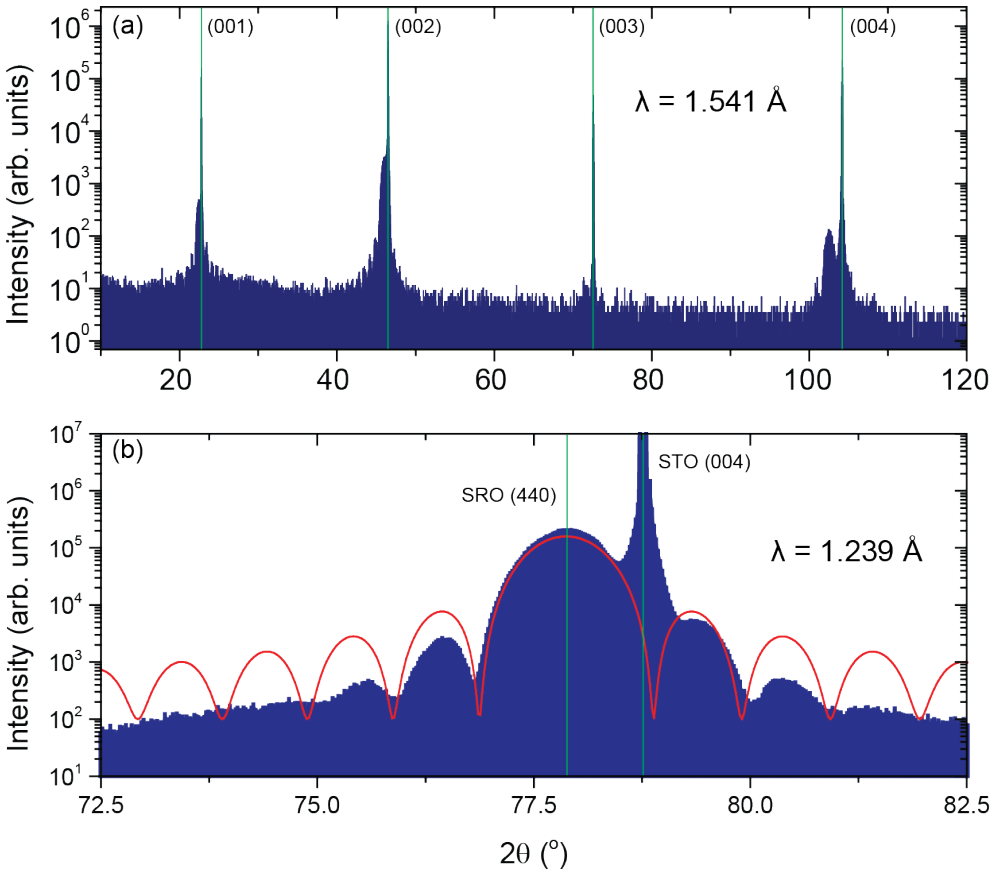

Figure 4.2: (a) Large scale $\theta/2\theta$ scan of a 10-nm-thick $SrRuO_3$ film grown on $SrTiO_3$ (100) performed in-house with the wavelength $\lambda = 1.541$ Å (sample #143), (b) $\theta/2\theta$ scan in the vicinity of the (004) $SrTiO_3$ peak performed at the ANKA synchrotron facility ($\lambda = 1.239$ Å, sample #200). Green lines mark peak positions and the red curve depicts the calculated Laue oscillations.

the Q_z direction by a small value which depends on the φ angle, indicating that the material has a distorted orthorhombic structure. The profiles show that the $SrRuO_3$ peak positions along $\varphi = 0°$ and $\varphi = 180°$ coincide, which implies that no orthorhombic distortion can be observed in these directions. The peaks at $\varphi = 90°$ and $\varphi = 270°$ are shifted relative to the central ones which allows us to determine the degree of the orthorhombicity. The distorted orthorhombic unit cell can be approximated as a tilted pseudocubic with the tilt angle $\alpha = arctan(\Delta Q_z/\Delta Q_x)$, where ΔQ_z and ΔQ_x are distances in reciprocal space along x and z between $SrRuO_3$ peaks for different φ angle orientations. The evaluation from the $\varphi = 90°$ and $\varphi = 270°$ peaks gives a tilt angle value of $\alpha = 0.49°$ which is in good agreement with the literature data [34, 171].

It is also important to mention that the XRD data do not reveal any evidence

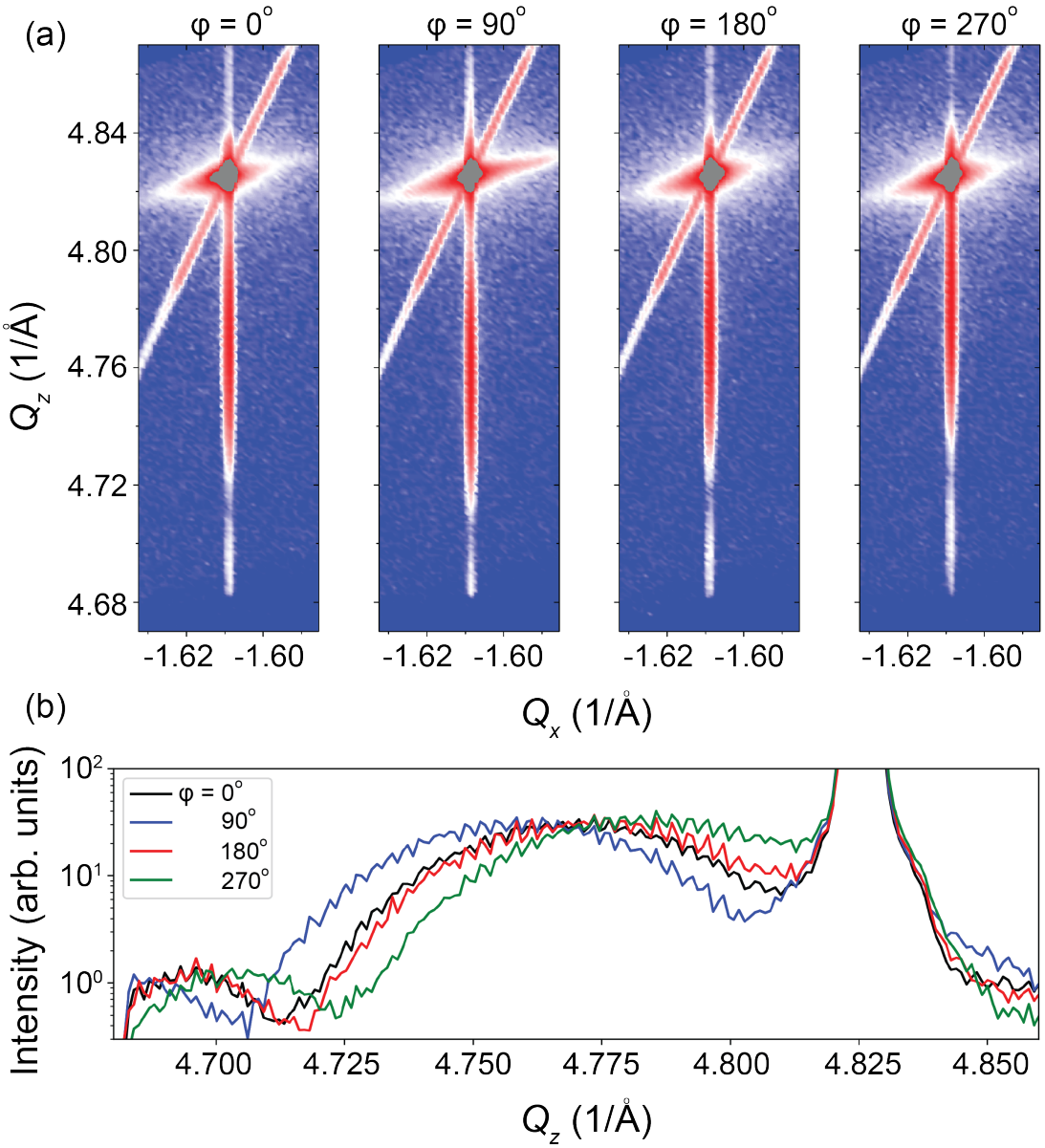

Figure 4.3: (a) Reciprocal space maps for a $SrRuO_3$ film grown on $SrTiO_3$ (100) measured around the $(\bar{1}03)$ peak of $SrTiO_3$ at four different φ angle orientations of the substrate (sample # 121), (b) line-by-line averaged intensity profiles along the Q_z direction for different φ angles.

of film twinning. We therefore consider the films to consist of single domains.

Electrical transport

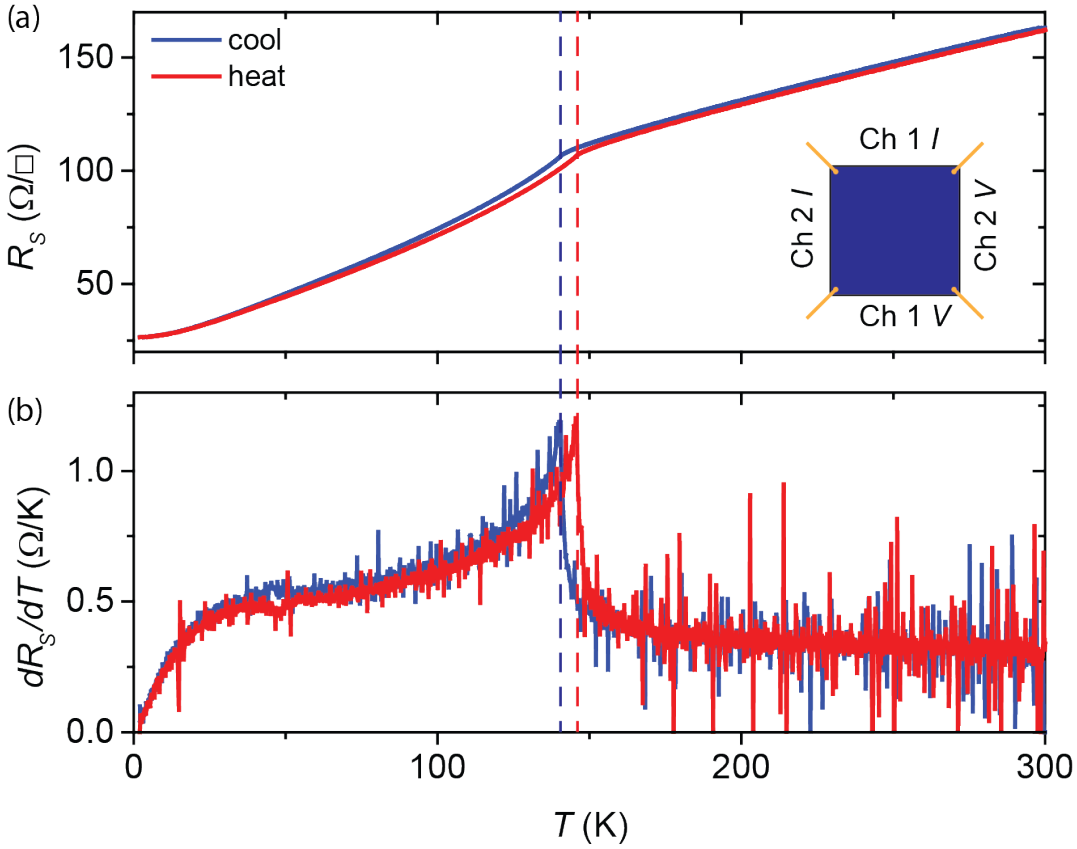

Figure 4.4: (a) Sheet resistance as a function of temperature for a 12-nm-thick $SrRuO_3$ film grown on $SrTiO_3$ (100) measured using the van der Pauw geometry shown in the inset (sample # 143). Measurements during cooling (blue) and heating (red) are performed at a rate of 1 K/min, (b) temperature derivatives of the same resistance curves showing the resistivity anomaly at T_C.

For conducting samples, electrical transport properties are important indicators of the film quality. The transport properties of the films were measured on a PPMS P9 system (Quantum Design) using the AC measurement mode. $SrRuO_3$ demonstrates metallic behavior in the entire temperature range [37, 172]. Figure 4.4 shows a typical measurement of the resistance as a function of temperature for a 12-nm-thick $SrRuO_3$ film grown on $SrTiO_3$ (100) using

van der Pauw geometry [173] with Au electrodes bonded to the corners of the $5 \times 5\,\mathrm{mm}^2$ film. The resistance was measured simultaneously in two channels corresponding to perpendicular directions (see the inset in Fig. 4.4(a)) and then the sheet resistance was calculated as the solution of the van der Pauw equation: $e^{-\pi\,(R_{\mathrm{vertical}}/R_{\mathrm{S}})} + e^{-\pi\,(R_{\mathrm{horizontal}}/R_{\mathrm{S}})} = 1$ [173]. The blue and red curves correspond to cooling and heating the sample with a rate of 1 K/min. The difference between them is related to the lag due to the heat capacity of the system during the continuous temperature sweep.

The Curie temperature T_{C} of the ferromagnetic transition is visible in the *R(T)* curves as a change of slope. Above T_{C}, the resistance changes linearly with temperature [37]. More precisely, T_{C} can be determined from the divergence of the temperature derivative of the sheet resistance curves as illustrated in Fig. 4.4(b) and marked with dashed lines. These peaks in the derivative are attributed to the short-range spin-spin correlations near T_{C} [174,175]. The actual T_{C} of the sample is calculated as the average between values for the cooling and heating lines. For the sample of Fig. 4.4 $T_{\mathrm{C}} = 143\,\mathrm{K}$. This is smaller than the extrapolated T_{C} determined from the SQUID magnetometry data (149 K, see Sec. 5.1.4). At temperatures below 15 K, the behavior of the resistance changes becoming close to quadratic $R = R_0 + aT^2$. This is due to the electron-electron and electron-magnon scattering. [176, 177]. Another important characteristic of the material that can be attributed to the amount of defects and impurities is the residual resistance ratio (RRR) equal to $R_{300\mathrm{K}}/R_{4\mathrm{K}} = 6.2$ which is a high value for PLD-grown $SrRuO_3$ films of comparable thickness [32]. The RRR for MBE-grown films is usually higher [178].

STEM

All STEM results have been collected in a collaboration with the Stuttgart Center for Electron Microscopy (StEM, [179]), especially with Hongguang Wang and Vesna Srot who were directly responsible for developing a technology for the TEM specimen preparation and measurements.

STEM images have been taken using a spherical aberration-corrected microscope (JEOL JEM-ARM 200F) with a DCOR probe corrector (CEOS GmbH) at 200 kV. Specimens in cross-sectional orientation were prepared by focused ion beam (Zeiss CrossBeam XB 1540) cutting, following by nanomilling at liquid nitrogen temperature (Fischione Model 1040 nanomill).

Figure 4.5 shows HAADF-STEM *Z*-contrast images of a cross-sectional cut of a $SrRuO_3$ film grown on (100) $SrTiO_3$. The single-crystal $SrTiO_3$ substrate is at the bottom of the images. Above it, the $SrRuO_3$ epitaxial film with the thickness of 8 nm (which corresponds to ≈ 20 unit cells of $SrRuO_3$) is located. *Z*-contrast images are sensitive to the mass of the constituent atoms. Ru atoms, having

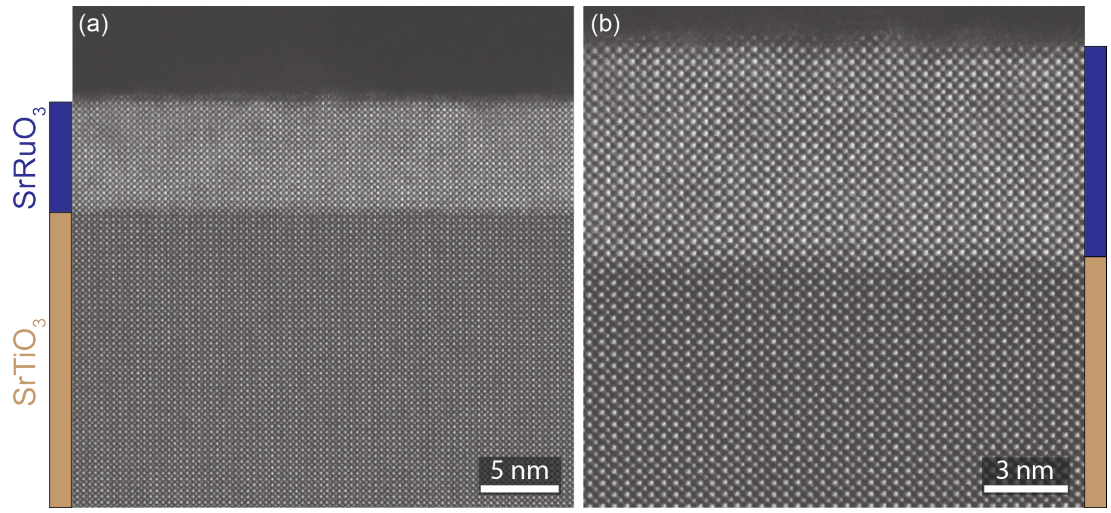

Figure 4.5: Z-contrast STEM images (cross-sectional cuts) of a $SrRuO_3$ film with a thickness of $\approx 8\,\text{nm}$ grown on (100) $SrTiO_3$ (sample # 093).

larger mass than Sr atoms, yield a larger contrast in the film. The interface area appears sharp and clean. Also, no significant defects are observed in the film.

4.1.2 $SrRuO_3/DyScO_3$ (110)

$DyScO_3$ is another suitable substrate for the $SrRuO_3$ growth due to the good lattice match. (110) $DyScO_3$ surface represents a square mesh with the in-plane lattice constant of $a_{DSO} = 3.944$Å [75, 79]. The tensile strain in epitaxial $SrRuO_3$ is therefore $S = (a_{SRO} - a_{DSO})/a_{SRO} = -0.35\%$ which is almost half of the compressive strain of $S = 0.64\%$ on (100) $SrTiO_3$. The growth window is, however, narrowed by the substrate surface termination conditions. In a wide range of growth parameters, pits tend to form close to the substrate steps. This happens due to imperfect substrate termination close to the atomic steps [28, 180]. Therefore, the growth parameters had to be re-optimized for $DyScO_3$ substrates to obtain a smooth film topography (see Sec 3.3.3). Examples of a film with pits and an optimized one are shown in Fig. 4.6.

Figure 4.7 shows a $\theta/2\theta$ scan of a 14-nm-thick $SrRuO_3$ film grown on (110) $DyScO_3$ performed in-house. According to the data, the film is compressively strained despite a smaller lattice parameter of bulk $SrRuO_3$ compared to $DyScO_3$ [181]. This indicates that $SrRuO_3$ grown at such growth parameters is off-stoichiometric which results in a larger lattice constant of the material. The fitting procedure according to Eq. 4.1 yields $c = 3.963$Å and $N \approx 14\,\text{nm}$.

Magnetometry measurements of $SrRuO_3$ grown on $DyScO_3$ are complicated. The paramagnetic substrate with the saturation magnetization up to $M_s \approx$

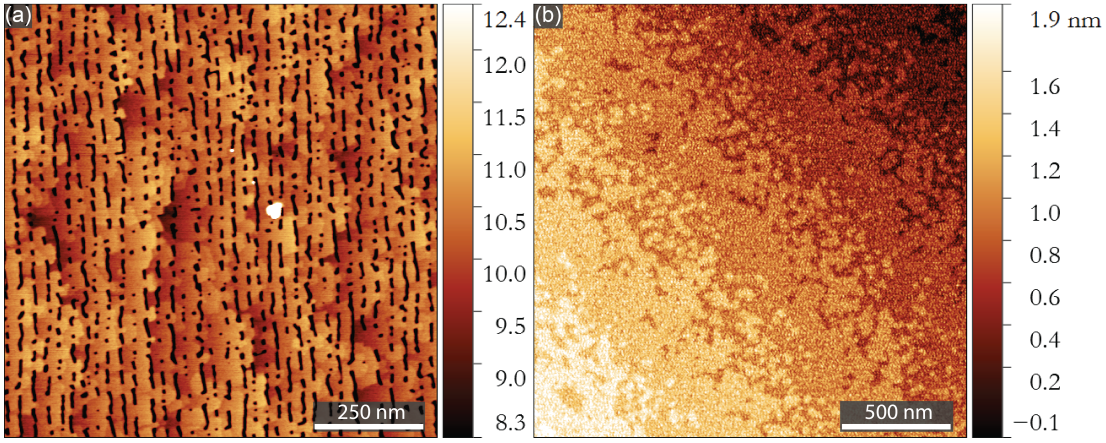

Figure 4.6: (a) A 12-nm-thick thin film of $SrRuO_3$ grown on $DyScO_3$ (110) demonstrating ordered pit stripes forming close to pre-existing substrate steps (sample # 164). (b) A similar film grown at optimized conditions (sample # 205).

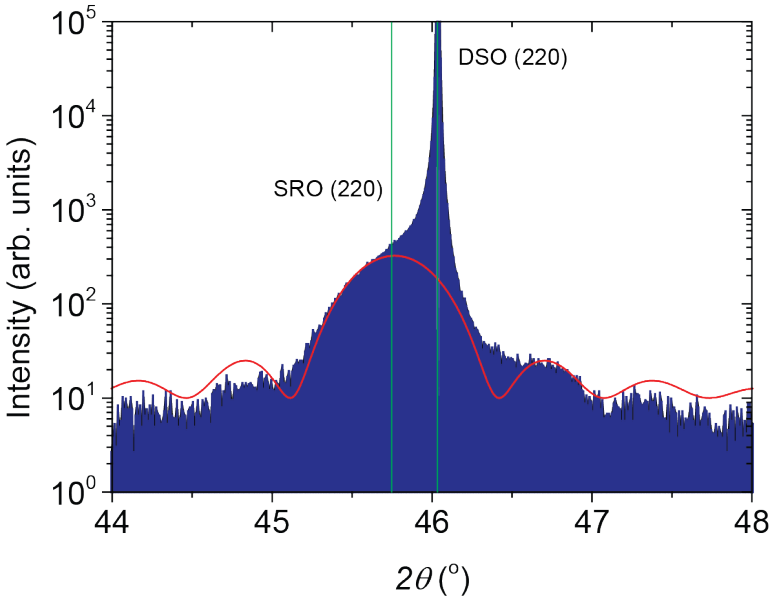

Figure 4.7: $\theta/2\theta$ scan of a 14-nm-thick $SrRuO_3$ film grown on (110) $DyScO_3$ in the vicinity of the (220) $DyScO_3$ peak performed in-house (sample # 210). Green lines mark peak positions and the red curve depicts the calculated Laue oscillations.

$8\,\mu_B$/Dy introduces a very strong background signal that masks the ferromagnetism of the film. As well as on $SrTiO_3$, $SrRuO_3$ on $DyScO_3$ is metallic and was used in this work for the fabrication of nanostructures for the investigation of electrical transport properties. These properties are described in Chapter 6 which is devoted to the $SrRuO_3$ nanolines.

4.2 Nanodots of $SrRuO_3$

Nanodots have been fabricated from the $SrRuO_3$ thin films using the patterning technology described in Sec. 3.4. For reasons explained in Sec. 3.4.1, for most samples, squares are used as the designed shape of the dots. The shape of the resulting dots depends on the feature size, because all shapes get rounded once the size of the structure approaches the resolution limit of the e-beam lithography. Figure 4.8 shows several top-view SEM images of dots with different sizes. The deviation from the rectangular shape becomes noticeable already for sizes below 200 nm.

The total number of dots on a sample is given by the structure size and dots spacing. For most samples, the designed distance between centers of two adjacent dots is equal to two dot diameters. The real dot spacing to dot size ratio, however, increases as the dots become smaller. This effect arises from the contraction of the structure size under the influence of the ion etching which becomes more relevant at small sizes. So, after etching through an Al_2O_3 mask containing dots of 40 nm size, the diameter of the resulting dots equals only about 20 nm. The dot spacing in this case is limited to about 80 nm, increasing the spacing-to-size ratio to four.

The number of dots in an array increases with decreasing dot diameter. For example, with decreasing the dot size from 200 to 20 nm, the number of dots on a substrate rises by an order of magnitude from 10^8 to 10^9. Due to inhomogeneities during patterning, i.e., resist thickness variations and substrate charging, defects such as missing or distorted dots, may appear in the resulting structure. The probability of such effects increases with decreasing dot size and spacing but normally does not exceed several percent of the total number of dots. Examples of such defects may be seen in Fig. 4.8(e) as missing dots. The figure shows an AFM topography image of several rectangular arrays of 20-nm-size dots separated by small gaps. The height of the dots is just $\approx$ 2-3 nm which allows to create sufficient contrast to reveal the atomic terraces of the underlying $SrTiO_3$ substrate.

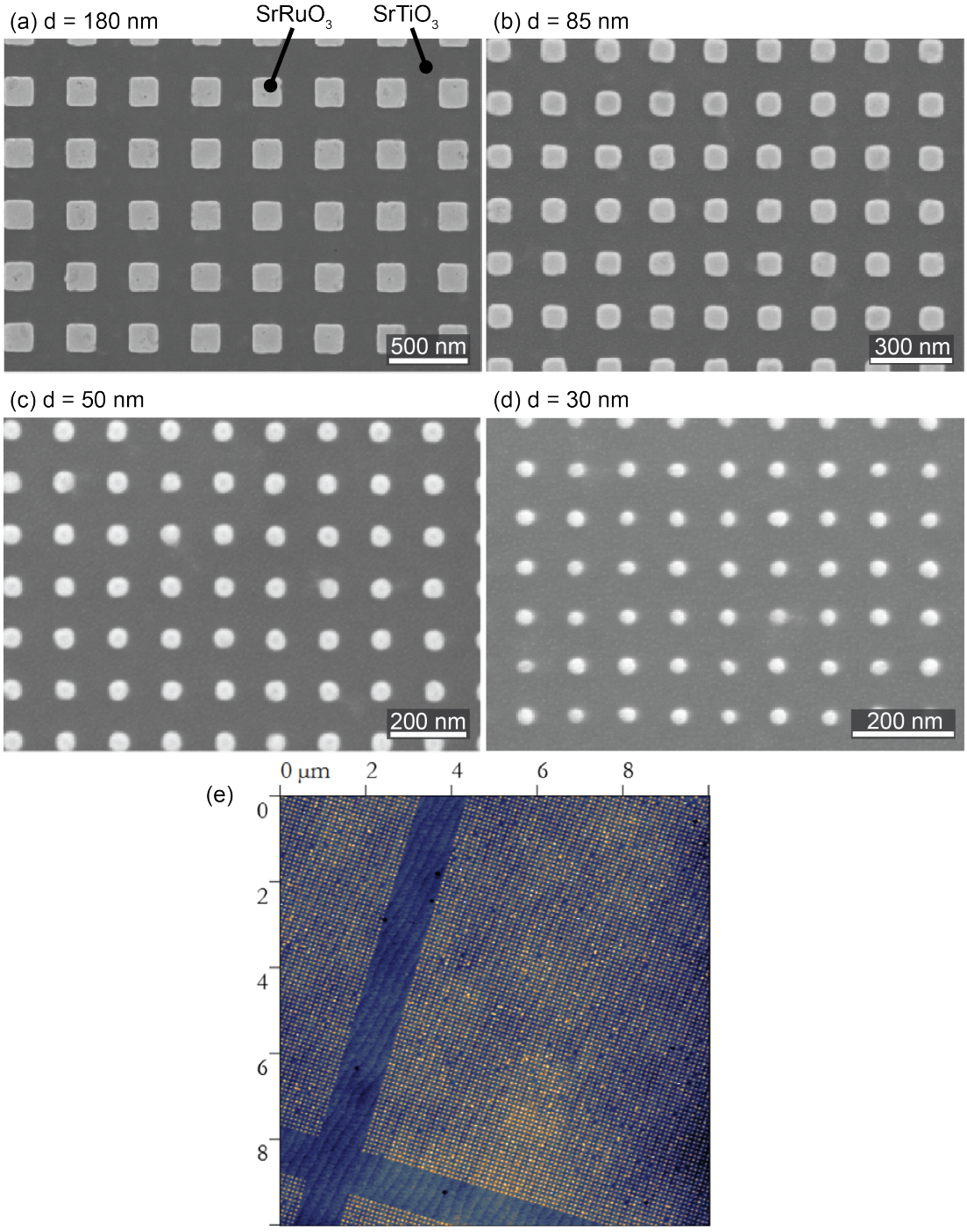

Figure 4.8: Top-view SEM images of rectangular arrays of $SrRuO_3/SrTiO_3$ dots with diameters of (a) 180 nm, (b) 85 nm, (c) 50 nm, (d) 30 nm and heights of 12 nm (sample # 133). It is seen how the dot shape transforms from rectangular to circular with reducing dot size, although all dots are rectangular by design. (e) AFM image of several arrays of 20-nm-size dots demonstrating contrast between the dots and the underlying terraces of a substrate (sample # 52). The height of the dots is $\approx$ 2-3 nm.

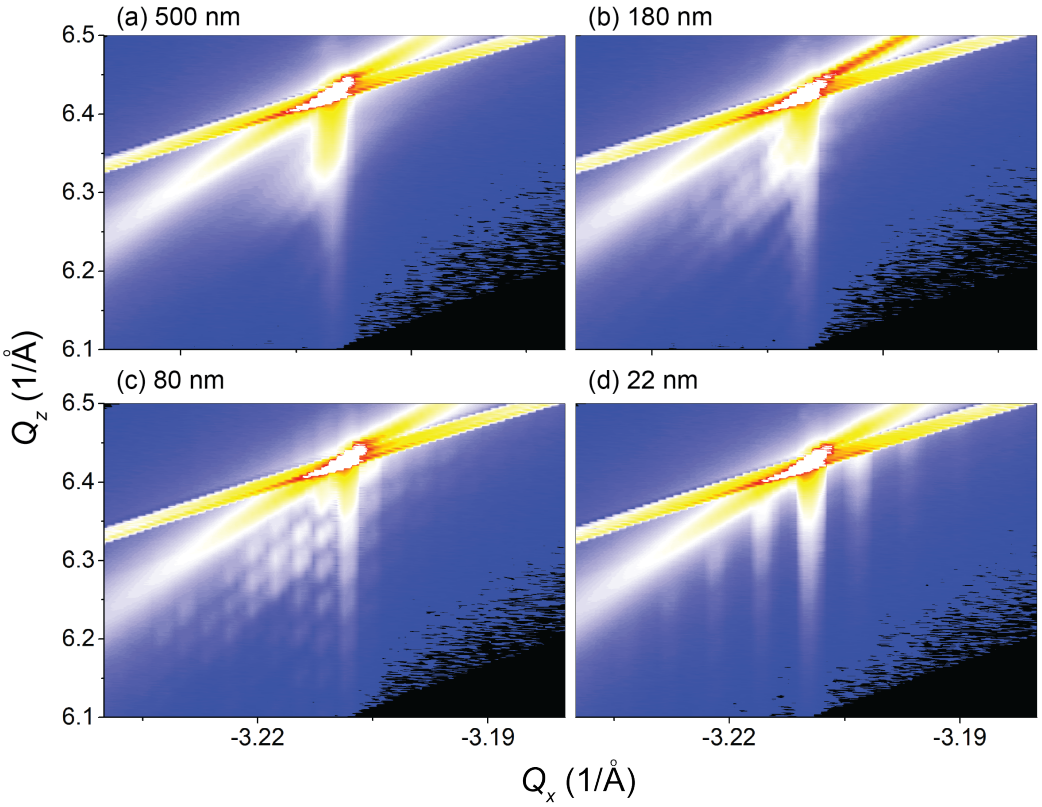

Figure 4.9: Reciprocal space maps measured in the vicinity of the (204) peak of $SrTiO_3$ on a sample with rectangular arrays of $SrRuO_3$ dots of different sizes (sample # 198). The diffraction on the large scale structure of the arrays corresponding to different dot periodicities can be observed.

4.2.1 XRD

X-ray diffraction measurements on nanodot arrays were performed at the ANKA synchrotron facility (Karlsruhe, Germany) using a wavelength of $\lambda = 1.239$ Å. For these measurements, several rectangular arrays of nanodots of different sizes (from 500 nm to 22 nm) have been fabricated on a single substrate. Figure 4.9 shows reciprocal space maps measured on dots with different diameters in the vicinity of the (204) $SrTiO_3$ diffraction maximum. Just as for films, RSMs for dots show an elongated $SrRuO_3$ peak located under the $SrTiO_3$ one. Also, depending on the array periodicity, additional diffraction peaks appear on the sides of the main one. The peaks originate from x-ray diffraction on the large scale structure of the arrays. The distance between the peaks in reciprocal space increases with decreasing real space array periodicity. This distance gives the correct value of the dot spacing in the arrays. The appearance of additional maxima has the downside that the intensity of the radiation gets distributed between all subpeaks,

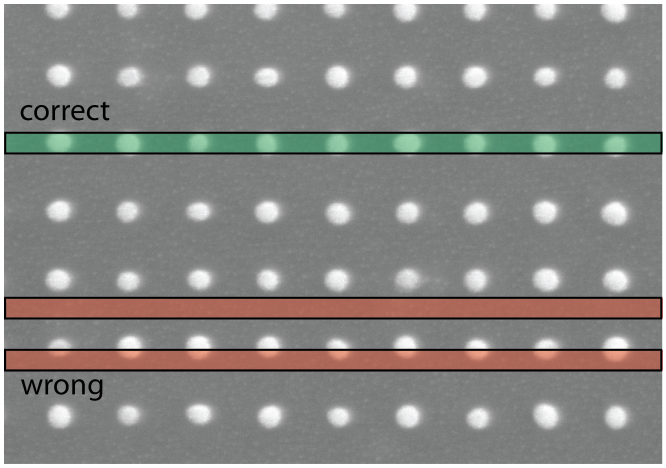

Figure 4.10: For the high-quality images of dots cross sections, TEM lamellae have to be cut as close to the center of dots as possible (green). Otherwise (red), either none or only a small amount of the dot material is included in the cut.

thereby reducing the counting statistics of the measurement which is already low due to the small amount of $SrRuO_3$ in the arrays. Such a low counting statistics does not allow to make solid conclusions about the material structure.

4.2.2 STEM

The TEM sample preparation for ordered arrays of nanodots is technologically complicated. The challenge is mainly related to the rather small density of dots on a sample. In order to obtain high-quality images of the dot structures, a TEM lamella has to be prepared in a way that a row of dots is cut as close to the dot centers as possible. In practice, using the standard procedure of sample cutting, most cuts are done either in the space between dots or dots are only partially included in the lamella. The illustration of this is shown in Fig. 4.10. A typical thickness of a lamella specimen for TEM to provide high resolution imaging is $\approx 20\,\text{nm}$. Such a thickness is comparable with the size of the small nanodots. For dots with a diameter of 20 nm, the distance between dot centers is limited by about 80 nm due to limitations of the technological process. This makes the probability of a central cut with the standard "blind" method, used for large scale structures, rather small. To overcome this, a specimen preparation technology using focused ion beam cutting and nanomilling was developed in the StEM department. This allows the precise adjustment of the cut relative to the dots.

Figure 4.11 depicts several STEM images which give an overview of the dot appearance with several nanodots cut in a row (Figure 4.11(a)), a single 80-nm-diameter nanodot (Fig. 4.11(b)) and a single 30-nm-diameter nanodot with the magnified interface region showing atomic resolution (Fig. 4.11(c,d)). The images demonstrate that after patterning the material remains epitaxial with a clean interface without visible defects, indicating that no significant structural

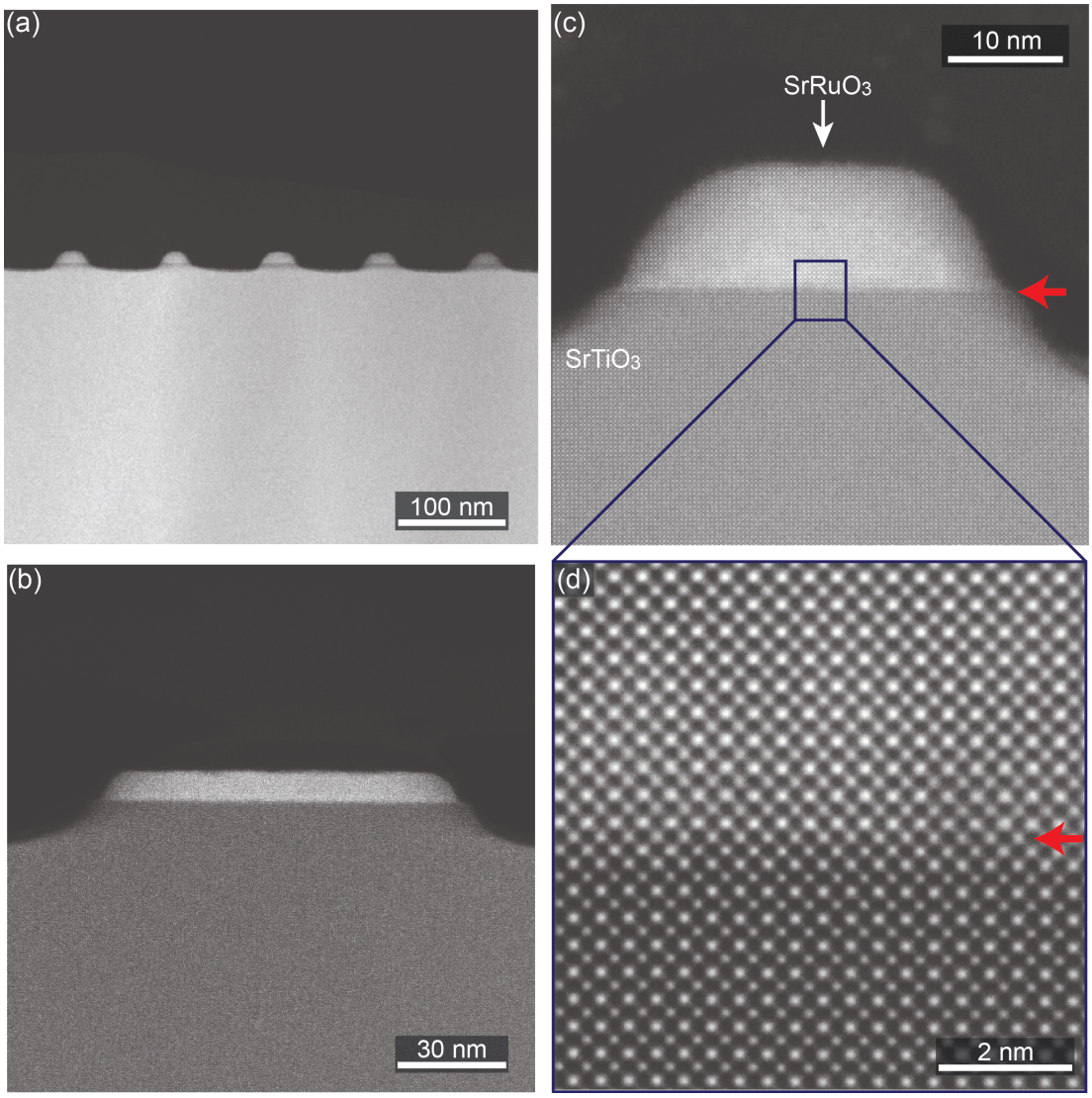

Figure 4.11: STEM images of cross-sections for various $SrRuO_3$ nanodots. (a) Several dots of $\approx 30\,\text{nm}$ diameter cut in a row (sample # 119), (b) a single nanodot with 80 nm diameter (sample # 169) (c) a single nanodot with 30 nm diameter (sample # 176), (d) magnified atomic resolution image of the same dot.

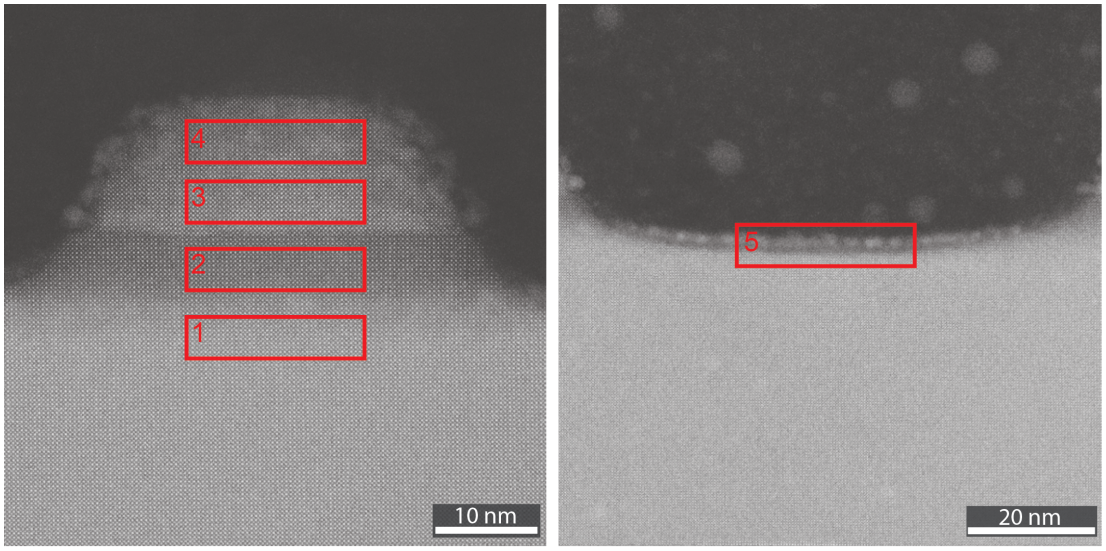

Element	1	2	3	4	5
Sr	50.0 ± 3.3	47.8 ± 3.9	41.0 ± 3.6	39.3 ± 5.0	43.5 ± 4.1
Ti	49.5 ± 1.2	51.2 ± 1.1	3.1 ± 0.4	3.4 ± 0.6	50.0 ± 1.6
Ru	0.5 ± 0.3	1.0 ± 0.5	55.9 ± 1.8	57.3 ± 2.8	6.5 ± 0.8

Figure 4.12: EDX analysis of the elemental distribution in different parts of a nanodot. The table provides quantitative results for the regions marked with boxes. (1) the region of bulk $SrTiO_3$ substrate, (2) $SrTiO_3$ pillar remaining after the dry etching, (3) bottom and (4) upper part of the $SrRuO_3$ nanodot, (5) a region between nanodots at the substrate surface.

changes have occurred to the material during patterning. Dry etching with Ar ions removes the material non-uniformly, causing the curved shape of the dots. This effect is also responsible for the lateral size reduction of the structure.

Energy-dispersive X-ray Spectroscopy (EDX) was performed at different regions of the dot cross sections and the substrate space in between dots using the TEM microscope. Figure 4.12 shows the results as the distribution of elements (Sr, Ti and Ru) in the bulk substrate (region 1), the $SrTiO_3$ pillar (region 2), the bottom (region 3) and upper (region 4) parts of the nanodot and at the surface of the substrate in the region between dots (region 5). The elemental composition of the region 1 corresponds to the stoichiometric $SrTiO_3$ with a very small amount of Ru that presumably comes from the surface. In the region of the $SrTiO_3$ pillar, the concentration of Sr is reduced by $\approx 2\%$. This small difference is, however, within the error margin of the measurement. In the $SrRuO_3$ part, the composition is slightly off stoichiometry, favoring Ru over Sr. The difference becomes larger in the upper part of the dot which was subjected for a longer

time to the ion flux. This suggests that Sr during the ion milling process is more volatile. Also, small amounts of Sr and Ru can be observed in all regions due to the re-deposition of materials during etching. In the spacing between dots, the surface layer of ≈3-5 nm can be visually distinguished from the rest of the substrate, here the material is apparently damaged by the ion irradiation.

4.2.3 Single-unit-cell-thick $SrRuO_3$ nanodots

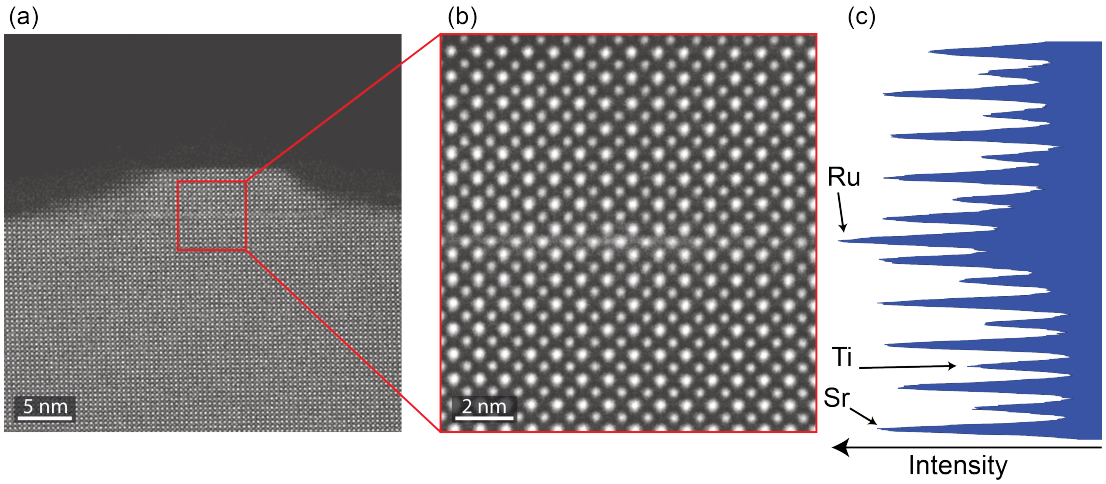

Figure 4.13: (a) STEM image of the cross section of a single-unit-cell-thick $SrRuO_3$ patterned into a nanodot with a diameter of 30 nm. (b) Magnified STEM image showing the $SrRuO_3$ layer with the measured electron beam intensity profile (c).

The precise film thickness control of pulsed laser deposition together with the well-optimized layer-by-layer growth regime of $SrRuO_3$ on $SrTiO_3$ allow us to fabricate stable layers of $SrRuO_3$ with thicknesses as small as a single unit cell. Such a layer can also be patterned into nanodots. An example of the appearance of such nanodots is depicted on STEM images in Fig. 4.13. Here, the $SrRuO_3$ monolayer is sandwiched between two layers of $SrTiO_3$ and patterned laterally to dots with a diameter of ≈ 30 nm. The intensity profile in Fig. 4.13(c) reveals the sharp interface with a single Ru oxide layer. The walls of these dots have a larger slope compared to pure $SrRuO_3$ nanodots due to the much smaller etching rate of $SrTiO_3$ during Ar milling.

Unfortunately, the extremely small amount of $SrRuO_3$ in such samples does not allow for meaningful magnetometry measurements.

Chapter 5

Nanodots of $SrRuO_3$

This chapter describes the main experimental results of this thesis. Mostly, the results are related to the modification of magnetic and structural properties of $SrRuO_3$ after patterning the material from thin films to nanodots. To illustrate this modification in a comprehensive manner, we provide a comparison of the magnetic properties between the films and the nanodots and discuss the origin of their discrepancies. For this reason, the description of the magnetic properties of the thin films is also given in this chapter rather than in the previous one.

We also analyze, by means of TEM, structural changes to the material which are partially responsible for the modification of its magnetic properties.

5.1 Measurement techniques

For the measurement of the magnetic properties two techniques have been mainly used. The primary technique was SQUID (superconducting quantum interference device) magnetometry [182], as it provides an extremely high sensitivity which is necessary to measure the very small amount of magnetic $SrRuO_3$ present in the nanodot samples. The second technique - VSM (vibrating sample magnetometry) [183] - has been used as a secondary one. It provides by an order of magnitude smaller sensitivity and, therefore, can only be used for the measurement of the thin films. The advantage of it is the higher data acquisition rate which makes it useful for the express analysis of the samples. In the section below, a brief description of the techniques, measurement parameters, sample mounting and the analysis used to extract the data from raw signals are given.

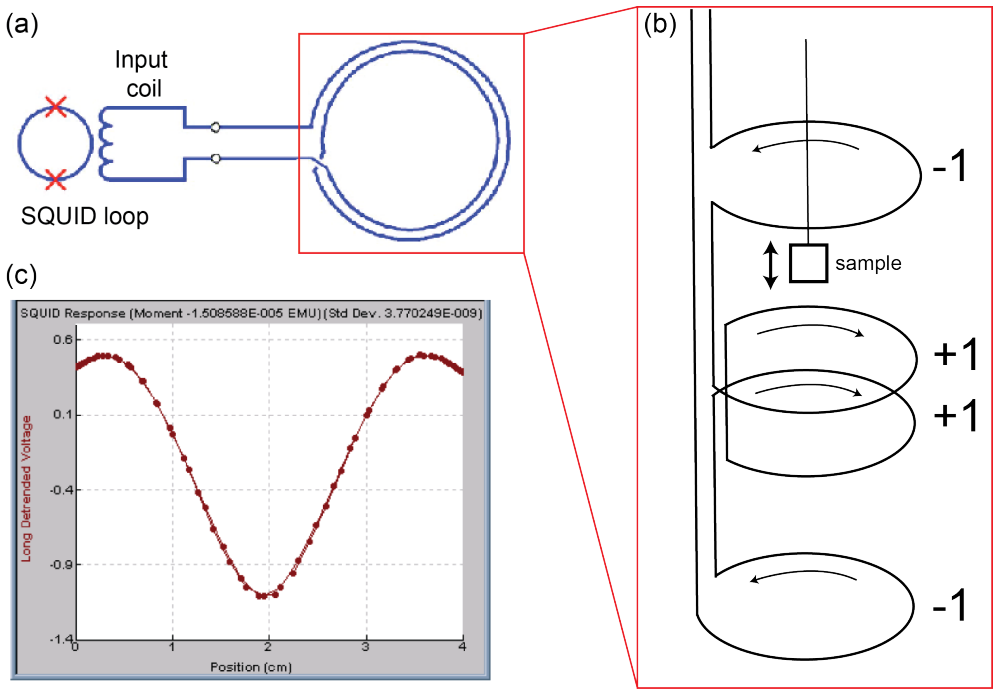

Figure 5.1: Schematic of a SQUID magnetometer. (a) A SQUID loop inductively coupled to a flux transformer, (b) a pick-up coil of the flux transformer in the form of a second derivative gradiometer. The sample oscillates relative to the coil producing an inductive signal with a typical form as shown in (c). Adapted from [182, 189, 190].

5.1.1 SQUID magnetometry

The SQUID magnetometry is available in several generations of MPMS (Magnetic Properties Measurement System, Quantum Design, USA [184]) setups, all of which have a similar functionality.

The name "SQUID" by itself is not directly related to magnetometry. A SQUID device represents a superconducting loop with one or two Josephson junctions that finds application in a large number of setups and technologies [182]. The most common one is, indeed, the measurement of small magnetic fields. But besides this, SQUIDs are used for NMR [185, 186], in biomedicine [187] or even to test some predictions of general relativity [188].

The principle of measuring magnetic fields using a SQUID is based on the Josephson effect and the quantization of the magnetic flux in a superconducting coil [191]. When the magnetic flux through a SQUID coil changes, it causes a variation of the critical current of the Josephson junction. Measuring this variation allows to determine the value of the external magnetic field with high precision. The variation of the magnetic flux in a range of just a half of the flux quantum produces a measurable amount of the voltage drop across the SQUID

that grants the device its extreme sensitivity. The sensitivity, however, has a downside as it also makes a SQUID magnetometer extremely sensitive to any variations of the external electromagnetic background. For example, a typical sample produces in the SQUID a magnetic response of the order of one thousandth of a flux quantum, whereas the Earth's magnetic field flux through a $1\,\mathrm{cm}^2$ area is equivalent to about a million flux quanta [189]. Therefore, SQUIDs have to be very well shielded from any external influence and extremely precise electronics and feedback loops are required. SQUIDs are not used to measure magnetic fields directly. Instead, external magnetic fluxes are coupled to a SQUID device by means of flux transformers (see Fig. 5.1(a)) [192]. Another reason to use the flux transformers is that the sensitivity of a SQUID loop decreases with increasing size. Hence, the loop has to remain small enough and can not be used for a direct measurement of macroscopic samples. In order to minimize the sensitivity of the magnetometer to distant magnetic field sources, the detection coils of the flux transformer that interact directly with the sample consist of several loops wound in opposite senses. The MPMS systems use the so-called second derivative gradiometer scheme (see Fig. 5.1(b)) [190] that helps to cancel any uniform magnetic fields originating from outside the magnetometer.

All measurements for this work have been performed using the reciprocating sample option (RSO) with the sample rapidly oscillating relative to the detection coils. This produces the inductive response with a typical form shown in Fig. 5.1(c) which is then fit by the theoretically expected curve to determine the actual magnetization of the sample. Such a method achieves a higher sensitivity than the alternative dc measurement scheme. The most frequently used measurement parameters were: 4 cm of oscillation amplitude with a frequency of 0.5-1 Hz and 10 oscillation cycles per data point. The typical sensitivity of such a measurement is of the order of 10^{-12}-$10^{-11}\,\mathrm{Am}^2$ (10^{-9}-10^{-8} emu) depending on the experimental conditions.

The MPMS setups allow to apply magnetic fields up to 7 T and a temperature range of 1.7-400 K. The maximum sample size is $5 \times 5\,\mathrm{mm}^2$.

5.1.2 Processing a SQUID response

A SQUID measurement does not provide a direct value of the sample magnetization. Instead, the voltage of the inductive response is measured and then the magnetization is calculated using a fit of the voltage curve (see Fig. 5.1(c)). By default, this procedure is done by the operating software and does not require the involvement of a user. This gives acceptable results when measuring samples with a magnetization well above the sensitivity limit. If the sample magnetic moment is weak or the magnetic system is complex, the shape of the response

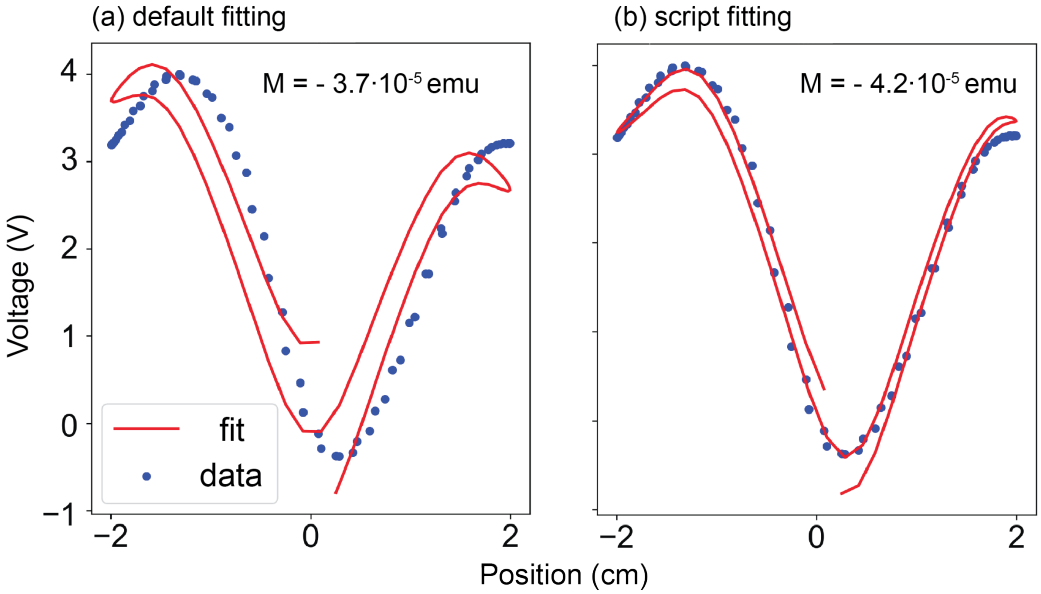

Figure 5.2: Fitting of the same SQUID response curve performed (a) by the SQUID software, (b) using my own Python script. The values of the magnetization extracted from the two fits differ by more than 10 %.

can significantly deviate from a perfectly symmetric one. This is related to competing magnetic signals or various drifts happening during a measurement, e.g., an electronic drift or a sample displacement. For such signals, the default fitting routine does not do its job well. The value of the magnetization extracted from such imprecise fitting can be noticeably different from the actual sample magnetic moment. In order to overcome this issue, a Python script has been written to analyze the raw data manually. Figure 5.2 shows an example of the fitting performed by the SQUID software (Fig. 5.2(a)) and the fitting done using the script (Fig. 5.2(b)). In the example, the response voltage curve is asymmetric and slightly off center which causes a deviation of the fit curve. A much better coincidence of the fit with the measured response can be achieved through the manual fitting procedure.

The script fits the following equation to the measured inductive response in the SQUID flux transformer [193]:

$$\begin{aligned} f(Z) = X_1 + X_2 \cdot Z + X_3 \cdot \{2 \cdot [R^2 + (Z + X_4)^2]^{-3/2} - \\ -[R^2 + (\Lambda + (Z + X_4))^2]^{-3/2} - [R^2 + (-\Lambda + (Z + X_4))^2]^{-3/2}\} \end{aligned} \tag{5.1}$$

where Z is the sample position, R and Λ are the setup defined longitudinal radius and the longitudinal coil separation constants, respectively. The fit parameter X_1 is a constant offset voltage, X_2 takes into account a linear electronic drift during the measurement, X_3 is an amplitude and X_4 is a shift of the sample along the axis

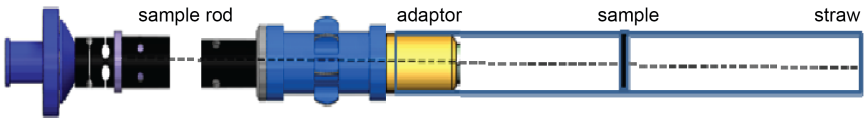

Figure 5.3: Mounting of a sample for magnetometry using a plastic straw. The out-of-plane orientation is shown. Adapted from [194].

of the magnet. The actual magnetization of the sample can then be determined from the parameter X_3 using the following equation:

$$M = \frac{X_3 \times long\_regr\_factor \times RSO\_regr\_factor}{SQUID\_cal\_factor \times sensitivity\_factor \times correction\_factor} \quad (5.2)$$

with additional factors defined by the setup parameters and the gain settings during measurement. More details about the script and the fitting procedure can be found in Appendix B.

5.1.3 Vibrating Sample Magnetometry

Vibrating sample magnetometry is similar to the RSO SQUID with the difference that instead of an ultrasensitive SQUID device, a relatively simple pick-up coil is used. A sample moves sinusoidally relative to the pick-up coil and the induced voltage is measured. The sample movement is controlled by a precise linear motor. Such an approach achieves a sensitivity that is about two orders of magnitude smaller than that of a SQUID, namely 10^{-10}-10^{-9} Am^2 (10^{-7}-10^{-6} emu). The advantage of the technique is its speed which makes it useful for a rough express analysis of samples that do not require high sensitivity, i.e., thin films. The VSM used in this work is an extension of the PPMS (Physical Property Measurement System) setup and can utilize its capabilities of 9 T magnetic field and 1.7-400 K temperature range. Apart from the sensitivity difference, the results obtained in this thesis by VSM are in full agreement with the SQUID results.

5.1.4 Measurement procedure

The measurement procedures used were essentially the same for the SQUID and the VSM. A sample was mounted into a transparent non-magnetic plastic straw supplied by Quantum Design (see Fig. 5.3) [194]. Since during the measurement straws are oscillating with the frequency of 1-10 Hz, it is necessary to fix the samples well to avoid shifting. Samples can be measured in the out-of-plane and in-plane oriented magnetic field (see Fig. 5.8). In the out-of-plane orientation, the sample plane is positioned perpendicular to the straw axis and the stability is secured by edges of the straw which is partially cut. For the in-plane measurements, the samples were additionally placed into plastic capsules which were

then fixed inside the straws. To protect the sample surface when in contact with the sharp edges of the straw, a protective layer of PMMA resist was spin coated on top of the substrate. It was checked that this resist layer does not alter the magnetic properties of the system, apart from a small diamagnetic contribution.

During the sample fabrication, it is desirable to avoid contacts with magnetic metals such as iron. Even a micrometer size particle of iron attached to a sample can produce a magnetic signal larger than that of $SrRuO_3$ dots. This is especially important for invasive procedures, i.e., sample cutting with wire saw.

Important characteristics of ferromagnetic materials can be obtained through two types of measurements. The first one is the magnetization versus temperature, $M(T)$. It allows to observe how the ferromagnetic transition occurs and to measure its Curie temperature, T_C. $M(T)$ is usually divided into two parts - zero-field-cooled (zfc) and field-cooled (fc). First, a sample is cooled to low temperature in the absence of the external magnetic field. In this case, ideally, magnetic moments remain randomly oriented across the ferromagnetic transition and the net magnetization remains zero. In a real experiment, however, a small residual magnetic field remains in the superconducting magnet that may magnetize a sample to a small extent. Then, a small magnetic field (usually $\sim 0.1\,\mathrm{T}$) is applied and the sample is heated, providing the zfc curve. Once the sample temperature exceeds the ferromagnetic transition, it is cooled again in the same magnetic field, yielding the fc curve. During this measurement, as soon as T_C is reached upon cooling, the magnetic moments orient themselves in the external magnetic field, thereby producing a net magnetization which increases with decreasing temperature as thermal fluctuations play a smaller role.

T_C determination. In real ferromagnets, especially in thin films, the ferromagnetic transition is smoothened due to various reasons [195] such as thermal fluctuations, temperature gradients or material inhomogeneities. As a consequence, ferromagnetic transition curves have tails with a finite magnetization above T_C. Because of this, the question of a precise determination of T_C is relevant. There is no agreement in the literature on the subject. One common way is to use the magnetic susceptibility measurements [196, 197]. For conventional ferromagnets, the plot of inverse magnetic susceptibility versus temperature is a linear curve which can be easily extrapolated to zero. MPMS SQUIDs, however, do not allow to measure the susceptibility directly and VSM, as discussed above, is not sensitive enough for nanodot samples. Therefore, another way has to be found. Different approaches are used to directly determine T_C from the $M(T)$ curve. This can be done either by a linear extrapolation of the $M(T)$ curve to $M = 0$ (so-called extrapolated T_C) [198], by finding the point of maximum curvature on the transition curve [199, 200], by fitting the entire $M(T)$ curve, e.g., the two-tangent method [195], by using Arrott plots [201], and others [202, 203].

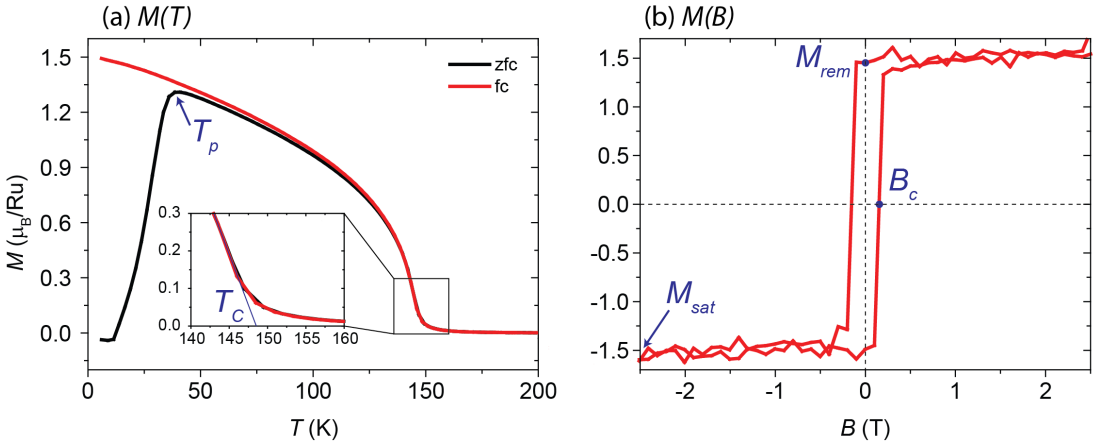

Figure 5.4: Characteristic parameters of ferromagnetic materials shown by using the example of a $SrRuO_3$ thin film. (a) $M(T)$ curve with the denoted extrapolated Curie temperature T_C and magnetic peak temperature T_p. (b) Hysteresis $M(B)$ loop with the denoted saturation magnetization M_{sat}, remnant magnetization M_{rem} and coercive field B_c.

Different methods give slightly or even significantly different values of the transition temperature. For materials such as $SrRuO_3$, T_C can also be determined from the resistance anomaly which exists in $R(T)$ curves at the ordering temperature (see Sec. 4.1.1). For our study, the precise value of T_C is not as important as its relative variation across samples. For our purpose, it is therefore sufficient to stick to a certain method which gives reproducible results. In this research, T_C is determined by the linear extrapolation method (see Fig. 5.4). Other methods were found to be more complicated due to the unconventional character of the transition curves in nanostructured samples.

Hysteresis loops. Important information about ferromagnets can be extracted from their hysteretic properties, i.e., the dependence of the magnetization on the history of the system. Ferromagnetic materials are able to maintain a magnetization in the absence of an external field that grants them such properties as the remnant magnetization M_{rem} which is preserved at $B = 0$ and the coercive field B_c at which the magnetization projection changes its sign (Fig. 5.4(b)). These values and the overall shape of the hysteresis loop can give important information about the magnetic anisotropy, domain structure, etc.

A measurement of a hysteresis loop starts at the magnetic field $+B$ above the magnetic saturation. After that, the field is swept to $-B$ and back to $+B$ again, measuring a closed loop. When sweeping the magnetic field, the measured magnetic moment is the projection of the magnetization vector to the magnetic field axis. In the absence of the magnetic field, the magnetization orients along

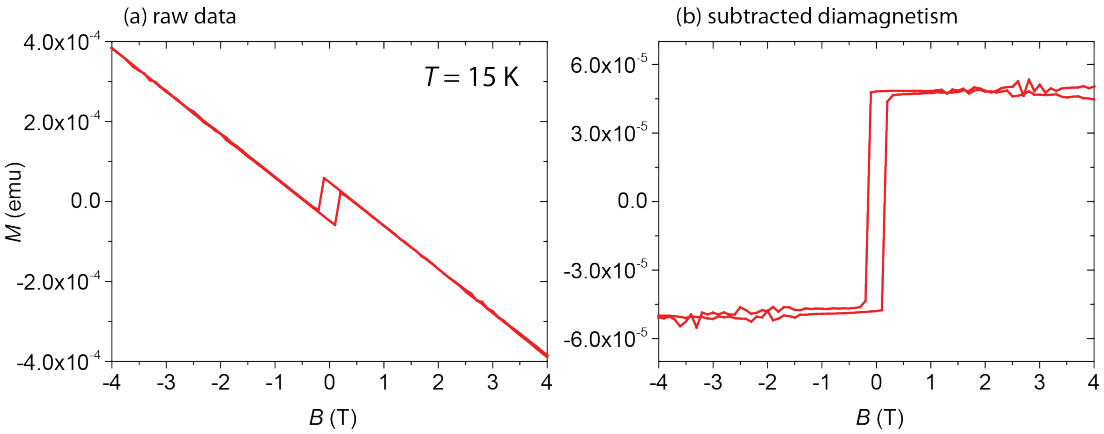

Figure 5.5: SQUID magnetometry $M(B)$ measurement at $T = 15\,\mathrm{K}$ in an out-of-plane oriented magnetic field on a thin film of $SrRuO_3$ with a thickness of 12 nm showing an example of subtraction of the diamagnetic contribution from the $SrTiO_3$ substrate. (a) raw data, (b) subtracted data (sample #211).

the crystallographically defined magnetic easy axis of the material. If the angle between the easy axis and the measurement axis is small, the remnant magnetization tends to be close to the saturation and vice versa. An increase of the magnetic field leads to the rotation of the magnetization from the easy axis to the magnetic field axis, towards saturation. This creates "tails" of the hysteresis loops (see, e.g., Fig. 5.8(b)). If the magnetic easy axis coincides with the direction of the magnetic field, a hysteresis loop has a "rectangular" shape as the magnetization vector just flips between positive and negative projections of the magnetic field.

All known substances exhibit magnetic properties, at least at the level of diamagnetism. This means that in an external magnetic field they develop a small magnetization oriented opposite to the field. Even though the effect of the diamagnetism is usually rather small, it becomes important when measuring thin films grown on substrates. Normally, substrates have a volume which is by many orders of magnitude larger than that of a thin film. This makes even small diamagnetic contributions from the substrate relevant. Luckily, at achievable magnetic fields, diamagnetism is linear with the field and nearly temperature independent [204]. For the hysteresis measurements, the diamagnetic contribution of the $SrTiO_3$ substrate should be subtracted from the raw data (see Fig.5.5):

$$M_{SRO} = M_{tot} - \chi H \tag{5.3}$$

where M_{SRO} is the desired $SrRuO_3$ magnetization, M_{tot} is the total magnetization measured, χ is the negative diamagnetic susceptibility of $SrTiO_3$ and H is the magnetic field strength. The exact value of χ as required for precise measurements

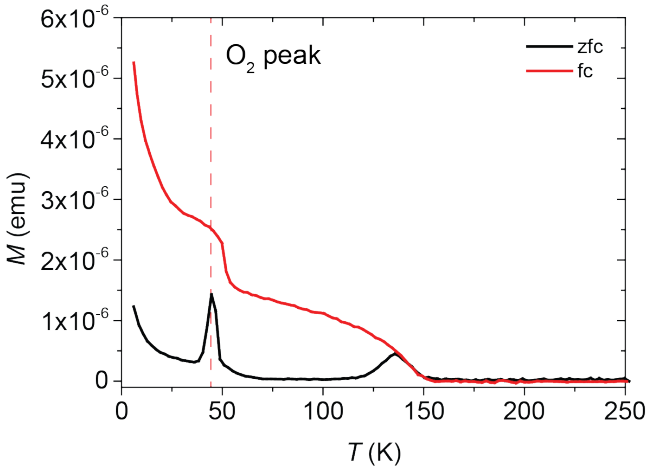

Figure 5.6: An example of a SQUID measured $M(T)$ curve for a nanodot sample (#122) with oxygen contamination in the chamber. Peak at $T = 44\,\mathrm{K}$ caused by the oxygen is visible.

depends also on the sample mounting technique, the substrate orientation and the chamber background and has to be determined experimentally. On average, a value of $\chi = -(7.2 \pm 0.3) \cdot 10^{-6}$ in dimensionless SI units is found, which is comparable to the literature values of the diamagnetic susceptibility for $SrTiO_3$ crystals [205, 206]. Figure 5.5 shows an example of how $M(B)$ curves look before and after the subtraction of the $SrTiO_3$ diamagnetic contribution. For $M(T)$ curves only a constant contribution has to be subtracted as they are measured at fixed magnetic field.

One of the biggest problems for low-temperature magnetometry is oxygen. Since it is present everywhere around us, it is also not difficult to find some amount of it in a measurement chamber. And sometimes it is a non-trivial task to purge the chamber entirely oxygen free or to prevent oxygen leakages during the measurement. The reason oxygen is so unwanted is that it undergoes a series of magnetic phase transitions at low temperatures [207, 208]. It is paramagnetic in its liquid state and solidifies at $T \approx 54\,\mathrm{K}$ into the paramagnetic γ-phase. With reducing the temperature further, at $T \approx 44\,\mathrm{K}$ and $T \approx 24\,\mathrm{K}$ it transforms to the β and α-phases, respectively, both of which are antifferomagnetic. During these phase transitions, the magnetic susceptibility of oxygen changes drastically which introduces large disturbances in the measurements, if oxygen is present in the vicinity of the sample. For macroscopic samples it does not cause much trouble as it is usually not difficult to keep the oxygen concentration low enough. But it becomes a problem when measuring thin films or, even more, nanostructures. An example of such an oxygen-contaminated measurement performed on a sample with 25-nm-size dots is shown in Fig. 5.6 (sample #122). As can be seen, there is a clear disturbance in the signal close to $T \approx 50\,\mathrm{K}$ which is a characteristic sign of the oxygen contamination [209]. To avoid its appearance, the measurement chamber needs to be purged well and leakages have to be prevented.

5.2 Magnetic properties of $SrRuO_3$ thin films

As was already mentioned in Sec. 1.3.1, the magnetic properties of $SrRuO_3$ are very sensitive to almost any kind of disorder in the material, including stoichiometry, strain and defects. For this reason, the properties of PLD-grown films are usually worse than those of MBE ones as PLD does not allow to precisely control the material stoichiometry and the high-energy flux of ions and ultraviolet radiation from the plasma plume may produce additional defects in a substrate [210, 211]. Nevertheless, a careful optimization of the deposition conditions allows to grow films with rather high magnetic and structural quality.

Together with other parameters, the magnetic properties of the material can be used as indicators of its quality. Key magnetic criteria that characterize $SrRuO_3$ are: the Curie temperature of the ferromagnetic transition T_C, the saturation magnetization M_s, the coercive field B_c, and the peak temperature of the zero-field-cooled magnetization T_p. For the following results, the magnetization is normalized to the expected number of Ru atoms on a substrate and presented in μ_B/Ru units.

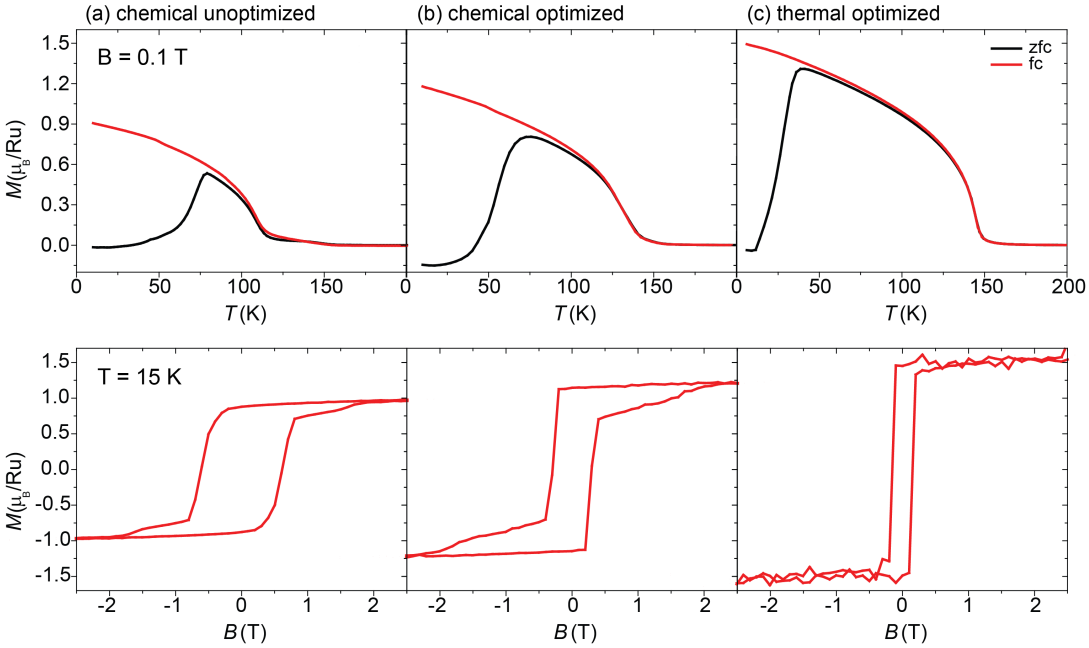

Figure 5.7: SQUID magnetometry measurements of $M(T)$ characteristics (top) and hysteresis loops (bottom) of $SrRuO_3$ thin films of comparable thickness grown on (100) $SrTiO_3$ at different growth conditions: (a) a film grown on a chemically terminated substrate before the growth optimization, (b) after the growth optimization, (c) on an *in situ* thermally annealed substrate. All measurements were performed in an out-of-plane oriented magnetic field.

The PLD deposition parameters were optimized in two steps. An overview of the deposition process and parameters for all optimization steps can be found in Sec. 3.3.3. For the fabrication of first samples, $SrTiO_3$ substrates were terminated using etching with buffered HF acid, followed by a long-time annealing in an oven at ambient oxygen pressure (see Sec 3.2). The first optimization step was done here, when the "old" parameters used for the growth of $SrRuO_3$ by previous generations of growers were re-optimized to improve the magnetic properties. This step corresponds to the transition from (a) to (b) in Fig. 5.7 which shows $M(T)$ and hysteresis curves for the two optimization steps. Later, when the technology of *in situ* thermal annealing was developed and applied, it helped, together with an additional optimization, to further improve the magnetic properties. The final magnetic parameters of the films are depicted in Fig. 5.7(c). All curves in the figure are measured using the out-of-plane orientation of the substrate with 0.1 T applied field for the $M(T)$ curves and $T = 15\,\mathrm{K}$ for the hysteresis loops. The films produced with the "old" growth parameters (Fig. 5.7(a)), had rather poor magnetic properties - the Curie temperature showed a large spread and low values of $T_C \approx 120 - 140\,\mathrm{K}$ with an unconventional double-step magnetic transition, a small saturation magnetization $M_s = 0.8 - 1.0\,\mu_\mathrm{B}/\mathrm{Ru}$, and a high coercivity $B_c \approx 0.7\,\mathrm{T}$. After the first optimization, the magnetic characteristics improved significantly, providing $T_C \approx 141 \pm 4\,\mathrm{K}$, higher $M_s = 1.0 - 1.2\,\mu_\mathrm{B}/\mathrm{Ru}$, and smaller $B_c \approx 0.5\,\mathrm{T}$. Still, there was a large spread of properties presumably originating from the different quality of the substrate surface after the chemical treatment. The implementation of *in situ* annealing brought the magnetism to a new level, with $T_C = 149 \pm 1\,\mathrm{K}$, $M_s \approx 1.3 - 1.5\,\mu_\mathrm{B}/\mathrm{Ru}$ and $B_c \approx 0.2 - 0.3\,\mathrm{T}$. At this point, the material quality can be compared to the best $SrRuO_3$ films published [32]. Together with this, the stability of the properties between different films has increased significantly, strongly reducing the spread. The remaining spread of the saturation magnetization originates, evidently, from the imprecise determination of the film thickness or magnetic dead layers at the film surface or at the interface with the substrate. Also, it can be seen that that the magnetic peak temperature T_p, which is defined as the maximum of the zero-field-cooled magnetization, decreases throughout the optimization. Its value changes from 78 K to 73 K and even 39 K for the consecutive optimization steps, respectively. This peak originates from the interplay between the thermal energy and mainly the energy of domain wall displacement [212]. Such a behavior takes place only if the value of the applied magnetic field does not exceed a critical value. At higher fields, the difference between the zfc and fc branches of the $M(T)$ curves vanishes and the material is completely magnetized even at low temperatures. The decrease of T_p can be related to the modification of the magnetic domain structure or the weakening of domain wall pinning. A small deviation observed

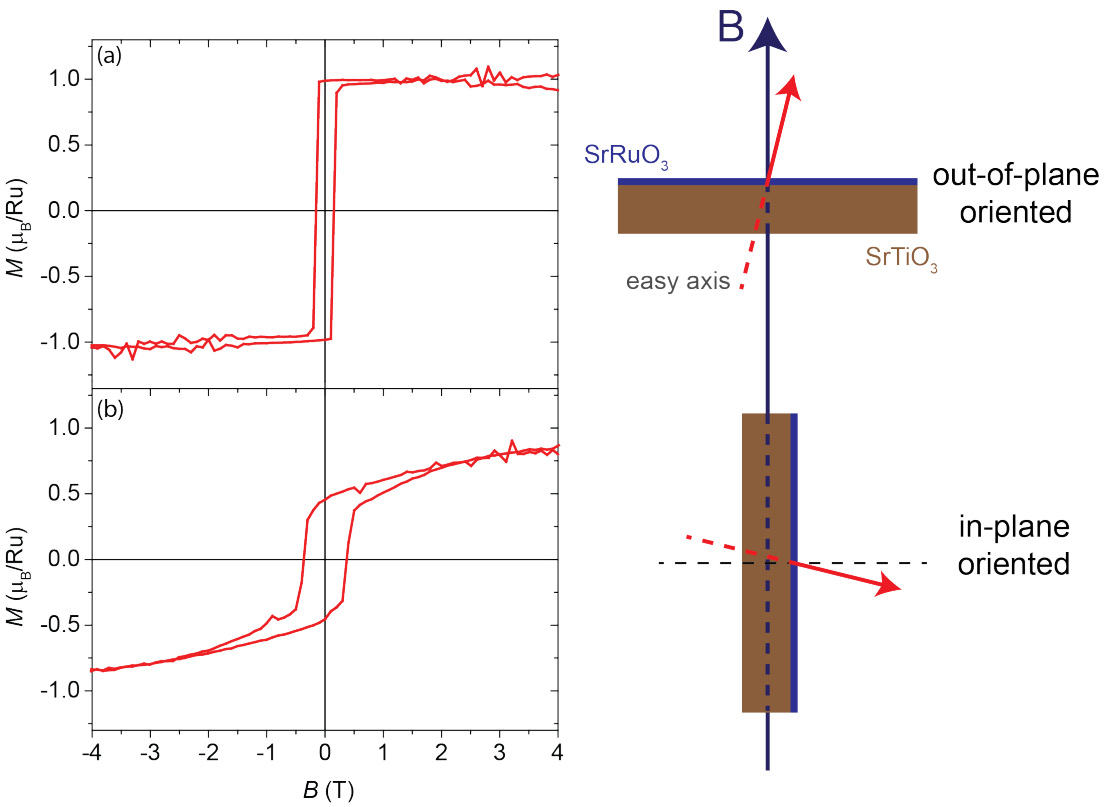

Figure 5.8: Hysteresis loops of a 12-nm-thick $SrRuO_3$ film grown on (100) $SrTiO_3$ measured at $T = 15\,K$ in the (a) out-of-plane and (b) in-plane oriented magnetic field (sample #211). Schematic in the right panel illustrates the different orientation of the magnetic easy axis which causes the difference in the hysteretic behavior.

for several zero-field-cooled curves from zero at low temperature is related to the residual magnetic field of the superconducting magnet of the MPMS setup. The constriction of the hysteresis loops is yet an another manifestation of the magnetic properties improvement. The existence of well-defined "tails" in hysteresis loops in Fig. 5.7(a,b) indicates that at this growth conditions the structure of the magnetic domains of $SrRuO_3$ or the domains pinning is different which influences the magnetization reversal.

All data presented in Fig. 5.7 are measured in an out-of-plane oriented magnetic field. In the in-plane orientation, the key parameters of the $M(T)$ curves remain the same with a slight change of the shape. Hysteresis loops, however, change significantly due to the magnetic anisotropy of $SrRuO_3$. An example of magnetic hysteresis loops measured for a 12-nm-thick $SrRuO_3$ film at 15 K in the out-of-plane and in-plane orientations is shown in Fig. 5.8 (sample # 211). The behavior is different for the two orientations. As described in Sec. 1.3.1,

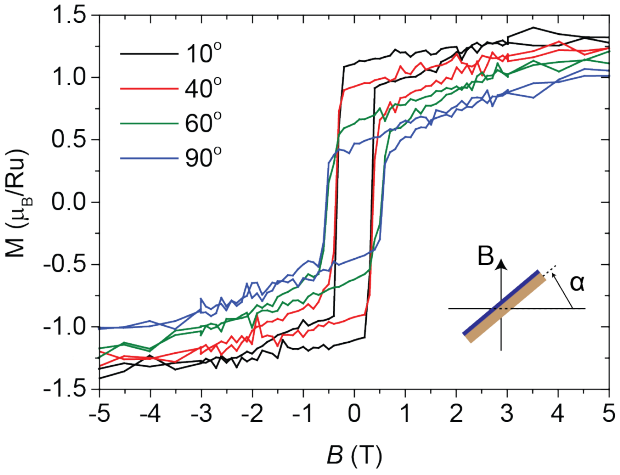

Figure 5.9: $M(B)$ measurements of a 12-nm-thick $SrRuO_3$ film grown on (100) $SrTiO_3$ performed at several substrate orientations and $T = 15\,K$ demonstrating how the hysteresis loops change when the magnetic easy axis rotates relative to the magnetic field (sample #96). For this experiment, a chemically treated substrate was used.

the magnetic easy axis for $SrRuO_3$ grown on (100) $SrTiO_3$ is tilted relative to the film normal under a temperature-dependent angle of 30-45°. With decreasing temperature, the easy axis rotates towards the film normal. For our samples, the orientation of the easy axis was found to differ slightly between different films, depending on the film thickness and the growth conditions. Also, the orientation of the substrate in a SQUID chamber may affect the result as the angle can not be precisely controlled. In general, however, in the out-of-plane orientation, hysteresis loops always have a more rectangular shape, i.e., with M_{rem} close to M_{sat} and the saturation happening at low magnetic field. This implies that the easy axis is close to the film normal. In the in-plane orientation, M_{rem} is approximately half the M_{sat} indicating that the magnetic field is aligned approximately with the magnetic hard axis. At the same time, the value of the coercive field B_c in the in-plane orientation is usually higher.

Additional data demonstrating the angular dependence of the hysteresis loops is shown in Fig. 5.9. Here, $M(B)$ curves were measured for four different orientations of the substrate. It can be seen how the loops change in shape as the direction of the magnetic easy axis deviates further from the magnetic field axis. From the images we can also conclude that the easy axis is oriented relatively close to the film normal. Unfortunately, the construction of the magnetometer does not allow a precise control of the substrate angle. The angle measurement error is $\approx 10°$. This experiment was performed with the film grown on a chemically treated substrate. The shape of the hysteresis loops is therefore different from the ones presented in Fig. 5.8.

Film properties are not only a matter of deposition conditions. As was explained in Sec. 1.3.1, the properties of $SrRuO_3$ are sensitive to minor modifications of the material stoichiometry. For PLD-grown samples, the material stoichiometry is defined, first of all, by the composition of the target, as the

ablation process provides a close-to-stoichiometric transfer of the material from target to substrate. It was found, that when a series of samples was grown without polishing a target, the magnetic properties were slowly deteriorating from the first sample to the last one. For example, for a series of samples from #73 to #77 grown without polishing the target, T_C of the thin films was gradually decreasing from $\approx 136\,\mathrm{K}$ to $\approx 117\,\mathrm{K}$. This series was produced before the final growth optimization. Such a deterioration may be related to the change of the target stoichiometry during the long ablation (with presumably getting more Ru deficient as it is the most volatile component) or to the the increase of the amount of particulates transferred to the substrate [213]. However, no such particulates were observed under AFM. In order to maintain the quality of material properties at high level, the target was polished every time before a new deposition session. During a single session, two films were usually grown.

5.3 Substrate modification after patterning

Properties of samples change in many respects after patterning. First of all, $SrRuO_3$ itself is modified, its amount on the substrate is greatly reduced and the material is transformed from the thin film to nanostructured form. Together with this, the substrate, $SrTiO_3$, subjected to the ion irradiation, acquires conductivity and enhanced magnetism. Therefore, when measuring the patterned samples, it is important to separate effects originating in the substrate from the ones in the nanodots. To understand the modifications happening to the substrates, two experiments were performed. First, bare $SrTiO_3$ substrates were subjected to the same fabrication steps that were used for nanodot samples but without the $SrRuO_3$ growth and e-beam lithography, i.e., only the substrate termination and ion etching were done. Second, $SrRuO_3$ was grown but during the Ar milling the etching time was increased significantly to etch away the entire $SrRuO_3$ layer from the substrate. Samples were then measured by SQUID magnetometry as usually. In both cases, the results were similar.

As was mentioned in Sec. 1.3.2, an ideal $SrTiO_3$ crystal does not possess magnetic properties other than diamagnetism. However, in real $SrTiO_3$, vacancies and possibly clusters of vacancies are present [214]. These vacancies may serve as a source of magnetic moments and grant the material paramagnetic or ferromagnetic properties. Additionally, after the crystal is subjected to processing, i.e., by ion [215] or light [216] irradiation, the magnetism may be enhanced. The exact mechanism of the magnetic signal appearance is still under debate [70, 217, 218]. Practically, in our work only paramagnetism has been observed. Normally, when measuring $SrRuO_3$ thin films, the size of this effect is very small compared to the film signal and can be neglected. After the patterning, two things happen.

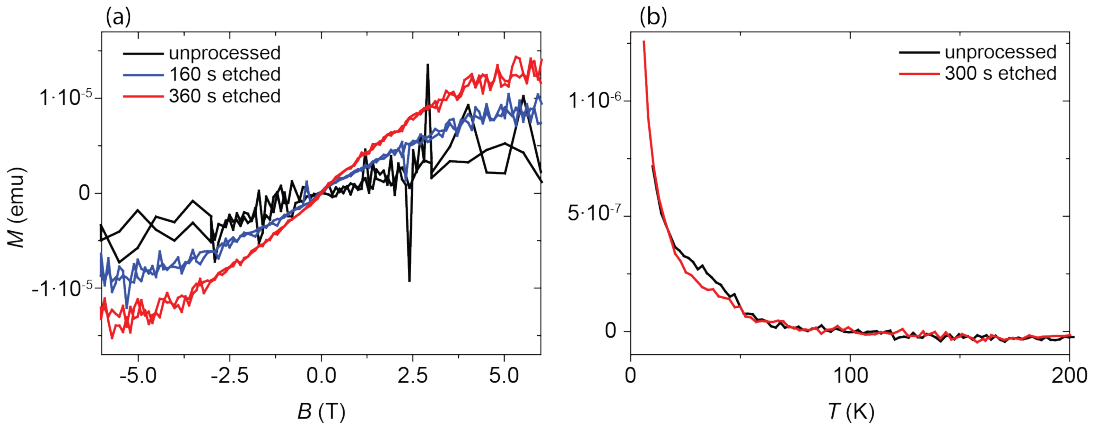

Figure 5.10: SQUID magnetometry measurement on bare $SrTiO_3$ substrates before and after the ion irradiation. (a) $M(B)$ curves measured at 15 K for a substrate etched for 160 and 360 s (sample #097), (b) $M(T)$ curves measured at 0.1 T for a substrate before and after 300 s etching (sample #125). All curves show a paramagnetic signal.

First of all, the amount of $SrRuO_3$ on the substrate is substantially reduced (only 5-10% of the film material remains). Second, during Ar milling, the amount of vacancies in the substrate is facilitated. These changes both make the substrate contribution to the signal much more relevant. Figure 5.10 shows an example of $M(B)$ and $M(T)$ curves for (100) $SrTiO_3$ substrates before and after the irradiation with Ar ions. In both cases, a small paramagnetic signal of the order of $10^{-9} - 10^{-8}\,\mathrm{Am}^2$ ($10^{-6} - 10^{-5}$ emu) can be observed at low temperature. This is approximately one order of magnitude smaller than the ferromagnetic signal coming from a $SrRuO_3$ film and it is comparable to the one observed in nanodots. The contributions, according to the Curie-Weiss law, becomes more relevant with decreasing temperature and are non-negligible only at temperatures below 50 K. This is far below the ferromagnetic transition temperature of $SrRuO_3$ (149 K) which is the interest of this work. The small paramagnetic signal inherent to $SrTiO_3$ becomes stronger after the Ar milling due to the formation of additional vacancies (Fig. 5.10). The $M(B)$ curves show no coercivity, depend linearly on the magnetic field in the range of $B = \pm(2 - 2.5)\,\mathrm{T}$ and start saturating at a field of $B \approx 5\,\mathrm{T}$. On the other hand, $M(T)$ measured at a small magnetic field of 0.1 T do not show much difference before and after the irradiation. The numbers, however, are not reproducible for different substrates as there is a variation in the intrinsic level of paramagnetism across substrates. Also, the Ar milling itself has a spread of parameters (see Sec. 3.4.3) which further influences the reproducibility.

5.4 Magnetic properties of nanodots

For this work, nanodots have been fabricated with a wide range of sizes, ranging from 100 μm to 15 nm in diameter. Over this range of almost four orders of magnitude, the magnetic properties change substantially. The magnetism in large dots ($> \sim 10\,\mu$m) resembles the one of thin films. Varying the size of the dots from large to small, one can trace the evolution of properties from thin-film-like to nanodot-like. In this section, different aspects of the dot magnetic properties are described and their comparison with the properties of the unstructured films are provided.

For a detailed description of dot properties other than magnetic see Sec. 4.2. Mostly, dots have been prepared in rectangular arrays with the distance between dots varying from one to three dot diameters. For larger dot spacing, the total amount of $SrRuO_3$ becomes too small to be measured.

When growing $SrRuO_3$, the material is deposited not only on the top surface of a substrate but also on its edges. The additional magnetic signal from the side walls is relevant and may even be comparable to the one from small nanodots. To get rid of this material, prior to measurement the edges of the samples were gently polished using a piece of fine SiC sand paper and then cleaned according to the standard cleaning procedure (Sec. 3.2).

Down to the smallest measured dot sizes (≈ 15 nm), $SrRuO_3$ remains ferromagnetic. This means that there are no significant dead layers and damage to the material appearing as a result of patterning that makes the material lose its functional properties. This in turn opens up many possibilities for fabrication and study of such complex functional oxide nanostructures.

5.4.1 $M(T)$ curves

Figure 5.11(b) shows an $M(T)$ curve for $SrRuO_3$ nanodots with a diameter of ≈ 20 nm on which key differences in magnetic properties between dots and thin films can be illustrated. At low temperatures, a paramagnetic Curie-Weiss type signal is observed in the dot sample. As discussed above, this originates from the $SrTiO_3$ substrate. It is also present in the film sample but it is much less pronounced due to the very much larger amount of the ferromagnetic material. The paramagnetic contribution becomes relevant at temperatures below 50 K and does not affect the behavior in the vicinity of the ferromagnetic transition.

Another distinction is a different value of the low-temperature magnetization. In this example, the magnetic moment for dots is smaller: $\approx 1.0\,\mu_B$/Ru in nanodots compared to $\approx 1.5\,\mu_B$/Ru in the film if one excludes the paramagnetic contribution. These values are different for different samples and dot sizes. The origin of it can be intrinsic - the changing magnetic anisotropy and the magnetic

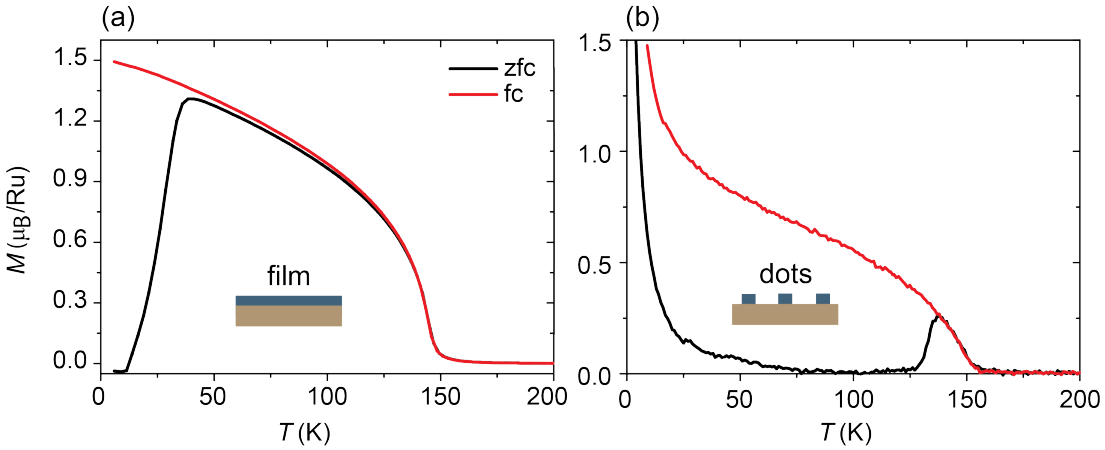

Figure 5.11: Comparison of $M(T)$ curves for (a) a 12-nm-thick film of $SrRuO_3$ (sample #143) and (b) nanodots with a diameter of 20 nm patterned from a similar film (sample #178) measured in an out-of-plane oriented magnetic field of 0.1 T.

domain structure of the dots that lead to different hysteretic properties. This, together with the fact that $M(T)$ curves are measured at rather small magnetic fields, results in a different magnetization maximum at a given field. The spread of parameters comes from an error in the estimation of the amount of $SrRuO_3$ in a sample. The error becomes larger at small dot sizes due to the complex shape of dots (see STEM images in Sec. 4.2).

The magnetic peak temperature T_p, determined as the peak in the zero-field-cooled branch of $M(T)$ (see Fig. 5.4), shifts towards much higher values after patterning. As was discussed above for films, such a drastic increase of T_p can be related to a modification of the magnetic domain structure or a large number of defects appearing on the dot surface as a result of patterning and serving as pinning sites for spins, making it more difficult to magnetize the material.

One of the interesting effects happening in nanodots is the enhancement of T_C as compared to the thin films. This is described in more detail below.

5.4.2 T_C enhancement in nanodots

As was discussed in Sec. 2.1, ferromagnetic nanostructures normally lose their ferromagnetic properties when the material thickness in one or more dimensions approaches several atomic layers. This destabilization of the magnetic ordering happens due to the reduction of the number of nearest neighbors. A similar behavior has been expected in $SrRuO_3$ nanodots. And it is, indeed, observed for dots smaller than 30 nm as is described below. For larger dots, however, we discovered a surprising increase of T_C. It takes place in structures with sizes

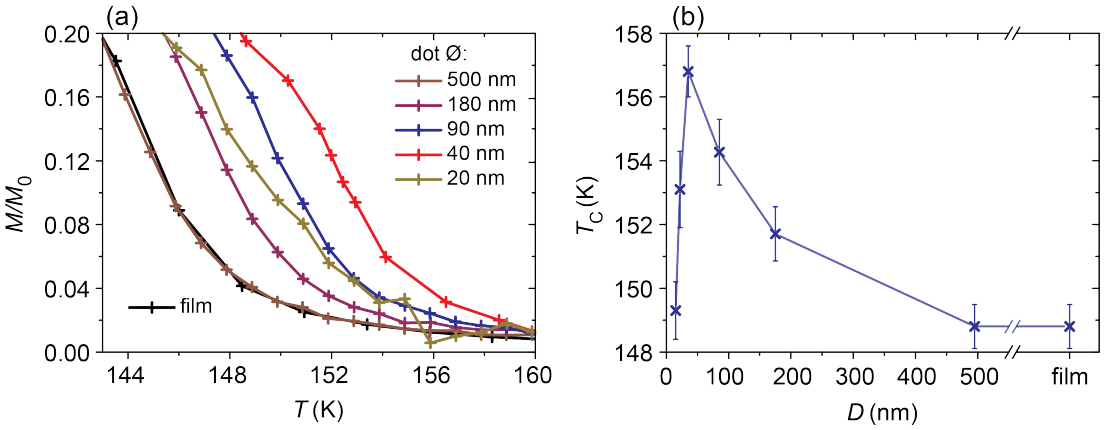

Figure 5.12: (a) $M(T)$ characteristics in the temperature range close to the ferromagnetic transition measured from $SrRuO_3$ dots of various sizes patterned on (100) $SrTiO_3$. All curves are normalized to the magnetization level of the thin film. (b) Curie temperature of the same samples plotted as a function of the dot diameter.

between $\approx$ 200 and 40 nm. This increase is observed systematically and it is reproducible for similar dots. Figure 5.11 shows $M(T)$ for dots with a diameter of 20 nm. $T_C = 153$ K which is 4 K higher than in the corresponding thin film. In order to investigate this effect in detail, a series of samples with dots of different sizes was prepared and the $M(T)$ curves were examined. The size of the dots was varied from 500 to 15 nm, and an unstructured thin film sample was used as a reference. All dots were patterned from films of the same 12 nm thickness and grown at the same deposition conditions on $5 \times 5 \times 0.5\,\mathrm{mm}^3$ (100) $SrTiO_3$ substrates. The initial film morphology was similar. The magnetic properties of all films were measured prior to patterning to confirm that the properties were similar. The magnetic transition was found to occur at $T_C = 149 \pm 1$ K. Dots were formed in rectangular arrays covering $\approx 16\,\mathrm{mm}^2$ of the central area of each substrate. For all samples, the diameter to spacing ratio was kept at 0.5, i.e., the distance between the centers of two adjacent dots equaled two dot diameters.

The measured $M(T)$ curves for the samples are shown in Fig. 5.12(a), and the Curie temperatures extracted from the curves are plotted in Fig. 5.12(b) [134]. Since the saturation magnetization and the shape of the $M(T)$ curves depend on the dot size, all curves in Fig. 5.12(a) have been normalized to the magnetization level of the film. At dot diameters larger than 500 nm, T_C remains the same as in the unstructured film. For smaller dots, T_C starts to increase with decreasing dot size. This increase continues down to dot sizes of $\approx$ 40 nm. At the maximum, the Curie temperature reaches $T_C \approx 157$ K which is close to the T_C of bulk $SrRuO_3$ (≈ 160 K [47]). At this point, the increase of T_C is ≈ 8 K. When decreasing the

dot size further, below 30-40 nm, T_C drops. The drop is more rapid than the increase - with decreasing the size by ≈ 20 nm, T_C goes back to the film value. We suggest that the mechanism of this drop is different from the mechanism of the enhancement at larger sizes. We attribute the drop to the deterioration of ferromagnetic properties due to decreased number of neighbors mentioned in the beginning of this section.

The enhancement of T_C in nanopatterned ferromagnets is an unusual effect which was previously observed only in special nanostructured systems. For example, in nanowires of ferromagnetic semiconductor (Ga,Mn)As, the observed increase of the Curie temperature from 191 to 200 K is attributed to an increase of the free surface after patterning and the resulting diffusion of Mn to sidewalls [219]. The T_C enhancement is explained by the chemical modification of the material. In the case of $SrRuO_3$ nanodots, no such modification is observed as is shown in Sec. 4.2. It is known however, that the ferromagnetism in $SrRuO_3$ is very sensitive to the strain in the material (see Sec. 1.3.1). It is, therefore, interesting to look how the strain distribution in the material changes after patterning and how it may be correlated with the enhancement of T_C.

5.4.3 Strain relaxation

The usual way of measuring the strain in thin films is X-ray diffraction [220]. The application of X-ray diffraction to nanodots is, however, complicated by the small amount of material per substrate area which does not provide an adequate counting statistics. Even with the synchrotron radiation, measurements take a considerable time and spectra are dominated by the substrate signal. Because of this, instead of X-ray diffraction, a STEM-based geometric phase analysis [221] has been used for determining the strain distribution in the nanodots. This was done in collaboration with the Stuttgart Center for Electron Microscopy (StEM, [179]). The geometric phase analysis allows to calculate interatomic distances from high-quality STEM micrographs with a resolution of 0.03 Å [222].

The method was used to analyze high spatial resolution STEM images in the in-plane and out-of-plane directions. It was applied to nanodot samples with dot diameters of 30 and 80 nm, using a thin film sample for comparison. The lattice constant of the $SrTiO_3$ substrate was used as the reference 0% level. Figure 5.13 shows the strain distribution in a $SrRuO_3$ film grown on (100) $SrTiO_3$. The graphs in the right panel are obtained from the line-by-line averaging of the strain map regions marked by the white boxes. The data reveal that the film is fully strained, i.e., the lattice constant in the in-plane direction does not change across the interface, whereas in the out-of-plane direction the unit cell of $SrRuO_3$ is elongated by a constant value of $\approx (1.4 \pm 0.3)\,\%$ compared to $SrTiO_3$. In

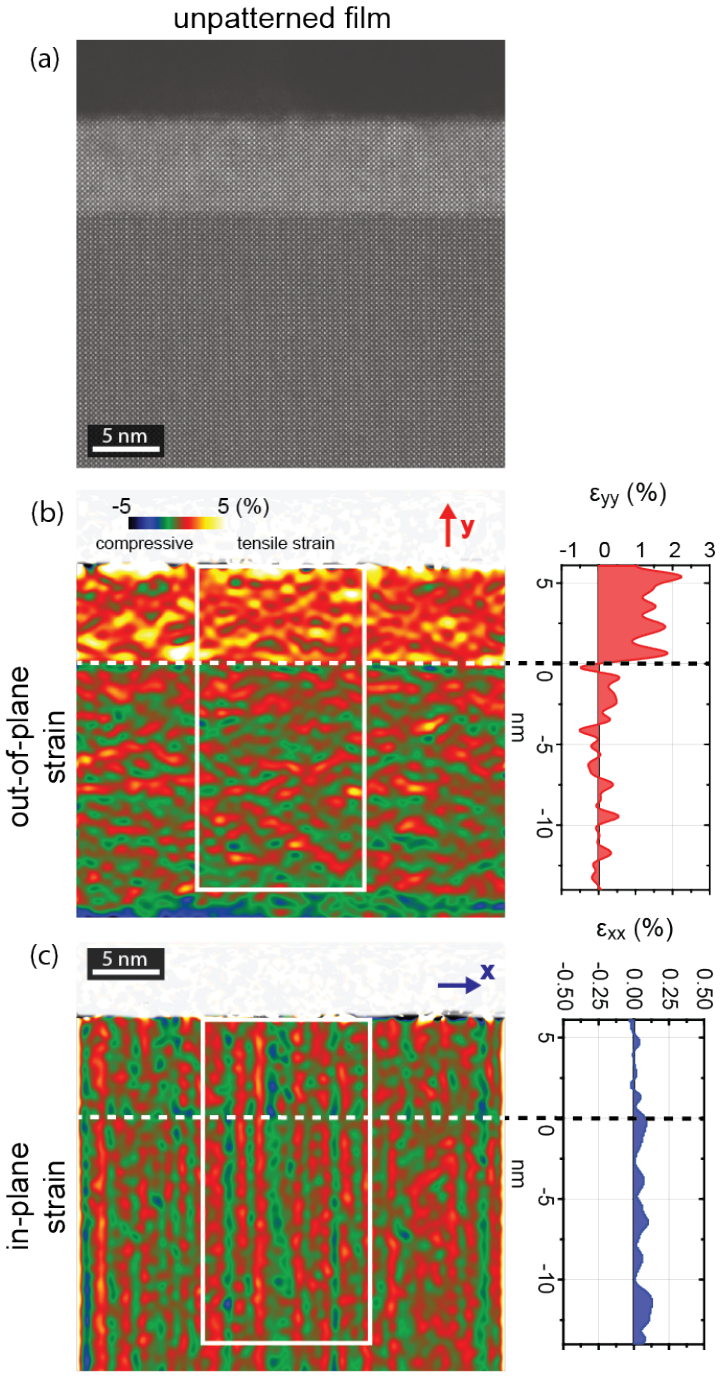

Figure 5.13: (a) Z-contrast STEM image of an unstructured $SrRuO_3$ film with a thickness of $\approx$ 10 nm. The respective strain components in the out-of-plane ε_{yy} (b) and in-plane ε_{xx} (c) directions are obtained from geometric phase analysis.

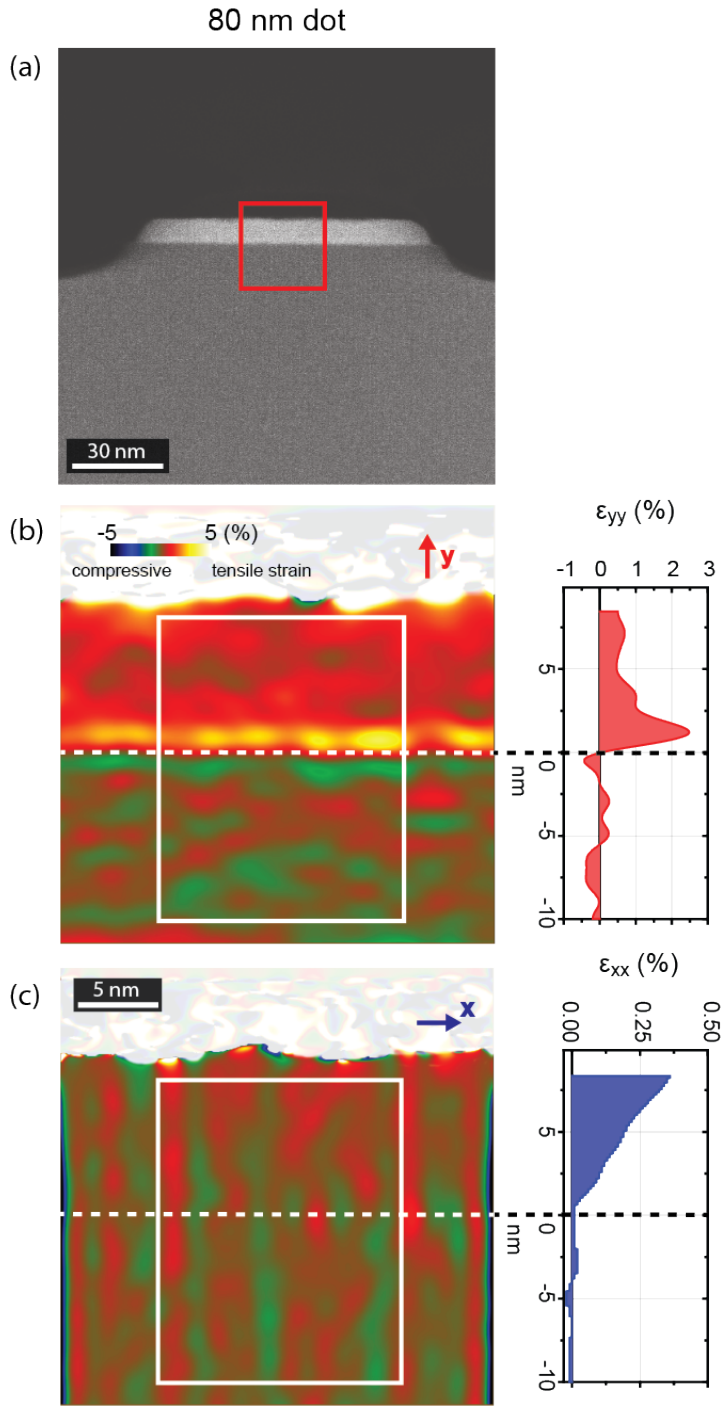

Figure 5.14: (a) *Z*-contrast STEM image of a 80-nm-sized nanodot. The respective strain components in the out-of-plane ε_{yy} (b) and in-plane ε_{xx} (c) directions are obtained from geometric phase analysis. The central region of the dot (red rectangle) is analyzed.

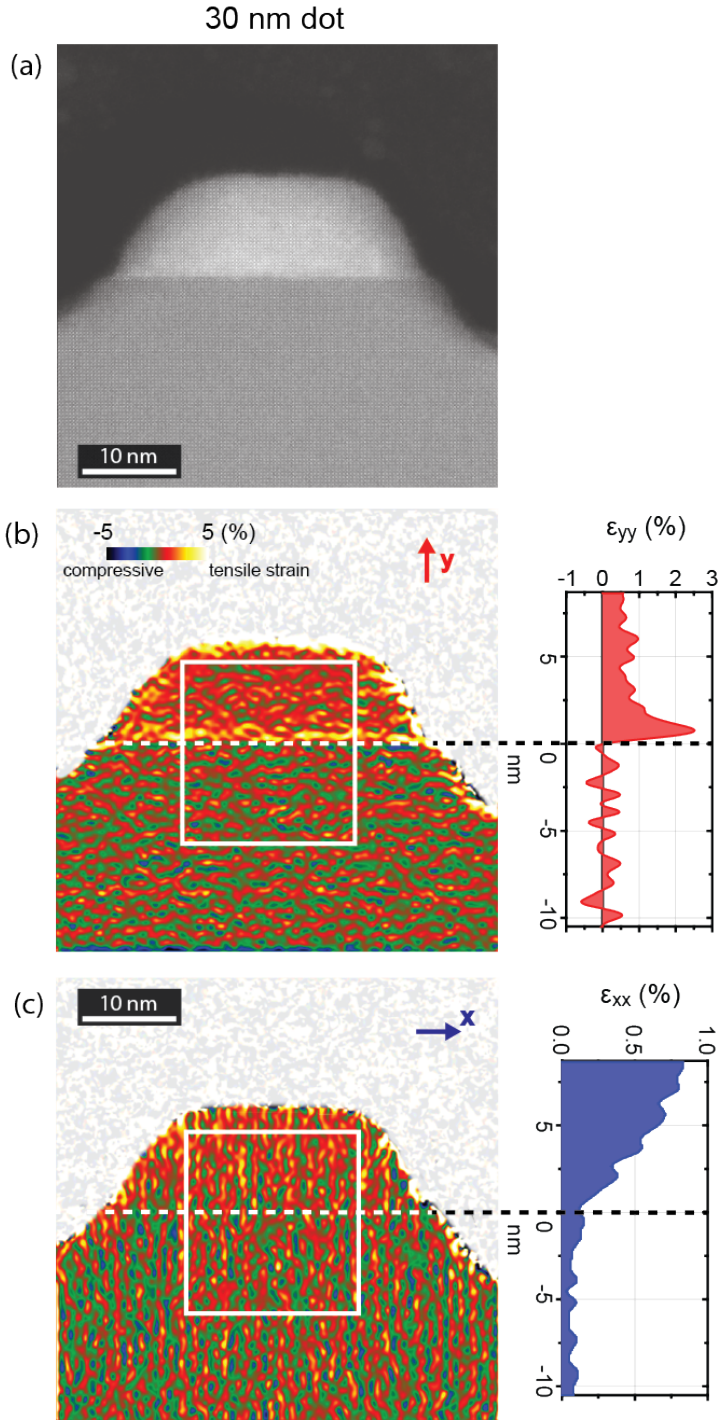

Figure 5.15: (a) *Z*-contrast STEM image of a 30-nm-sized nanodot. The respective strain components in the out-of-plane ε_{yy} (b) and in-plane ε_{xx} (c) directions are obtained from geometric phase analysis.

nanodots these strain characteristics change significantly, as shown by Fig. 5.14 for a 80-nm-diameter dot and Fig. 5.15 for a 30-nm-diameter dot. For both dot sizes, in the in-plane direction, starting from the interface, the lattice constant of $SrRuO_3$ increases gradually, which indicates the strain relaxation. For the 80-nm dot, the lattice constant has relaxed by $\approx (0.35 \pm 0.10)\,\%$ at the top of the dot, whereas for the 30-nm dot the relaxation is stronger. It reaches $\approx (0.75 \pm 0.10)\,\%$, matching fully relaxed $SrRuO_3$.

Considering the literature data [57–59] which link the magnetic properties of $SrRuO_3$ to strain, we conclude that it is this relaxation of the epitaxial strain which is responsible for the enhancement of T_C in nanodots.

In the out-of-plane direction, an interesting behavior is observed as well. Here, in the first two unit cells of $SrRuO_3$ at the interface, the strain is similar to that of the film, and then decays rather quickly together with the lateral strain to approach a three-dimensionally relaxed structure. Similar mechanisms of patterning-induced strain relaxation have been observed before in patterned semiconductor nanostructures, for example in Si [223], InGaN/GaN [224] or (Ga, Mn)As [225].

The deformation of materials under strain occurs according to the Poisson effect which states that a material tends to expand in the direction perpendicular to the direction of compression [226]. The ratio of the transverse to the longitudinal expansion is characterized by the Poisson constant:

$$\nu = -\frac{d\varepsilon_{trans}}{d\varepsilon_{axial}} \tag{5.4}$$

where $d\varepsilon_{trans}$ and $d\varepsilon_{axial}$ are the strains in transverse and longitudinal directions, respectively. According to DFT calculations existing in the literature, the Poisson ratio for bulk orthorhombic $SrRuO_3$ varies in the range of $\nu = 0.334 - 0.345$ depending on the calculation method [227]. For our samples, considering the relaxed lattice constants of $SrRuO_3$ and $SrTiO_3$ of $a_{STO} = 0.3905\,\text{nm}$ and $a_{SRO} = 0.393\,\text{nm}$ and the strain distribution in the $SrRuO_3$ thin film (Fig. 5.13, one obtains a Poisson ratio of $\nu = 0.59 \pm 0.23$ which is larger than the literature value but still fits within the error margin.

5.4.4 Magnetic hysteresis

The analysis of the changes of magnetic hysteresis induced by the patterning is challenging. Even in bulk media, hysteresis curves can exhibit a rather complex behavior that is governed by the interplay between ferromagnetism, magnetic anisotropy and the magnetization reversal mechanism. In nanopatterned structures, this behavior is further complicated by the shape anisotropy and the magnetic dipole-dipole interaction between the nanoobjects. When patterning a

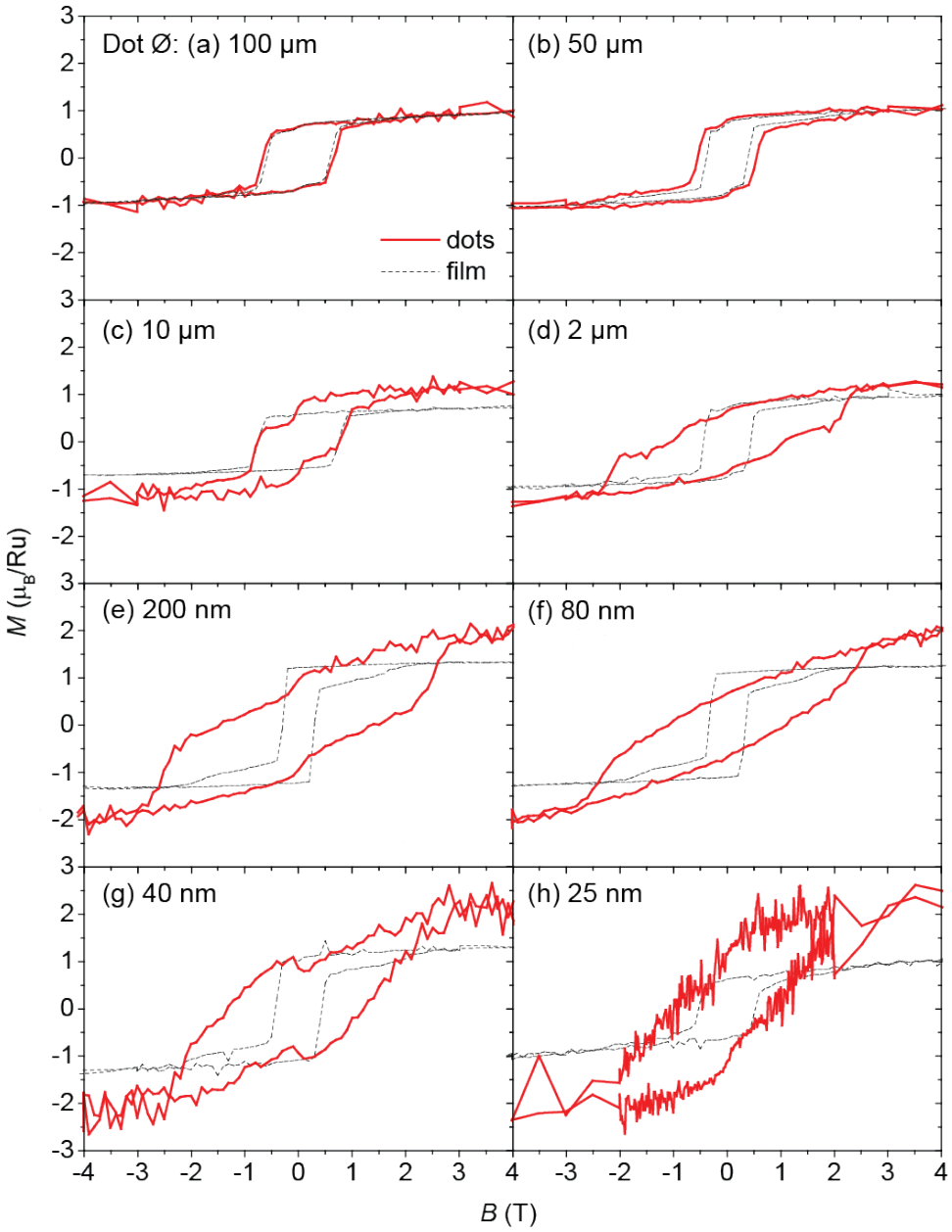

Figure 5.16: Modification of hysteresis loops with changing dot diameter. The hysteresis curves for dots are depicted in red. Black lines show the hysteresis loops measured on the same films before patterning. For dots larger than 10 μm, the hysteresis closely matches the one of the thin films. For smaller dots, it transforms to a more elongated shape with higher coercivity and saturation magnetization. All curves have been measured at $T = 15\,\mathrm{K}$ in an out-of-plane oriented magnetic field.

material from a thin film into an array of nanodots, all characteristics mentioned may change at once. This makes it difficult to separate different influencing factors from one another and to determine which of the parameters play a key role in the changes.

To trace the evolution of the magnetic hysteresis from thin films to nanodots of $SrRuO_3$, a series of samples with different dot sizes has been produced. The structure size was varied over a considerable range, of hundreds of μm to 15 nm, the smallest dot size we could achieve. The height of all structures was kept at 12 nm which was also the thickness of the initial $SrRuO_3$ films. Large dots (with sizes ≥ 200 nm) had a rectangular shape to maximize the amount of $SrRuO_3$ on a substrate and to speed up the e-beam exposure. Smaller dots are rounded as we approach the resolution limit of e-beam lithography. The distance between the dots was scaled proportionally with the dot size and for this series equaled three lengths of the dot side. All curves were measured at $T = 15$ K. This value has been chosen to reduce the paramagnetic contribution which becomes more noticeable at a lower temperature.

The hysteresis curves measured for the dots of different sizes are shown in Fig. 5.16. The behavior of the dots is plotted in red and the black lines display the corresponding thin film reference for each sample. At dot sizes of 100 and 50 μm (Fig. 5.16(a,b)), the shape of the curves measured on the dots mirrors the ones of the thin films. The only difference is a slightly higher value of the coercive field B_c, probably originating from the material damage. The 10 μm dots (Fig. 5.16(c)) can be considered as the intermediate size between film and dots. Here, the shape of the curve starts to be modified in several respects. First, a sharp flip of the magnetization at B_c typical for the films develops into a more gradual one. Also, an additional reduction of the magnetization close to zero magnetic field takes place in some samples. This reduction is more frequently observed in the dots with sizes of $\approx 50 - 200$ nm. However, it is not completely reproducible and may be present and absent in different samples with nominally identical characteristics. Finally, the value of the saturation magnetization M_{sat} consistently becomes larger with smaller dot size. When reducing the dot size further, these transformations become more prominent - the curves tilt more and M_{sat} increases, finally reaching a value of $M_{sat} \approx (2.0 \pm 0.5)\,\mu_B$/Ru.

All the differences described above can be caused by a set of reasons including the dipole-dipole interaction between dots, changes in the magnetic domain structure or the magnetic anisotropy. More background about these characteristics is provided in Sec. 2.1. In the following section it will be discussed which of these factors make the greatest contribution to the behavior modification.

Temperature dependence. With increasing temperature, the hysteresis loops change, reflecting the decay of the ferromagnetic interaction. Figure 5.17 shows

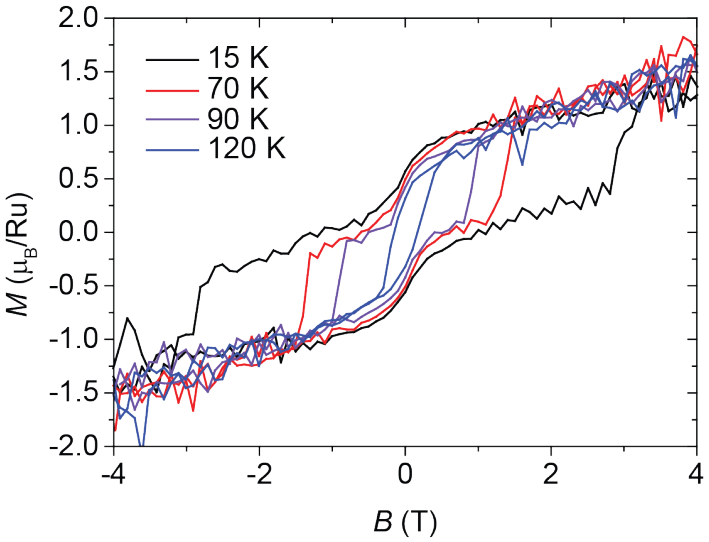

Figure 5.17: Temperature dependence of the hysteresis loop of a sample with 80-nm-diameter dots (sample #213). The contraction of the loop with increasing temperature is visible.

hysteresis curves measured on a sample with 80-nm-diameter dots measured at several temperatures below T_C. At temperatures well below the ferromagnetic transition ($< 100\,\mathrm{K}$), the overall shape of the curve with its characteristic features persists. What changes is the coercive field B_c, which reduces due to the higher thermal energy of the material. At temperatures closer to the ferromagnetic transition, the loops become narrow and the curve features become indistinguishable. Such behavior is also present in $SrRuO_3$ films and is consistent with the theoretical predictions [228] and experimental observations for nanoparticles of other materials [229].

5.4.5 Magnetic anisotropy

Magnetic anisotropy is a complex quantity consisting of a large number of physical properties of different nature. For an arbitrary magnetic system, the magnetic anisotropy energy can have the following contributions [102]:

$$E = E_{crys} + E_{shape} + E_{surface} + E_{stress} + E_{exch} \tag{5.5}$$

where E_{crys} is the magnetocrystalline anisotropy, E_{shape} is the shape anisotropy, $E_{surface}$ is the anisotropy related to surface effects, E_{stress} is the stress anisotropy, and E_{exch} is the exchange anisotropy. The magnetic anisotropy is not a scalar quantity. Every component has one or more preferential directions, called easy axes. This is additionally complicated by the presence and structure of magnetic domains that affect the magnetization reversal through domain boundary motion or domain magnetization rotation. A more detailed theoretical background can be found in Sec. 2.1.

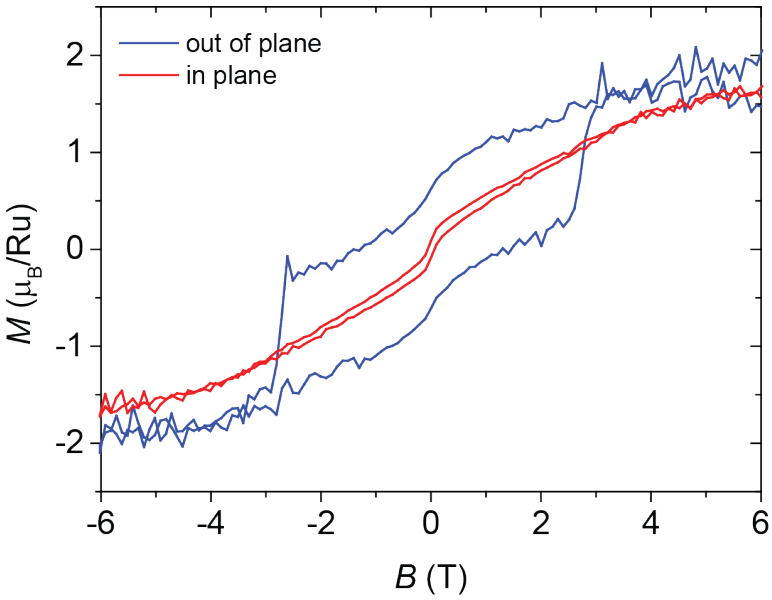

Figure 5.18: Hysteresis loops measured in the out-of-plane and in-plane orientations for nanodots with a diameter of 50 nm and a thickness of 12 nm at $T = 15$ K (sample #218).

For systems of nanoobjects, having a complicated shape, a non-uniform crystal structure and interacting with each other, a comprehensive analysis of the anisotropic properties is a highly non-trivial task. Luckily, $SrRuO_3$ belongs to the hard magnetic materials with an extremely high intrinsic anisotropy energy. This makes the analysis more straightforward as we expect the magnetocrystalline term to dominate the anisotropy energy.

The approximate orientation of the magnetic easy axis can be determined from angular measurements of the magnetization curves. An example of such a measurement for thin films was shown in Fig. 5.9. For a uniaxial magnetic system like $SrRuO_3$, the orientation with the largest ratio of the remanent to the saturation magnetization M_{rem}/M_{sat} indicates the magnetic easy axis and the one with the smallest magnetization - the hard axis. From the image it can be seen that the ratio decreases from $(M_{rem}/M_{sat})_\perp = 0.85$ to $(M_{rem}/M_{sat})_\parallel = 0.34$ with increasing angle between the magnetic field and the film normal from $\alpha = 10°$ to $\alpha = 90°$. At small angles, M_{rem}/M_{sat} is close to one which indicates that the magnetic easy axis is oriented close to the film normal. A similar measurement is shown in Fig. 5.18 for nanodots with a diameter of 50 nm and a thickness of 12 nm. Here, M_{rem}/M_{sat} changes from $(M_{rem}/M_{sat})_\perp = 0.44$ in the out-of-plane to just $(M_{rem}/M_{sat})_\parallel = 0.12$ in the in-plane orientation. For a different sample with 200-nm-size dots (sample #098), the values are $(M_{rem}/M_{sat})_\perp = 0.51$ and $(M_{rem}/M_{sat})_\parallel = 0.32$, correspondingly, which are intermediate between the film and the smaller dots. In these calculations, the region of the coherent magnetization rotation is extrapolated to the intersection with the $B = 0$ axis to ignore the rapid magnetization drop at small fields which is not related to

anisotropy. The results indicate that the easy axis for dots shifts to a new angle. This may happen due to the structural relaxation of the material inside the dots which was described in Sec. 5.4.3. Similar effects were found in [230, 231].

The value of the anisotropy can be evaluated using several models and methods. One of the most successful approaches is the law of approach to saturation (LAS) [232] that describes the behavior of the magnetization in an external field close to the saturation M_s ($H \gg H_c$) and at temperatures well below the ferromagnetic transition ($T \ll T_C$) according to the equation:

$$M = M_s(1 - \frac{a}{H} - \frac{b}{H^2}) + \chi H \tag{5.6}$$

where a, b and χ are constants. The a/H term is the magnetic hardness arising from the stress caused by the crystalline defects or from the leakage field [233]. χH is referred to as the paramagnetism-like term and is considered to be the consequence of defects. More important for this discussion is the quadratic term b/H^2 [234] which describes the influence of the magnetocrystalline, shape and stress anisotropies with the parameter

$$b = \varepsilon H_k^2, \tag{5.7}$$

where H_k is the anisotropy field and ε is a microscopic coefficient that depends on the crystal geometry (for isotropic cubic systems $\varepsilon = 32/105$). By finding the parameter b from fitting the magnetization curve, one can determine the anisotropy field and calculate the anisotropy constant K_u:

$$2K_u = H_k \mu_0 M_s \tag{5.8}$$

where μ_0 is the permeability of free space.

The described model does not fit our hysteresis curves well. The reason for this rests in the complexity of our magnetic system. Little is known about the precise orientation of the magnetic easy axis or the exact amount of material in the nanodots which is required to calculate the saturation magnetization. This introduces a large uncertainty for the choice of the fitting parameters. One can simplify the treatment using a simpler but less precise method. It determines the anisotropy field H_k from the slope dM/dH of the magnetization curve at low fields below the saturation region [235]:

$$H_k = \frac{M_{sat}}{dM/dH} \tag{5.9}$$

and then immediately uses Eq. 5.8 to calculate K_u. Such an approach is valid for the hysteresis loops measured along or close to the hard magnetic axis. Since for our nanodot samples the orientation of the easy axis is known only approximately,

we consider the following calculations only as an estimation. For the thin films of the data set shown in Fig. 5.8, the evaluation gives values of $H_k = 9.3\,\mathrm{T}$ and $K_u = 7.3 \cdot 10^5\,\mathrm{J/m^3}$. These are in the range found by other researchers [236, 237]. For nanodots (Fig. 5.18), the values change to $H_k = 6.3\,\mathrm{T}$ and $K_u = 9.9{\cdot}10^5\,\mathrm{J/m^3}$. It can be seen that despite the reduction of H_k in nanodots, the total magnetic anisotropy tends to increase. This happens due to a significantly higher saturation magnetization in the samples. Nevertheless, the calculated values are of the same order of magnitude and more precise measurements using different methods are required to fully understand the magnetic anisotropy modification in the nanodots.

5.4.6 Interaction between dots

Magnetic dots of size l interact with each other by means of the dipole-dipole interaction [103] which decreases with distance as a function of $1/r^3$:

$$H_d = \frac{2mr}{[r^2 - (l/2)^2]^2}; \quad H_d = \frac{m}{[r^2 - (l/2)^2]^{3/2}}. \tag{5.10}$$

The first equation is valid for a point along the line of the dipole and the second one along the line perpendicular to it. Even with such a rapid decay, the effects of interaction between nanodots can be observed at scales of up to several microns. For example, a square dot of $SrRuO_3$ having a typical magnetization $M = 1.5\,\mu_\mathrm{B}/\mathrm{Ru}$, a size of $100 \times 100\,\mathrm{nm^2}$ and a thickness of 12 nm creates a stray field of $H \approx 3800\,\mathrm{A/m^2}$ at a distance of 200 nm from its center. For arrays, this value depends also on the nearest neighbors. They can make positive or negative contributions depending on the orientation of their magnetic moment. If we assume the former case, the interaction may exceed $\approx 2 \cdot 10^4\,\mathrm{A/m^2}$ for a square array of dots, considering four nearest and four second-nearest neighbors. By increasing the distance between dots to 500 nm, the stray field drops to just $\approx 1200\,\mathrm{A/m^2}$. Even though the interaction strength changes by orders of magnitude with increasing spacing, the question of whether it may affect the behavior of the system depends on the scale of other characteristic energies, e.g. the magnetic anisotropy and domain wall pinning.

To study the effects of the interaction between the dots, a series of samples has been produced. The samples contain rectangularly shaped nanodots of $SrRuO_3$ with a side length of 200 nm and a thickness of 12 nm formed into rectangular arrays with different periodicities of 400, 600 and 800 nm. The increasing dot spacing is intended to decrease the amount of the stray field experienced by the dots, changing the setup from a strongly interacting to an isolated ensemble. Even at 800 nm spacing, the interaction is expected to be non-negligible. A further reduction of interaction is complicated as samples become more and more diluted

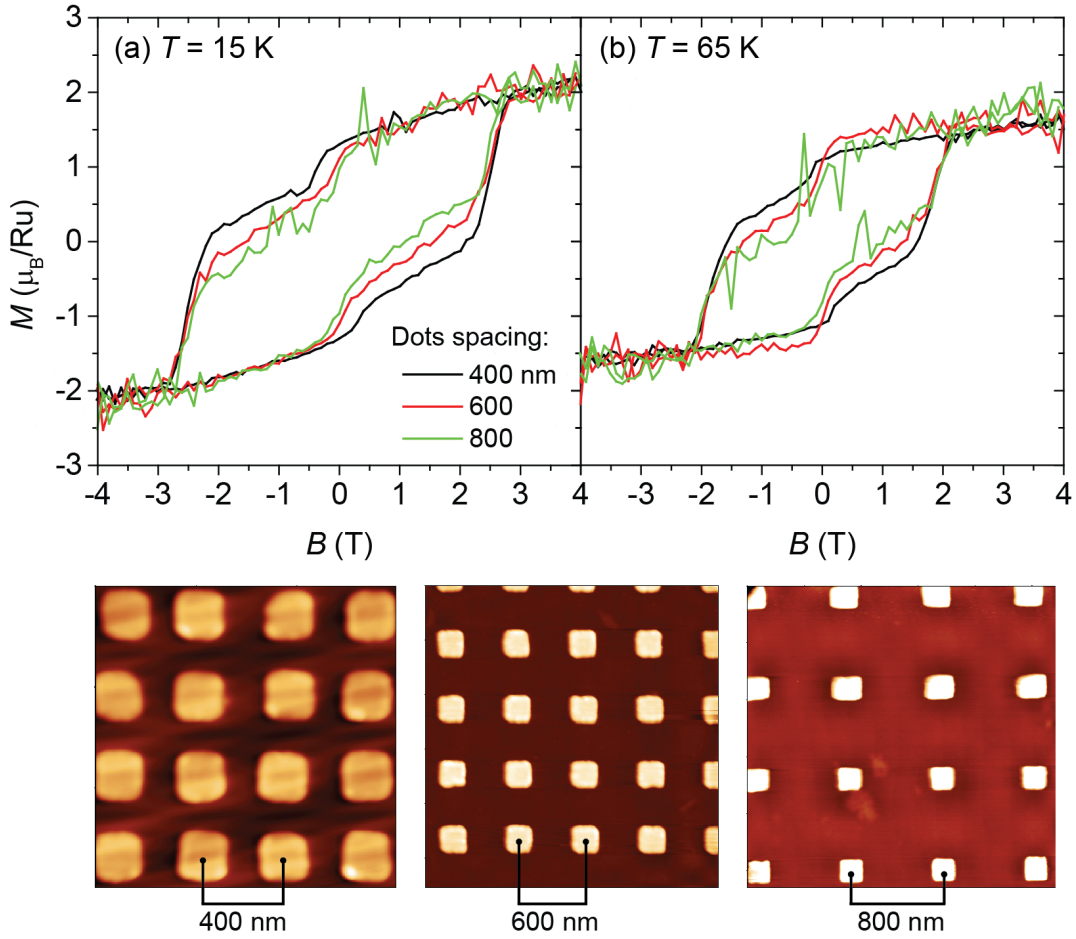

Figure 5.19: Hysteresis loops measured on rectangular arrays of $SrRuO_3$ dots with dot spacings of 400, 600 and 800 nm. The size of a dot is 200 nm and the thickness is 12 nm. The curves are measured at (a) $T = 15$ K and (b) $T = 65$ K. The bottom part of the figure depicts AFM images of the corresponding samples.

with increasing periodicity, thus decreasing the signal to noise ratio. Figure 5.19 shows hysteresis loops measured for three samples with the different dot spacing. All samples were measured with out-of-plane orientated magnetic field at temperatures of $T = 15\,\mathrm{K}$ (Fig. 5.19(a)) and $T = 65\,\mathrm{K}$ (Fig. 5.19(b)). At high fields, above $\approx 2.5\,\mathrm{T}$, the loops for different samples coincide quite well, while at smaller field the behavior is discrepant. The major differences are observed in the region of moderate magnetic field – from 0 to 2.5 T – in one of the shoulders of the loops. At the beginning of each scan (the starting point is at high positive magnetic field of 5-7 T), all samples show the same magnetization. When the field is swept downwards, the magnetization follows essentially the same line for samples with different dot periodicities. While sweeping the field down, close to 0 T, the behavior changes and the magnetization of every sample pursues its own path. At 2-3 T field in the opposite direction, the curves merge again and the magnetization saturates rather rapidly.

In the region of changing behavior, the smaller dot density results in a smaller total magnetization. The more dilute samples tend to reduce the amount of the external stray field by forming some sort of complex magnetic structures. Such structures can be magnetization states with no or reduced external field at remanence, e.g., magnetic vortexes, closure domains states, or demagnetization "checkerboard" structures formed by dots ensembles. More details are given in Sec. 2.1. From theoretical considerations, both the vortex and demagnetization checkerboard states can result in a behavior similar to the described above. However, in $SrRuO_3$, both the magnetic anisotropy field ($H_k \sim 6.3\,\mathrm{T}$) and the reversal field ($H_r \sim 3.5\,\mathrm{T}$) [238] are much larger than the expected interaction strength between the nanodots. Therefore, it would be interesting to perform low-temperature magnetic force microscopy on such type of samples to figure out in detail which of the mechanisms is responsible for the observed behavior.

Chapter 6

Nanolines of $SrRuO_3$

The magnetic measurements of nanodots described in the previous chapter reveal many intriguing aspects of the behavior of nanostructured $SrRuO_3$. Here, we use a different approach that complements the understanding of the material properties at the nanoscale. In this chapter, electrical transport measurements are utilized to study the $SrRuO_3$ nanostructures in the form of nanolines.

6.1 (110) $DyScO_3$ as a substrate for nanolines

To explore nanolines, several modifications to the process used for the fabrication of nanodots (see Ch. 3) have to be made. The most significant one is a change of the substrate material. Pure $SrTiO_3$ possesses rather good insulating properties with typical resistances in the GΩ range. However, under the influence of the ion irradiation which is a necessary part of the used nanostructuring technology, the conductivity of the substrate surface strongly increases due to the formation of vacancies [239]. Figure 6.1 shows the sheet resistance of a (100) $SrTiO_3$ substrate surface as a function of temperature for a bare substrate etched during 300 s using Ar ions (sample #160). The data was acquired using the same 4-probe van der Pauw technique described in Sec. 4.1.1. The measurement shows that already at room temperature the sample surface has a resistance of the order of several kΩ. As is shown further in this chapter, this is comparable to the resistance of $SrRuO_3$ nanolines. Furthermore, when cooling the substrate, the resistance drops abruptly and at a temperature of 2 K amounts to just several Ω. Such a surface can by no means be considered suitable for the fabrication and measurement of conducting nanodevices. For this reason, another substrate material - (110) $DyScO_3$ - was selected.

Only a limited number of substrate materials exist that are suitable for the reproducible growth of high-quality epitaxial films of $SrRuO_3$. The most popular

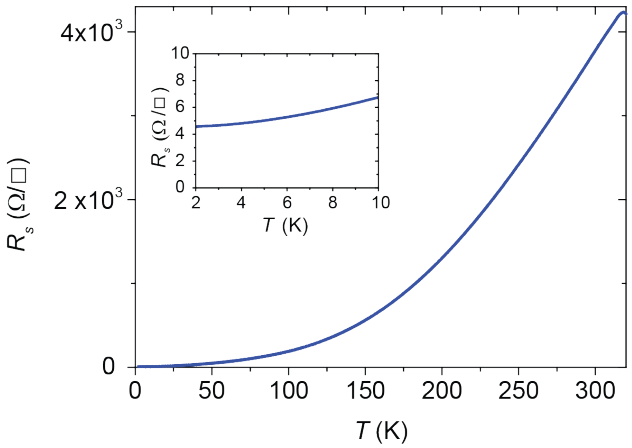

Figure 6.1: Sheet resistance of a bare $SrTiO_3$ substrate subjected to Ar ion milling for 300 s (sample #160). The curve is measured using a 4-probe van der Pauw geometry. The inset shows the low-temperature region of the curve.

one is, indeed, $SrTiO_3$. Besides it, $LaAlO_3$ [240], $DyScO_3$ [241], $NdGaO_3$ [242] and LSAT [243] substrates are used. Unfortunately, none of these substrates are free of problems. $LaAlO_3$, for example, develops twins [244], and $DyScO_3$ or $NdGaO_3$ are strongly paramagnetic [82, 245].

The choice of $DyScO_3$ as a replacement material can be justified by its great insulating properties even after ion irradiation, and a suitable lattice constant. Its magnetization of $\approx 8\mu_B$/Dy ion, however, makes it unacceptable for magnetic measurements at low temperature. Another drawback is related to strict requirements for the substrate surface. It is known that $SrRuO_3$ prefers to grow selectively on the Sc oxide terminated planes [241]. Because of this, any termination inhomogeneities of the substrate may have negative influence on the film morphology (see Sec. 4.1.2). On the other hand, the same phenomenon of selective growth was utilized to prepare self-organized $SrRuO_3$ nanolines on $DyScO_3$ [28]. The choice of growth parameters is therefore governed by an interplay of the conditions necessary to achieve a uniform film morphology and the conditions at which the film quality is best. The competing requirements result in worse film properties (including electrical transport) than those grown on $SrTiO_3$. The XRD measurements described in Sec. 4.1.2 (Fig. 4.7) show that in the narrow window of growth parameters where the uniform film morphology can be achieved, the increased density of defects in the film results in a larger $SrRuO_3$ lattice parameter.

Figure 6.2 shows the sheet resistance as a function of temperature for a 12-nm-thick $SrRuO_3$ film grown on (110) $DyScO_3$. Similar measurements performed on a film of the same thickness and area grown on $SrTiO_3$ can be seen in Fig. 4.4. Compared to the ones grown on $SrTiO_3$, the film exhibits a higher value of sheet resistance $R_s = 228\,\Omega/\square$ at room temperature, a lower value of $T_C = 118\,\mathrm{K}$ determined as the average value between peaks in the resistance anomaly during

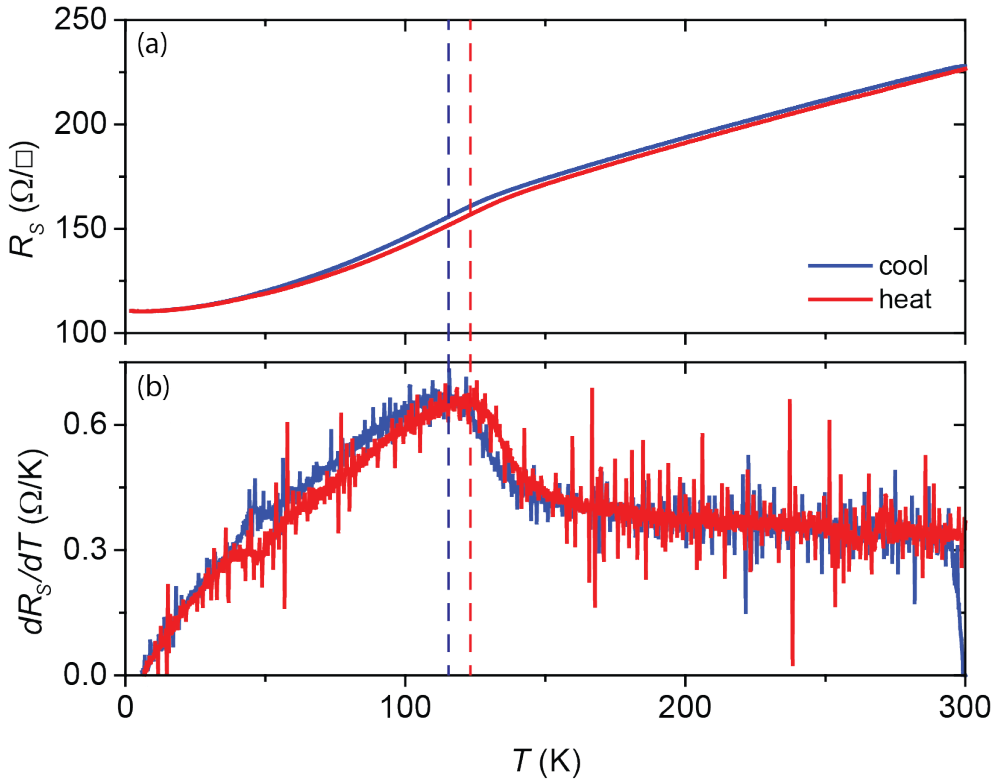

Figure 6.2: (a) Sheet resistance measured as a function of temperature for a 12-nm-thick $SrRuO_3$ film grown on (110) $DyScO_3$ (sample #206). The red and blue curves correspond to cooling and heating the sample with a rate of 2 K/min. The difference between them is related to the temperature lag of the setup. (b) Temperature derivatives of the same curves showing the resistivity anomaly of $SrRuO_3$ at T_C.

cooling and heating, and a residual resistance ratio $R_{300K}/R_{4K} = 2.1$. These values are worse than for the films grown on $SrTiO_3$. Nevertheless, such properties are acceptable for the fabrication of nanodevices.

6.2 Nanoline design

The main issues that have to be considered when preparing sample layouts for the nanolines are the same as for the nanodots. A detailed description can be found in Sec. 3.4.1. In fact, the fabrication of the nanolines is easier because the structure density is much smaller. That allows to avoid problems with the proximity effect, reduce the exposure time and significantly facilitate the lift-off process.

Figure 6.3 shows how a typical nanoline sample layout looks like. The working area is limited to $3 \times 4\,\mathrm{mm}^2$ in the central part of a substrate to avoid inhomo-

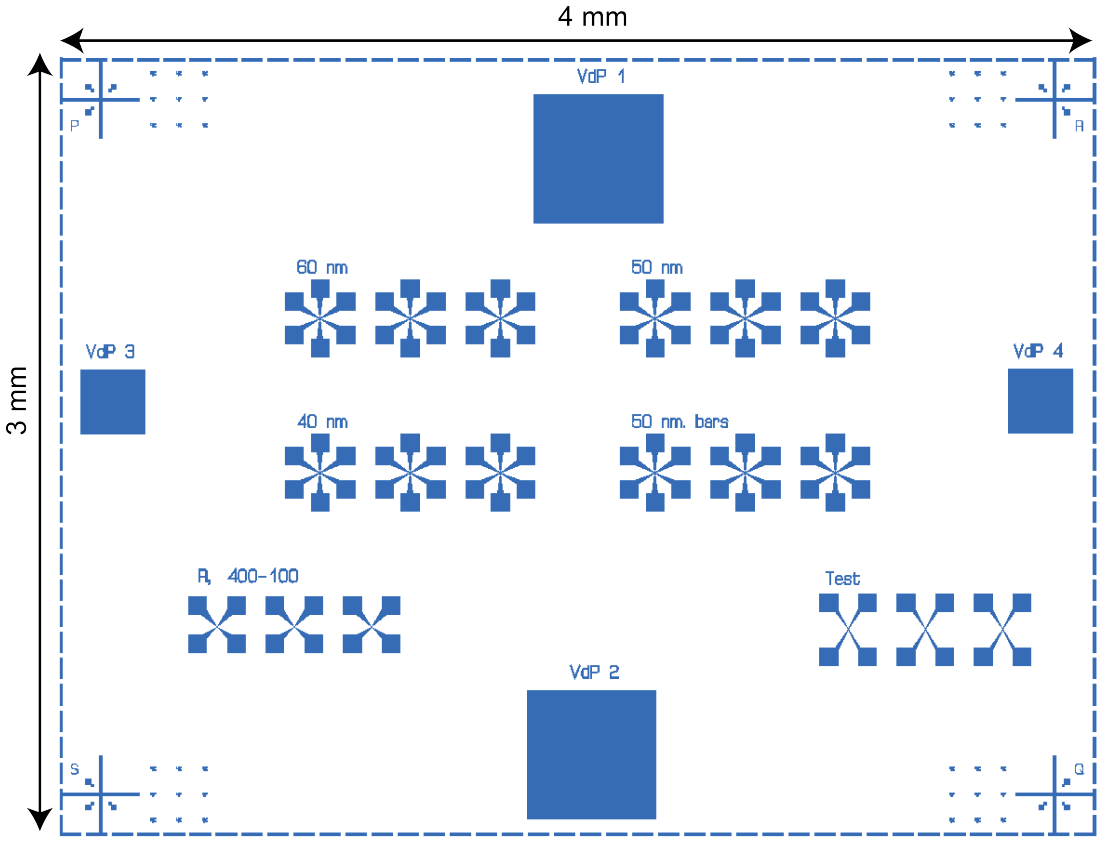

Figure 6.3: A typical design of a nanoline sample layout. The usable area of the substrate is $4 \times 3\,\mathrm{mm}^2$. Inside the area several types of devices are located. The types include nanolines with different width, regions of unpatterned film and test structures used to check the substrate conductivity.

geneities in the film structure and e-beam resist close to substrate edges. Each sample contains several types of structures. This includes nanolines of different width and test structures to confirm that the substrate is insulating. Also, several regions of unpatterned film with an area of about 0.1 - 0.25 mm^2 each are left on the substrate for reference van der Pauw measurements [173].

Most of the area of each device is covered by contact pads and contact wires. The contact pads are squares with a side length of 50 μm. The first contact pads were produced with additional Au/Pd metal layers overlapped with $SrRuO_3$. It was found, however, that the adhesion of the metals to $DyScO_3$ is rather weak, leading to the exfoliation of the pads during wire bonding and measurements. Therefore, it was decided to wire bond directly to the $SrRuO_3$ layer which is well visible in the optical microscope. The devices themselves are located at the intersection of the contact wires. Some examples of the structures are shown in Fig. 6.4. Figures 6.4(a-c) depict large and small scale layouts of a 50-nm-

wide nanoline and the corresponding top-view SEM image of the real structure. The width of the nanolines was varied from 100 nm to 40 nm. The fabrication of thinner nanolines is possible but costs yield and reproducibility. Access to the nanolines is provided through four electrodes, two attached to the ends of the nanoline and two at a distance of 200 nm from the ends. The lengths of the nanolines are 1 μm between the outer and 600 nm between the inner electrodes. Also, side gate electrodes were fabricated. This results in a total of six contacts for each device. Figures 6.4(d-f) show similar images for a test structure used to check the substrate conductivity as leakage currents play an important role during the measurements. Every structure is repeated several times due to the high probability of defects and imperfections that may completely ruin a device at such small scales.

$DyScO_3$ is not a good substrate for SEM due to significant charge accumulation at the surface induced by electron beam irradiation. To perform the microscopy, the sample surface was covered with a 1-nm-thick layer of Ir to facilitate the charge dissipation. This makes further measurements impossible. For this reason, all microscopic images shown were obtained only after the other measurements were completed.

6.3 Measurement procedure

The nanoline samples were measured in a PPMS P9 setup using the AC measurement mode. Substrates were mounted on 30-pin chip carriers (see Fig. 6.5(a)) using conducting silver paste as a glue. Sliver paste was chosen due to its good temperature stability. The chip carriers were then installed onto a multi-function probe of the PPMS system. For $R(T)$ and $R(B)$ measurements the standard functionality of the PPMS was used. For the measurement of $I(V)$ curves, electrical signals were applied using Keithley voltage and current sources. Figure 6.5(b) shows the basic scheme of the power supplies connected to a nanoline and its gate electrodes. The current was sourced to the outer contacts of the nanolines and the voltage drop was measured between the inner electrodes using a Keithley 2400 SourceMeter. The inner electrodes were chosen for the voltage drop measurement to avoid possible inhomogeneities close to the nanoline edges. One of the ends of the nanolines was grounded. The voltage for the gate electrodes was supplied using a Keithley 2612A SourceMeter. To contact the devices from the outside, samples were bonded using Al wires as illustrated in Fig. 6.5(c). Due to the limited number of available contacts on a chip carrier, only four devices on a sample could be bonded at once.

The nanolines can carry up to several hundreds μA of current, which corresponds to a voltage drop of about 1 V (the resistance is in the range of several

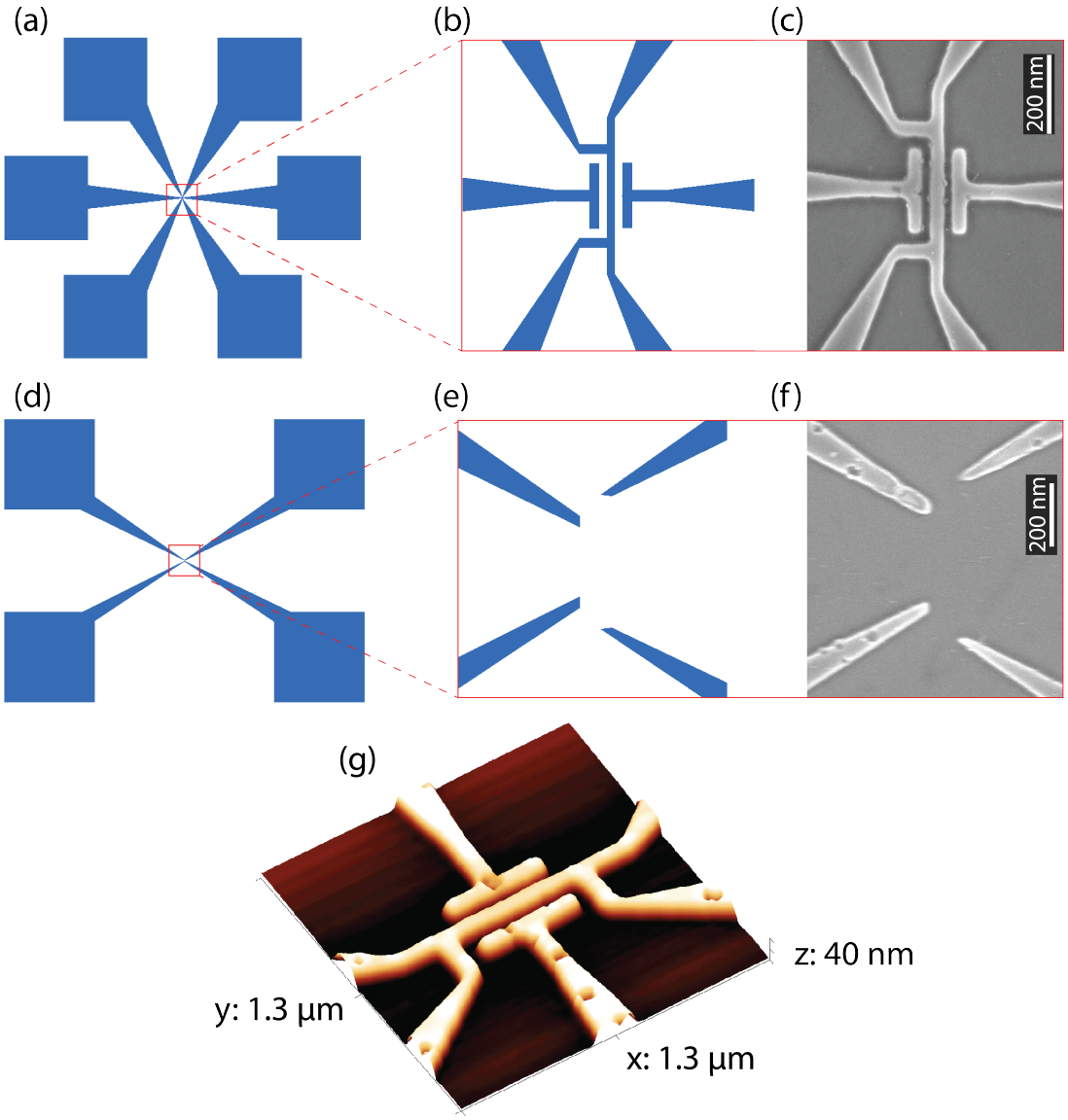

Figure 6.4: (a,d) Large scale and (b,e) small scale images of layouts for a 50-nm-wide nanoline (top) and a test structure (bottom) used to measure the substrate conductivity. (c, f) Corresponding top view SEM micrographs of the fabricated structures. (g) A 3D-representation of an AFM image of a 50-nm-wide nanoline with side gates. A few structural defects are visible.

kΩ as is shown below). However, if a nanoline contains fabrication defects, it can be easily destroyed by applying the power either to the nanoline itself or to the gate electrodes. Examples of the damaged devices imaged after the measurement are shown in the SEM microscopy images in Fig. 6.6. For these devices, the side gates have been fabricated in the shape of needles.

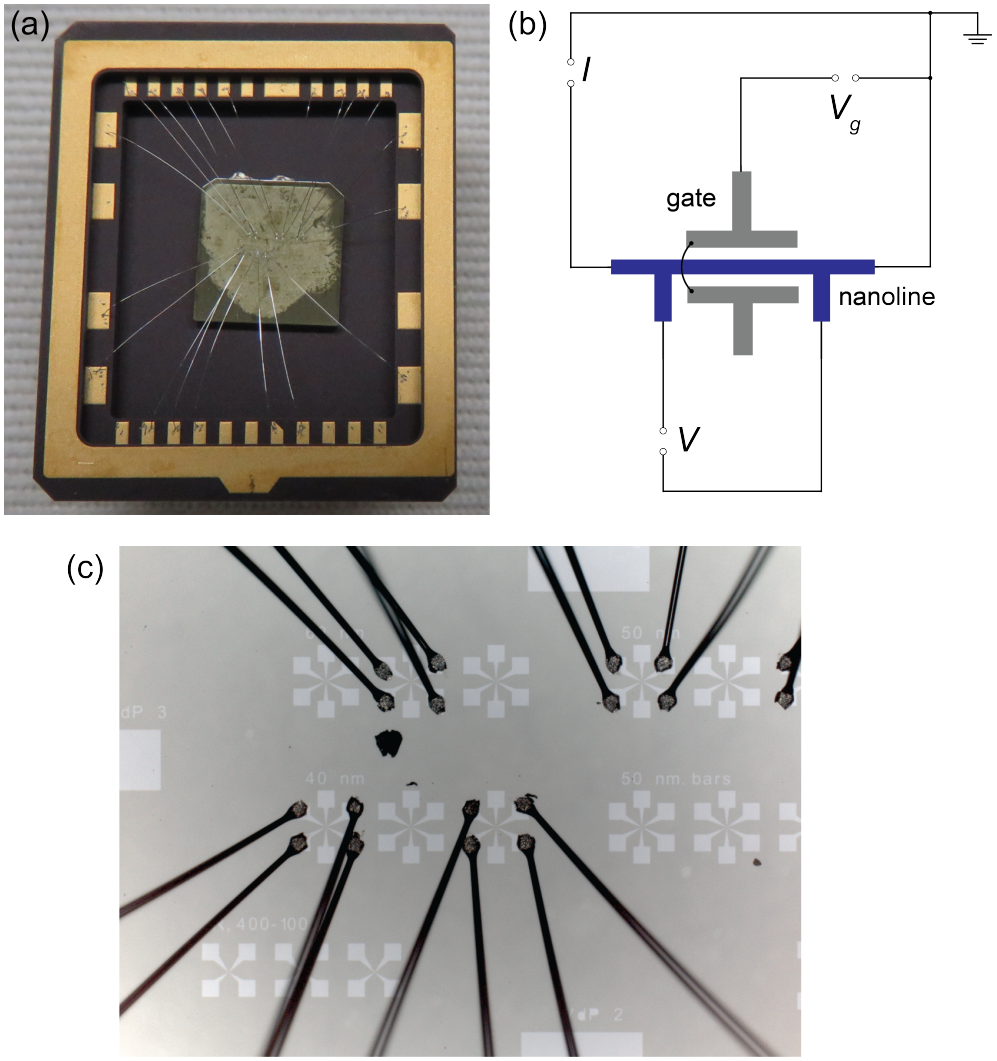

Figure 6.5: (a) A sample mounted on a 30-pin chip carrier using silver paste as a glue (sample # 205). Nanoline devices are contacted by Al wires. (b) Wiring diagram used for $I(V)$ measurements showing the connection of the nanoline electrodes to external power supplies. (c) Magnified view of the sample showing contact pads for the nanodevices as seen through an optical microscope. The structures are well visible in the optical microscope.

The application of a magnetic field to $DyScO_3$ is another issue that has to be addressed here. As was mentioned above, the material is strongly paramagnetic. This substantially limits the amount of external magnetic field which a sample can survive, especially at low temperatures. It was found that at $T = 2\,\mathrm{K}$ it is usually enough to apply the field of $\approx 1 - 1.5\,\mathrm{T}$ to damage the sample or even break the substrate into pieces. Even at higher temperatures, where the substrate

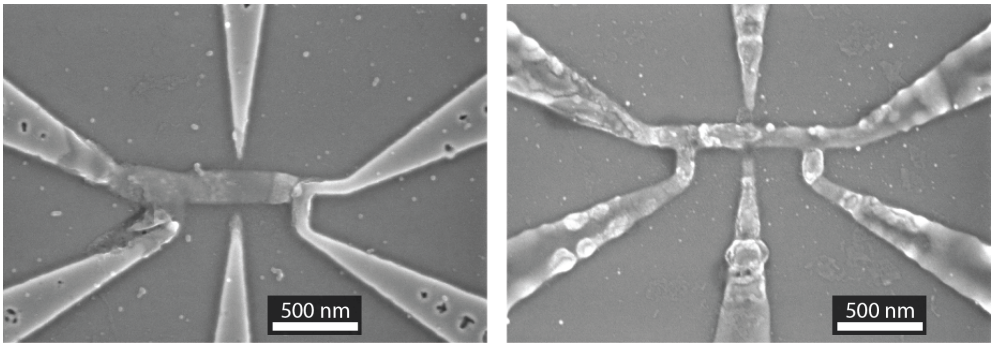

Figure 6.6: Micrographs of nanolines damaged during measurements.

magnetization is lower, the danger to damage the substrate persists. Therefore, the magnetic field applied in the experiments described below was limited to 1 T.

6.4 Electrical transport in nanolines

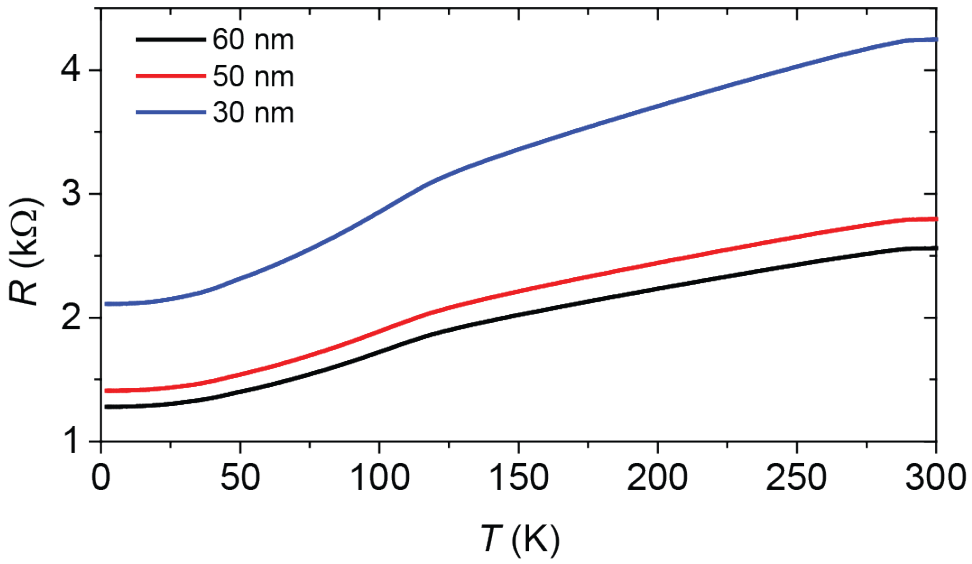

Figure 6.7: Resistance as a function of temperature measured in three $SrRuO_3$ nanolines with widths of 60, 50 and 30 nm and a thickness of 12 nm (sample #205).

Figure 6.7 shows the resistance as a function of temperature measured in three $SrRuO_3$ nanolines with diameters of 60, 50 and 30 nm fabricated on a single sample. The thickness of the initial film was 12 nm. The curves were measured during cooling the sample with a low rate of 1 K/min to reduce the temperature lag of the setup. It can be seen that the temperature dependence has the same

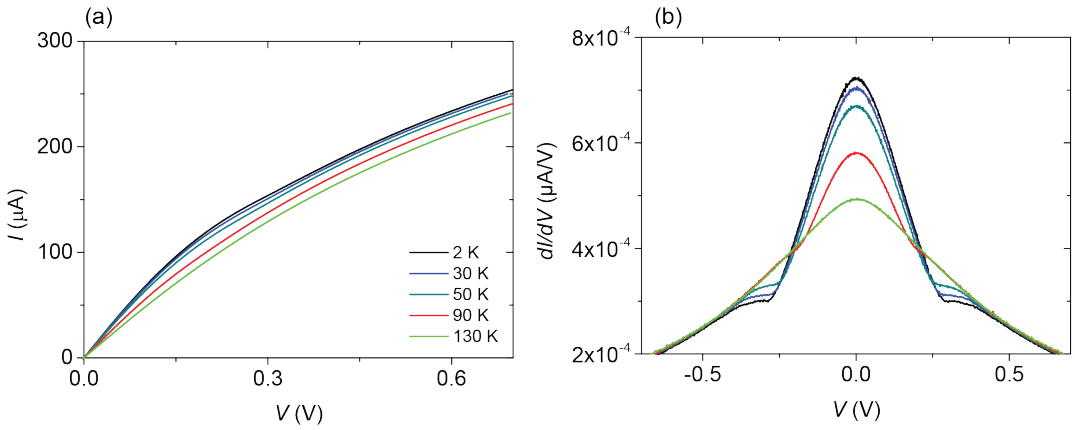

Figure 6.8: (a) $I(V)$ characteristics measured on a 50-nm-width $SrRuO_3$ nanoline at several background temperatures from 2 to 150 K. All characteristics are symmetric relative to zero, only the positive branches are shown. (b) Voltage derivatives of the $I(V)$ curves.

character as that of unpatterned $SrRuO_3$. The Curie temperature in the nanolines as determined from the resistivity anomaly is slightly reduced to $T_C \approx 110\,\mathrm{K}$ compared to $T_C \approx 118\,\mathrm{K}$ in a similar film (Fig. 6.2). The resistance of the nanolines can be compared to the one observed in the thin films. Taking a material thickness $t = 12\,\mathrm{nm}$, a film resistivity $\rho = R_s t = 270\,\mu\Omega{\cdot}\mathrm{cm}$ at room temperature, an effective wire length $l = 600\,\mathrm{nm}$ and considering a rectangular profile of the nanolines, one gets $R_{60nm} = 2.3\,\mathrm{k}\Omega$, $R_{50nm} = 2.7\,\mathrm{k}\Omega$ and $R_{30nm} = 4.5\,\mathrm{k}\Omega$ for the corresponding lines which is close to the measured values. For all the nanolines, $R_{300K}/R_{4K} = 2.0 \pm 0.1$ is in agreement with the thin film value. In magnetic fields up to 1 T, the resistance of the lines shifts insignificantly by $\approx 0.2\%$.

Side gate electrodes of both chosen shapes (bar- and needle-like) did not noticeably influence the transport properties up to the highest achievable voltages applied ($\sim 50-100\,\mathrm{V}$). This is not surprising considering the high $SrRuO_3$ carrier concentration of $n \sim 10^{22}\,\mathrm{cm}^{-3}$.

The $I(V)$ characteristics appear smooth and symmetric. Several $I(V)$ curves measured on a 50-nm-wide nanoline at different background temperatures are shown in Fig. 6.8(a). The lines are robust and can withstand up to $\approx 300\,\mu\mathrm{A}$ and $\approx 1\,\mathrm{V}$. Beyond these values, however, there is a high probability of destroying the device (Fig. 6.6). The actual temperature of the structure can be far above the stated background temperature as the nanolines are heated by the electric current due to their high resistance and a small volume. The heating causes a deviation of the measured $I(V)$ characteristics from the expected linear behavior as the resistance of the material shifts up under the influence of the increasing current.

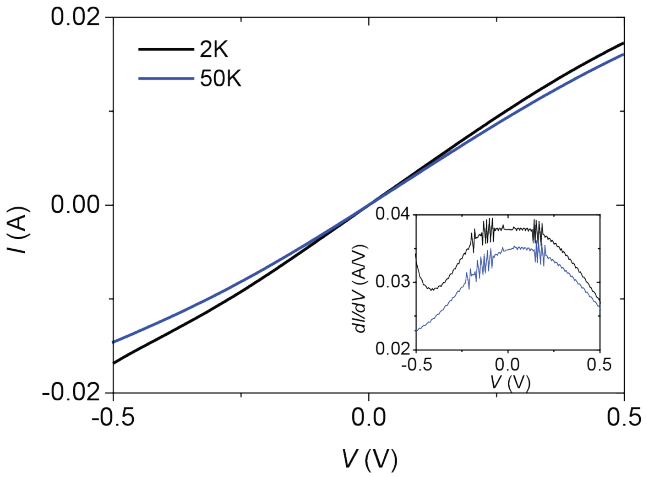

Figure 6.9: $I(V)$ characteristics measured on a 12-nm-thick $SrRuO_3$ film at 2 and 50 K. Voltage derivatives of the $I(V)$ curves are shown in the inset.

An effect of the heating can be noticed by its influence on the temperature of the measurement chamber. For instance, by increasing the current through a nanoline to $\approx 200\,\mu$A the temperature sensor reading is enhanced from the base temperature of 2 K to about 10 K. When measuring thin films, this effect is even larger due to a much larger film volume. The readings in that case may reach $T = 20 - 30$ K. At higher base temperatures (above 10-20 K), the phenomenon becomes less relevant.

Interestingly, the magnetic properties of $SrRuO_3$ are also reflected in the electrical transport. The $dI/dV(V)$ curves shown in Fig. 6.8(b) exhibit anomalies at background temperatures below T_C. Such a behavior is reproducible and was observed in all nanoline samples at approximately the same dissipated power value $P \approx 50\,\mu$W. Because of the different resistances, in thinner lines the features shift to higher voltages. For example, in a 30-nm-wide nanoline the peak of the anomaly is located at $V = 0.38$ V and $I = 125\,\mu$A, whereas in a 60-nm-wide one it is at $V = 0.29$ V and $I = 163\,\mu$A at a background temperature of $T = 2$ K. The described behavior is caused apparently by the heating effects. When the local temperature of the lines exceeds the temperature of the ferromagnetic transition close to $T = 110$ K, it leads to a slight modification of the electronic properties. This finding is also supported by the fact that the deviations disappear when the background temperature is larger than T_C.

Such heating effects are also observed in the thin films. Figure 6.9 shows $I(V)$ curves and their voltage derivatives measured at 2 and 50 K of background temperature in a $5 \times 5\,\text{mm}^2$ thin film of $SrRuO_3$ with a thickness of 12 nm measured by the 4-probe van der Pauw technique. A similar non linearity of the $I(V)$ curves is observed with the difference of a much higher dissipated power due to the larger film volume. Because of the power limitations, T_C was not reached

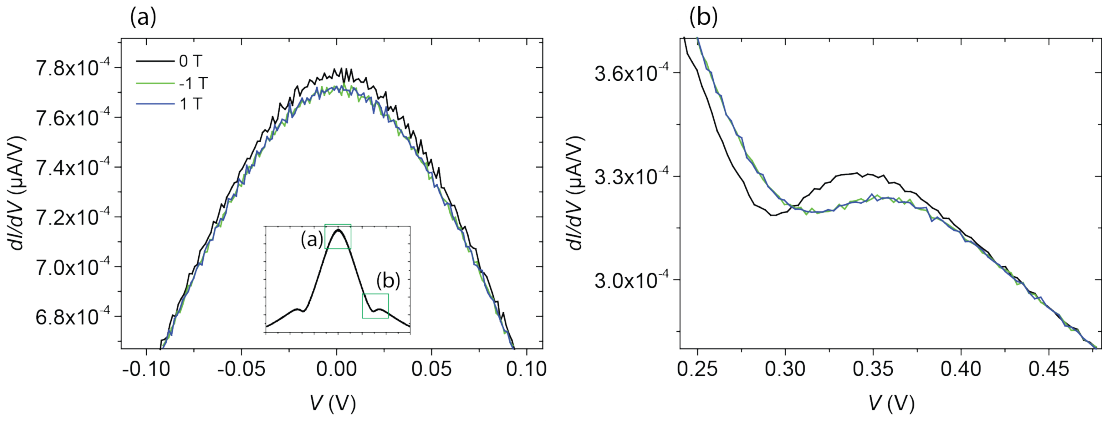

Figure 6.10: Magnetic field dependence of the $dI/dV(V)$ curves measured in a 60-nm-wide nanoline. The inset shows a full-scale curve, (a) and (b) correspond to the zoomed-in regions marked by green rectangles. The influence of the field variation between -1 T and 1 T is shown.

during this measurement. The observed asymmetry of the curves is caused by a larger time necessary to establish thermal equilibrium with the environment.

In an applied magnetic field, the anomaly in $dI/dV(V)$ shifts as is illustrated in Fig. 6.10. Due to the substrate magnetism, only limited magnetic fields of ± 1 T can be to applied without causing a sample damage. In such fields, the anomaly shifts towards higher voltages independent of the field orientation. At the same time, the peak of the dI/dV curve shifts down. The effect is not large and originates apparently from a magnetoresistance of $SrRuO_3$.

In conclusion, we have shown that the developed nanopatterning technology can be used not only for the fabrication of nanodots but for other classes of nanodevices. We demonstrate robust $SrRuO_3$ nanolines with widths as small as 30 nm. The material in the lines preserves the functional properties of $SrRuO_3$ with the same conductivity value that is observed in the corresponding thin films and, additionally, shows behavior which is not achievable in the films. This opens up new possibilities for the fabrication of such devices consisting of complex materials and utilizing their rich functional properties.

Chapter 7

Summary

Nanoscale confinement of materials in one or more dimensions allows for the realization of properties that do not exist in other substances in nature. This makes such objects extremely interesting as systems to study new physical effects and for potential applications in devices. New perspectives in this field arise if one considers using materials with inherently correlated electron systems. Even in bulk, these substances possess rich phase diagrams with a large number of competing ground states. The abundance of the functional properties is expected to enrich the physics of nanoobjects created from such materials. In this work, I utilize the top-down approach to create and study 0D- and 1D-confined nanostructures of correlated ferromagnetic metallic perovskite $SrRuO_3$. A specific emphasis is put on the modification of its magnetic properties upon confinement from the thin film to the nanostructured form.

In Chapter 3, I establish a basis for this research by developing the technology for patterning complex epitaxially-grown heterolayers. Using a combination of electron beam lithography and dry etching with Ar ions I succeeding fabricating nanostructures with sizes of $< 20\,\mathrm{nm}$, which was never achieved before for this class of materials. The top-down approach allows us the creation of nanostructures with arbitrary configurations and shape. At the same time, the stability of the process grants us the possibility to structure large areas containing up to several billions elements per sample.

The second highlight of the chapter is the optimization of growth conditions of $SrRuO_3$ on (100) $SrTiO_3$ to achieve the highest possible material quality while using pulsed laser deposition as a growth technique. We implement a newly developed technology of *in situ* thermal annealing for preparation of the substrate surface before epitaxial growth. The technology allows for a higher quality and better reproducibility of the deposited material compared to the commonly used chemical treatment of substrates.

The properties of both the initial thin film and the nanodots of $SrRuO_3$ are examined in Chapter 4 using various methods. I show that the quality of our thin films is comparable to or even exceeds the best films reported in the literature. After the patterning to nanodots, the material preserves the epitaxial structure and does not develop visible defects or dead layers down to structure sizes of 30 nm. This result is crucial as it proves that epitaxial layers of complex materials can be patterned to such small scales while maintaining structural integrity.

The results of SQUID magnetometry performed on the nanodots are presented in Chapter 5. I show that the magnetic properties of $SrRuO_3$ change in many respects after patterning. One intriguing effect is the enhancement of the Curie temperature of the ferromagnetic transition in the nanodots with sizes smaller than ≈ 200 nm. Although a modification of T_C in nanopatterned structures is not surprising, usually only a decrease is observed which is associated with the reduction of the number of nearest neighbors when one of the dimension of a system approaches several nanometers. In my samples, I see a gradual increase of T_C with shrinking dot size, starting from $T_C = 149 \pm 1$ K in thin films and dots > 200 nm and reaching a maximum of $T_C \approx 157$ K at a dot size of 35-40 nm. To explain such a behavior, we study the structural properties of the nanodots using STEM-based geometric phase analysis. This reveals a reduction of compressive epitaxial strain in small dots. The amount of the relieved strain increases with decreasing dot size and happens at the same length scale as the observed T_C enhancement. Literature data showing a dependence of the magnetism in $SrRuO_3$ on the amount of applied strain confirm this interpretation.

Analyzing the behavior of the nanodots hysteresis loops, I track the evolution of $M(B)$ with reducing structure size. I see that the hysteresis curves start to deviate from the thin film shape at dot sizes of $\approx 10\,\mu$m and smaller. I observe a gradual reduction of the remanence to saturation magnetization ratio from $M_{rem}/M_{sat} = 0.85$ in the thin films to $M_{rem}/M_{sat} = 0.51$ and $M_{rem}/M_{sat} = 0.44$ in 200 and 50 nm dots, respectively, as measured in the out-of-plane oriented magnetic field. This indicates that the magnetic easy axis reorients itself to a different angle. Using the slope of the loops at small fields, I estimate values of the anisotropy field and the anisotropy constant and conclude that they remain within the same order of magnitude after patterning. To describe the behavior of magnetic anisotropy in the dots quantitatively, different experimental approaches have to be used. Also, I discover that with changing periodicity of the dots, a modification of the hysteretic behavior in the region of magnetic fields from ≈ 0 to 2.5 T takes place which implies the effects of an interaction between the dots. From the SQUID measurements alone, it was not possible to determine whether these effects appear due to demagnetizing checkerboard states or to vortex or multidomain states inside the dots.

In addition to the nanodots exploration, I also studied electrical transport in nanowires fabricated of $SrRuO_3$ as described in Chapter 6. For these devices, (110) $DyScO_3$ was used a substrate material to avoid leakage currents caused by the conductivity of $SrTiO_3$ appearing after ion irradiation. I successfully fabricated wires with widths down to 30 nm and a thickness of 12 nm and showed that the material remains conductive and ferromagnetic. $R(T)$ curves measured in a temperature range down to 2 K show the same characteristic features as the corresponding thin films. The wires are robust, sustaining a dissipated power up to $\approx 300\,\mu$W corresponding to a current of $I \approx 300\,\mu$A and a voltage drop of $U \approx 1\,$V. $I(V)$ characteristics are smooth with a nonlinearity caused by the effect of resistive heating. At a dissipated power of $P \approx 50\,\mu$W, a small anomaly is observed in nanowires of all sizes which is well visible in the dI/dV signal. The anomaly apparently occurs when the local temperature of the device exceeds that of the ferromagnetic transition.

The results of this work show that it is possible to utilize a top-down approach and conventional e-beam lithography to pattern epitaxial nanostructures of complex materials with structure sizes of just about 10-20 nm while retaining their functional properties. At the same time, the material structure stays free of major defects and dead layers that deteriorate the nanostructure properties. Using the example of a single material, I demonstrate new interesting features caused by electronic and structural modifications happening upon spatial confinement even in single or weakly interacting nanostructures. This is not to mention their strongly bound ensembles, and in the long term even entire artificial solids composed of such objects. We anticipate many possibilities for the fabrication and exploration of such systems consisting of various combinations of materials from a broad family of substances with correlated electron systems.

Acknowledgment

The four years that I spent doing my PhD project were, most probably, the most exciting time of my life. I would like to express my gratitude to people who made this possible, who supported and guided me, both scientifically and personally.

The first name that should be mentioned in this section is Prof. Dr. Jochen Mannhart to whom I'm deeply grateful for the opportunity to work on such a great topic. Since the first day, his enthusiasm and great attitude were a source of constant support and every time after our meetings the level of my motivation increased by an order of magnitude.

Furthermore, I would like to express my gratitude to Prof. Dr. Martin Dressel for taking a task to be my second supervisor and for reviewing my work.

I thank my day to day supervisor Wolfgang Braun who was always ready to support me in choosing a further direction for my experiments and explaining concepts of RHEED or surface science over and over again.

I am grateful to Hans Boschker who was patiently answering countless questions about $SrRuO_3$ and XRD and paying for my wine at restaurants. I would like to address special thanks to Prof. John Mydosh and Dr. Eberhard Göring for fruitful discussions about magnetism and many insights that helped to better understand my samples.

I appreciate the great collaboration with the Stuttgart Center for Electron Microscopy that has produced a lot of beautiful scientific results. Namely, I would like to thank Prof. Dr. Peter van Aken, Vesna Srot and, especially, Hongguang Wang who not only spent a lot of time cutting and measuring our nanodot samples but also supported me on a personal level by great discussions and friendly attitude.

I greatly appreciate the assistance of the entire nanostructuring facility of the institute who invested a lot of experience and technical support into fabrication of my nanostructures. Namely, I want to thank Jürgen Weis as a head of the facility for providing the infrastructure, solving organizational problems, as well as for being my external supervisor and contributing his thoughts and consideration to the developing of my project; Ulrike Weizmann and Thomas Reindl for providing constant technical support with e-beam lithography and other setups and sharing ideas about fabrication of nanostructures; Marion Hagel for wire bonding the

samples. I also thank the entire departments of Prof. Schütz and Dr. Kremer for providing me access to SQUID setups and granting me a lot of measurement time.

I would like to thank the team of technicians of our department - Wolfgang, Sabine, Ingo, Konrad and Manfred - for the willingness to vent and repair vacuum chambers immediately after they break and a lot of other technical support with the sophisticated equipment that we use. Special thanks to Helga Hoier for performing XRD measurements.

My biggest gratitude I would like to express to the entire MHA-group. Each of you guys always had time for me whenever I popped up with a question and was friendly despite my personality is not always easy-going :) Thanks to Carsten and Pascal for sharing their lithography knowledge, Robin for teaching me how to speak german (and swabian), Prosper for proving that in the end everything will be alright, Jone for helping me to fill helium, Thomas and Wolfgang for correcting parts of my thesis and the paper, Wilson and Alex for teaching me how to be canadian. And to all of you for great times and discussions. Special thanks to people I had a chance to share an office with: Bhagwati for discussions about the future of humanity, Fati for helping me to realize that I'm not the only one who is struggling with writing the thesis, Ali for not being in the office so often. And of course Aggelos for warming up a chair for me. I am grateful for the comprehensive support from Renate Zimmermann, for solving all the organizational questions, proofreading my Zusammenfassung and always having a friendly attitude.

Appendix A

Recipes

In this appendix, I provide detailed recipes for all technological processes used for sample fabrication in this work. This includes substrate termination, PLD growth, e-beam lithography, e-beam evaporation and Ar milling.

A.1 Substrate preparation using buffered HF solution

This method of substrate termination was used only in the first half of this work before the more advanced *in situ* thermal annealing technique was developed. It is provided here as a large fraction of early samples was prepared using this technique. This termination method was applied only to $SrTiO_3$ substrates.

1. Wipe a substrate with a piece of lens paper moistened with isopropanol
2. Ultrasonic cleaning in acetone (10′)
3. Ultrasonic cleaning in isopropanol (10′)
4. Ultrasonic cleaning in ultra pure water (30′)
5. Etching in 87.5% NH_4F - 12.5% HF solution in an ultrasonic bath (30″)
6. Ultrasonic cleaning in ultra pure water (30″)
7. Cleaning in ultra pure water, step 2 (30″)
8. Cleaning in ultra pure water, step 3 (30″)
9. Ultrasonic cleaning in isopropanol (10″)
10. Dry with a nitrogen gun
11. Anneal in a tube furnace in oxygen atmosphere at 1000°C (2 h)
12. Glue the substrate on top of a Haynes block using silver paste
13. Anneal at a hot plate at 100°C (30′)
14. Ready for growth

A.2 Substrate preparation using *in situ* high temperature annealing

This termination technique was used for *in situ* termination of (100) $SrTiO_3$ and (110) $DyScO_3$ substrates.

1. Wipe a substrate with a piece of lens paper moistened with isopropanol
2. Ultrasonic cleaning in acetone (10′)
3. Ultrasonic cleaning in isopropanol (10′)
4. Ultrasonic cleaning in ultra pure water (10′)
5. Anneal in a PLD chamber using direct heating with CO_2 laser:
   - set the pressure in the chamber to 0.08 mbar O_2
   - gradually heat up (1 K/s) to:
   - for $SrTiO_3$ - to 1300°C
   - for $DyScO_3$ - to 1400°C
   - keep at the temperature for 200 s
   - cool to growth temperature (1 K/s)
6. Ready for growth

A.3 Fabrication of nanostructures using CSAR resist

The fabrication technology involves three steps - EBL exposure, Al_2O_3 hard mask deposition and Ar milling. All parameters are optimized for thin films ($\approx 10 - 20\,\text{nm}$) of $SrRuO_3$ grown on $SrTiO_3$ or $DyScO_3$.

1. Ultrasonic cleaning in acetone (3′)
2. Ultrasonic cleaning in isopropanol (3′)
3. Dry with a nitrogen gun
4. Spin-coat a layer of CSAR resist at a rotational speed of 4000 rpm (60″)
5. Anneal at a hot plate at 150°C (60″)
6. Spin-coat a layer of Espacer at a rotational speed of 6000 rpm (35″)
7. Parameters for EBL exposure:
   - Electron beam current - 300 pA
   - Aperture size - 60 μm
   - Exposure dose - 300 $\mu C/cm^2$
8. DI water rinse (15″)
9. Develop in AR-600-546 (60″)
10. Isopropanol rinse (20″)
11. Dry with a nitrogen gun
12. Deposit amorphous Al_2O_3 by PLD (10-15 nm)
13. Lift-off CSAR in AR-300-70 at 65°C and low-power sonication (2 h)
14. Oxygen plasma cleaning to remove CSAR residues (60″)
15. Ar ion milling (250 s)

A.4 Fabrication of nanostructures using PMMA resist

The fabrication technology involves three steps - EBL exposure, Al_2O_3 hard mask deposition and Ar milling. All parameters are optimized for thin films ($\approx 10 - 20\,\text{nm}$) of $SrRuO_3$ grown on $SrTiO_3$ or $DyScO_3$.

1. Ultrasonic cleaning in acetone (3′)
2. Ultrasonic cleaning in isopropanol (3′)
3. Dry with a nitrogen gun
4. Spin-coat a layer of PMMA 200K 3.5% resist at a rotational speed of 6000 rpm (35″)
5. Anneal at a hot plate at 160°C (4′)
6. Spin-coat a layer of PMMA 950K 1.5% resist at a rotational speed of 6000 rpm (35″)
7. Anneal at a hot plate at 160°C (4′)
8. Spin-coat a layer of Espacer at a rotational speed of 6000 rpm (35″)
9. Parameters for EBL exposure:
   - Electron beam current - 300 pA
   - Aperture size - 25 μm
   - Exposure dose - 600 $\mu\text{C/cm}^2$
10. DI water rinse (15″)
11. Develop in MIBK (90″)
12. Isopropanol rinse (20″)
13. Dry with a nitrogen gun
14. Deposit amorphous Al_2O_3 by PLD (10-15 nm)
15. Lift-off CSAR in AR-300-70 at 65°C and low-power sonication (2 h)
16. Oxygen plasma cleaning to remove CSAR residues (60″)
17. Ar ion milling (250 s)

Appendix B

Calculation of the magnetization from SQUID measurements

The script is written on Python and is intended to transform the inductive voltage response in the SQUID flux transformer to the actual sample magnetization. Additionally, it allows to analyze, process and plot the data. The fitting is done to the following equation:

$$\begin{aligned} f(Z) = X_1 + X_2 \cdot Z + X_3 \cdot \{2 \cdot [R^2 + (Z + X_4)^2]^{-3/2} - \\ -[R^2 + (\Lambda + (Z + X_4))^2]^{-3/2} - [R^2 + (-\Lambda + (Z + X_4))^2]^{-3/2}\} \end{aligned} \tag{B.1}$$

where Z is the sample position, R and Λ are the setup defined longitudinal radius and the longitudinal coil separation constants, respectively. The fit parameter X_1 is a constant offset voltage, X_2 takes into account a linear electronic drift during the measurement, X_3 is an amplitude and X_4 is a shift of the sample along the axis of the magnet. The actual magnetization of the sample can be calculated from the voltage amplitude X_3 using the following equation:

$$M = \frac{X_3 \times long.\_regr.\_factor \times RSO\_regr.\_factor}{SQUID\_cal.\_factor \times sensitivity\_factor \times correction\_factor} \tag{B.2}$$

where the *longitudinal regression factor* and the *SQUID calibration factor* are the setup dependent constants. The *correction factor* $= 0.9125$ is the standard correction incorporated into the software. The *sensitivity factor* can be different for every data point. It depends on the sensitivity limit of the detector and can be calculated as a ratio of gain to range settings. The corresponding gain and range codes can be extracted from a *.diag* file. Finally, the *RSO regression factor* is a small correction used for the recirocating sample option. Exact values of the factors can be found in the script below.

The script extracts raw voltages from a *.raw* data file, fits them to Eq. B.1 for every data point measured and determines the value of the magnetization according Eq. B.2.

Pythone code:

```
import numpy as np
import matplotlib as mpl
import matplotlib.pyplot as plt
from scipy.optimize import curve_fit

# function extracting a column i from a 2D list
def column(matrix, i):
    row_float =[]
    row_string = [row[i] for row in matrix]
    for i in row_string:
        row_float.append(float(i))
    return row_float

# separates a list of raw data into sublists by field
def separate_data(matrix,number_of_scans):
    field = matrix[1]
    print(field)

# define a file for data extraction
base_file_name = "Data\pgen-211.film.loop.15K.40000Oe.2meas.outofplane.
    OldSQUID.2" # file name without extensions

data_extension = ".rso.dat" # extension for default fitted data
raw_extension = ".rso.raw" # extension for raw data
diag_extension = ".rso.diag" # extension for diagnostic file, contains
    gain and range settings

data_file_name = base_file_name + data_extension
raw_file_name = base_file_name + raw_extension
diag_file_name = base_file_name + diag_extension

# read a data file and import values
data_file_content = np.loadtxt(data_file_name,delimiter=",",skiprows=31,
    dtype=str)
data_field = column(data_file_content, 2)
data_temperature = column(data_file_content, 3)
data_long_moment = column(data_file_content, 4)

# extract raw data
raw_file_content = np.loadtxt(raw_file_name, delimiter=",", skiprows=31,
    dtype=str)
raw_field = column(raw_file_content, 2)
raw_scan = column(raw_file_content, 5)
raw_position = column(raw_file_content, 7)
raw_voltage = column(raw_file_content, 8)
```

```
raw_data = [raw_field, raw_scan, raw_position, raw_voltage]

# function cuts a big array of raw data into sublists of 64 values each.
# a sublist corresponds to a single data point in .dat file
def separate_data(matrix,number_of_points):

    separate_fields = [matrix[0][x:x+64] for x in range(0, len(matrix[0])
        ,64)]
    separate_scans = [matrix[1][x:x+64] for x in range(0, len(matrix[0])
        ,64)]
    separate_positions = [matrix[2][x:x+64] for x in range(0, len(matrix
        [0]),64)]
    separate_positions = [[x - 2.0 for x in row] for row in
        separate_positions] # subtract 2 cm offset from positions
    separate_voltages = [matrix[3][x:x+64] for x in range(0, len(matrix
        [0]),64)]

    return (separate_fields, separate_scans, separate_positions,
        separate_voltages)

separated_data = separate_data(raw_data,64)

number_scans = max(max(separated_data[1])) #number of measurements
    performed for each data point
number_data_points = len(data_temperature) #total number of final data
    points
number_raw_data_points = number_data_points * number_scans #total number
    of raw data points

# extract lists of gain and range from diag file
diag_file_content = np.loadtxt(diag_file_name, delimiter=",", skiprows=27,
     dtype=str)
squid_range = column(diag_file_content, 24)
squid_gain = column(diag_file_content, 25)

# define SQUID constants and parameters
R = 0.97 # longitudinal radius, setup characteristic
A = 1.519 # longitudinal coil separation
corr_factor = 0.9125 # correction factor, standard for all MPMSs
# Attention! The following values are different for different SQUIDs!
SQUID_cal_factor = 7204.4 # Old SQUID - 7204.4, New SQUID - 8450
long_reg_factor = 1.825 # Old SQUID - 1.825, New SQUID - 1.825
regr_factor = 1.0099 # Old SQUID - 1.0099, New SQUID - 1.0283

#calculate the senditivity calibration factor from range and gain settings
     imported from diag file
range_factor = [10**squid_range[i] for i in range(len(squid_range))]

gain_factor = [None]*len(squid_gain)
for i in range(len(squid_gain)):
    if squid_gain[i] == 0:
```

```
        gain_factor[i] = 1
    elif squid_gain[i] == 1:
        gain_factor[i] = 2
    elif squid_gain[i] == 2:
        gain_factor[i] = 5
    elif squid_gain[i] == 3:
        gain_factor[i] = 10

#sensitivity calibration factor is defined as gain_factor/range_factor
sens_factor = [gain_factor[i]/range_factor[i] for i in range(len(
    gain_factor))]

# function for fitting
def squid_func(X, x1, x2, x3, x4):
    x,y = X # combine two variables into a single one for external access
    R = 0.97 # longitudinal radius, setup characteristic
    A = 1.519 # longitudinal coil separation

    return x1 + x2 * y + x3 * (2 * (R**2 + (x + x4)**2)**(-3.0/2.0) - (R
        **2 + (A + (x + x4))**2)**(-3.0/2.0) \
                               - (R**2 + (-A + (x + x4))**2)**(-3.0/2.0))

# fitting itself
fake_positions = [i for i in range(1,65)] #needed because RSO scan starts
    from the center position
index = 0
def squid_fit(index):
        return curve_fit(squid_func, (separated_data[2][index],
            fake_positions), separated_data[3][index],
                         bounds=([-10,-0.02,-10,-0.01], [10, 0.02, 10,0.01])
                             )

x = []
for index in range(len(separated_data[0])):
    popt, pcov = squid_fit(index)
    fit_coeff = [popt[i] for i in range(len(popt))]
    x.append(fit_coeff)

x1 = column(x,0)
x2 = column(x,1)
x3 = column(x,2) # the amplitudes to be used for the magnetization
    calculation
x4 = column(x,3)

# Recalculate the fitted function one more time for plotting.
fit_values = []
for j in range(len(x1)):
    voltage = []
    position = separated_data[2][j]
    for i in range(64):
        voltage.append(x1[j] + x2[j] * fake_positions[i] + x3[j] * (2 * (R
```

```
            **2 + (position[i] + x4[j])**2)**(-3.0/2.0) \
                                - (R**2 + (A + (position[i] + x4[j]))**2)
                                    **(-3.0/2.0) \
                                - (R**2 + (-A + (position[i] + x4[j]))**2)
                                    **(-3.0/2.0)))
    fit_values.append(voltage)

# calculate actual magnetization from the x3 amplitude
M = [x3[i] * long_reg_factor * regr_factor / (SQUID_cal_factor *
    corr_factor * sens_factor[i]) \
     for i in range(len(x3))]

# for multiple measurements the result is averaged
M_averaged = [sum(M[i:i+int(number_scans)])/number_scans for i in range(0,
    len(M),int(number_scans))]

plt.plot(data_field, M_averaged, color='red')
plt.title("M(B)")
plt.xlabel('B (T)')
plt.ylabel('M (emu)')

plt.ylim(-0.0002,0.0002) # data range for plotting, comment to default
plt.xlim(-10000,10000)

#plot together with the default data for comparison
plt.plot(data_field, data_long_moment, color="black", linestyle='dashed',
    linewidth='1')

fig = plt.gcf()

#subtraction of the diamagnetism and other corrections
diamagnetism = 9.75e-9 #diamagnetic susceptibility
uB_coeff = 21877.02265 #coefficient for translation to units of Bohr
    magneton
M_emu = [M_averaged[i] + diamagnetism * data_field[i] for i in range(len(
    data_field))]
M_uB = [M_emu[i] * uB_coeff for i in range(len(M_emu))]
#M_default = [data_long_moment[i] + diamagnetism * data_field[i] for i in
    range(len(data_field))]

plt.plot(data_field, M_uB, color='red')
plt.title("M(B)")
plt.xlabel('B (T)')
plt.ylabel('M (emu)')
fig = plt.gcf()
```

Bibliography

[1] Zloshchastiev, K. G. Why do we live in a 4D world: Can cosmology, black holes and branes give an answer? *Phys. Lett. B* **638**, 89–93 (2006). URL https://doi.org/10.1016/j.physletb.2006.05.034.

[2] Penney, R. On the dimensionality of the real world. *J. Math. Phys.* **6**, 1607 (1965). URL https://doi.org/10.1063/1.1704700.

[3] Tegmark, M. On the dimensionality of spacetime. *Class. Quantum Grav.* **14**, 69–75 (1997). URL https://doi.org/10.1088/0264-9381/14/4/002.

[4] Evans, B. L. & Young, P. A. Delocalized excitons in thin anisotropic crystals. *Phys. Status Solidi B* **25**, 417–425 (1968). URL https://onlinelibrary.wiley.com/doi/abs/10.1002/pssb.19680250139.

[5] Consadori, F. & Frindt, R. F. Crystal size effects on the exciton absorption spectrum of WSe_2. *Phys. Rev. B* **2**, 4893–4896 (1970). URL https://link.aps.org/doi/10.1103/PhysRevB.2.4893.

[6] Yoffe, A. D. Low-dimensional systems: quantum size effects and electronic properties of semiconductor microcrystallites (zero-dimensional systems) and some quasi-two-dimensional systems. *Adv. Phys.* **42**, 173–262 (1993). URL https://doi.org/10.1080/00018739300101484.

[7] Bibes, M., Villegas, J. E. & Barthelemy, A. Ultrathin oxide films and interfaces for electronics and spintronics. *Adv. Phys.* **60**, 5–84 (2011). URL https://doi.org/10.1080/00018732.2010.534865.

[8] Yoshimatsu, K. *et al.* Metallic quantum well states in artificial structures of strongly correlated oxide. *Science* **333**, 319 (2011). URL https://doi.org/10.1126/science.1205771.

[9] Mannhart, J. & Schlom, D. G. Oxide interfaces - an opportunity for electronics. *Science* **327**, 1607 (2010). URL https://doi.org/10.1126/science.1181862.

[10] Hwang, H. *et al.* Emergent phenomena at oxide interfaces. *Nat. Mater.* **11**, 103–113 (2012). URL https://doi.org/10.1038/nmat3223.

[11] Baiutti, F. *et al.* High-temperature superconductivity in space-charge regions of lanthanum cuprate induced by two-dimensional doping. *Nat. Commun.* **6**, 8586 (2015). URL https://doi.org/10.1038/ncomms9586.

[12] Bern, F. *et al.* Structural, magnetic and electrical properties of $SrRuO_3$ films and $SrRuO_3/SrTiO_3$ superlattices. *J. Phys.: Condens. Matter* **25**, 496003 (2013). URL https://doi.org/10.1088/0953-8984/25/49/496003.

[13] Stanford, M. G., Rack, P. D. & Jariwala, D. Emerging nanofabrication and quantum confinement techniques for 2D materials beyond graphene. *npj 2D Mater. Appl.* **2**, 20 (2018). URL https://doi.org/10.1038/s41699-018-0065-3.

[14] Royo, M., Luca, M. D., Rurali, R. & Zardo, I. A review on III-V core-multishell nanowires: growth, properties, and applications. *J. Phys. D: Appl. Phys.* **50**, 143001 (2017). URL https://doi.org/10.1088/1361-6463/aa5d8e.

[15] Alivisatos, A. P. Semiconductor clusters, nanocrystals, and quantum dots. *Science* **271**, 933–937 (1996). URL http://science.sciencemag.org/content/271/5251/933.

[16] Chakraborty, T. *Quantum dots. A survey of the properties of artificial atoms* (Elsevier, 1999).

[17] Wu, J. *et al.* A metal-free electrocatalyst for carbon dioxide reduction to multi-carbon hydrocarbons and oxygenates. *Nat. Commun.* **7**, 13869 (2016). URL https://doi.org/10.1038/ncomms13869.

[18] Xiu, F. *et al.* Electric-field-controlled ferromagnetism in high-curie-temperature $Mn_{0.05}Ge_{0.95}$ quantum dots. *Nat. Mater.* **9**, 3374 (2010). URL https://doi.org/10.1038/nmat2716.

[19] Samuel, I. Electrifying quantum dots for lasers. *Nat. Mater.* **17**, 9 (2018). URL https://doi.org/10.1038/nmat5040.

[20] Bourzac, K. Quantum dots go on display. *Nature* **493**, 283 (2013). URL https://doi.org/10.1038/493283a.

[21] Morosan, E., Natelson, D., Nevidomskyy, A. H. & Si, Q. Strongly correlated materials. *Adv. Mater.* **24**, 4896–4923 (2012). URL https://onlinelibrary.wiley.com/doi/abs/10.1002/adma.201202018.

[22] Dagotto, E. Complexity in strongly correlated electronic systems. *Science* **309**, 257–262 (2005). URL http://science.sciencemag.org/content/309/5732/257.

[23] Ohtomo, A. & Hwang, H. Y. A high-mobility electron gas at the $LaAlO_3/SrTiO_3$ heterointerface. *Nature* **427**, 423–426 (2004). URL `https://doi.org/10.1038/nature02308`.

[24] Ziese, M. *et al.* Tailoring magnetic interlayer coupling in $La_{0.7}Sr_{0.3}MnO_3/SrRuO_3$ superlattices. *Phys. Rev. Lett.* **104**, 167203 (2010). URL `https://link.aps.org/doi/10.1103/PhysRevLett.104.167203`.

[25] Cheng, G. *et al.* Sketched oxide single-electron transistor. *Nat. Nanotechnol.* **6**, 343 (2011). URL `https://doi.org/10.1038/nnano.2011.56`.

[26] Cen, C. *et al.* Nanoscale control of an interfacial metal–insulator transition at room temperature. *Nat. Mater.* **7**, 298 (2008). URL `https://doi.org/10.1038/nmat2136`.

[27] Zabaleta, J. *et al.* Nanoscale magnetic structure and properties of solution-derived self-assembled $La_3Sr_3MnO_3$ islands. *J. Appl. Phys.* **111**, 024307 (2012). URL `https://doi.org/10.1063/1.3677985`.

[28] Kuiper, B., Blok, J. L., Zandvilet, H. J. W. & Blank, D. H. A. Self-organization of $SrRuO_3$ nanowires on ordered oxide surface terminations. *MRS Commun.* **1**, 1 (2011). URL `https://doi.org/10.1557/mrc.2011.8`.

[29] Ruzmetov, D. *et al.* Epitaxial magnetic perovskite nanostructures. *Adv. Mater.* **17**, 2869–2872 (2005). URL `https://onlinelibrary.wiley.com/doi/abs/10.1002/adma.200501240`.

[30] Roas, B. Patterning of epitaxial $YBa_2Cu_3O_x$ insulator multilayers with a high-temperature-resistant lift-off mask. *Appl. Phys. Lett.* **59**, 2594–2596 (1991). URL `https://doi.org/10.1063/1.105913`.

[31] Banerjee, N., Huijben, M., Koster, G. & Rijnders, G. Direct patterning of functional interfaces in oxide heterostructures. *Appl. Phys. Lett.* **100**, 041601 (2012). URL `https://doi.org/10.1063/1.3679379`.

[32] Koster, G. *et al.* Structure, physical properties, and applications of $SrRuO_3$ thin films. *Rev. Mod. Phys.* **84**, 253–298 (2012). URL `10.1103/RevModPhys.84.253`.

[33] Choi, K. J. *et al.* Phase-transition temperatures of strained single-crystal $SrRuO_3$ thin films. *Adv. Mater.* **22**, 759–762 (2010). URL `https://doi.org/10.1002/adma.200902355`.

[34] Maria, J.-P., McKinstry, H. L. & Trolier-McKinstry, S. Origin of preferential orthorhombic twinning in $SrRuO_3$ epitaxial thin films. *Appl. Phys. Lett.* **76**, 3382 (2000). URL `https://doi.org/10.1063/1.126654`.

[35] Jones, C. W., Battle, P. D., Lightfoot, P. & Harrison, W. T. A. The structure of $SrRuO_3$ by time-of-flight neutron powder diffraction. *Acta Cryst.* **C45**, 365–367 (1989). URL https://doi.org/10.1107/S0108270188012077.

[36] Shin, J. *et al.* Surface stability of epitaxial $SrRuO_3$ films. *Surf. Sci.* **581**, 118–132 (2005). URL https://doi.org/10.1016/j.susc.2005.02.038.

[37] Allen, P. B. *et al.* Transport properties, thermodynamic properties, and electronic structure of $SrRuO_3$. *Phys. Rev. B* **53**, 4393 (1996). URL https://doi.org/10.1103/PhysRevB.53.4393.

[38] Capogna, L. *et al.* Sensitivity to disorder of the metallic state in the ruthenates. *Phys. Rev. Lett.* **88**, 076602 (2002). URL https://doi.org/10.1103/PhysRevLett.88.076602.

[39] Laad, M. S. & Müller-Hartmann, E. Origin of the non-Fermi-liquid behavior of $SrRuO_3$. *Phys. Rev. Lett.* **87**, 246402 (2001). URL https://doi.org/10.1103/PhysRevLett.87.246402.

[40] Timm, C., Raikh, M. E. & von Oppen, F. Disorder-induced resistive anomaly near ferromagnetic phase transition. *Phys. Rev. Lett.* **94**, 036602 (2005). URL https://doi.org/10.1103/PhysRevLett.94.036602.

[41] Shimizu, S. *et al.* Gate tuning of anomalous Hall effect in ferromagnetic metal $SrRuO_3$. *Appl. Phys. Lett.* **105**, 163509 (2014). URL https://doi.org/10.1063/1.4899145.

[42] Klein, L. *et al.* Transport and magnetization in the badly metallic itinerant ferromagnet $SrRuO_3$. *J. Phys.: Condens. Matter* **8**, 10111 (1996). URL https://doi.org/10.1088/0953-8984/8/48/026.

[43] Kostic, P. *et al.* Non-Fermi-liquid behavior of $SrRuO_3$: evidence from infrared conductivity. *Phys. Rev. Lett.* **81**, 2498 (1998). URL https://doi.org/10.1103/PhysRevLett.81.2498.

[44] Singh, D. J. Electronic and magnetic properties of the *4d* itinerant ferromagnet $SrRuO_3$. *J. Appl. Phys.* **79**, 4818 (1996). URL https://doi.org/10.1063/1.361618.

[45] Mazin, I. I. & Singh, D. J. Electronic structure and magnetism in Ru-based perovskites. *Phys. Rev. B* **56**, 2556 (1997). URL https://doi.org/10.1103/PhysRevB.56.2556.

[46] Gutter, A. J., Wong, F. J., Arenholz, E., Vailionis, A. & Suzuki, Y. Evidence of high-spin Ru and universal magnetic anisotropy in $SrRuO_3$ thin films. *Phys. Rev. B* **85**, 134429 (2012). URL https://doi.org/10.1103/PhysRevB.85.134429.

[47] Callaghan, A., Moeller, C. W. & Ward, R. Magnetic interactions in ternary ruthenium oxides. *Inorg. Chem.* **5**, 1572–1576 (1966). URL https://doi.org/10.1021/ic50043a023.

[48] Tian, W. *et al.* Epitaxial growth and magnetic properties of the first five members of the layerd $Sr_{n+1}Ru_nO_{3n+1}$ oxide series. *Appl. Phys. Lett.* **90**, 022507 (2007). URL https://doi.org/10.1063/1.2430941.

[49] Kats, Y., Genish, I., Klein, L., Reiner, J. W. & Beasley, M. R. Large anisotropy in the paramagnetic susceptibility of $SrRuO_3$ films. *Phys. Rev. B* **71**, 100403(R) (2005). URL https://doi.org/10.1103/PhysRevB.71.100403.

[50] Toyota, D. *et al.* Thickness-dependent electronis structure of ultrathin $SrRuO_3$ films studied by in situ photoemission spectroscopy. *Appl. Phys. Lett.* **87**, 162508 (2005). URL https://doi.org/10.1063/1.2108123.

[51] Xia, J., Siemons, W., Koster, G., Beasley, M. & Kapitulnik, A. Critical thickness for itinerant ferromagnetism in ultrathin films of $SrRuO_3$. *Phys. Rev. B* **79**, 140407 (2009). URL https://doi.org/10.1103/PhysRevB.79.140407.

[52] Boschker, H. *et al.* Ferromagnetism and conductivity in atomically thin $SrRuO_3$. *Phys. Rev. X* **9**, 011027 (2019). URL https://link.aps.org/doi/10.1103/PhysRevX.9.011027.

[53] Marshall, A. F. *et al.* Lorentz transmission electron microscope study of ferromagnetic domain walls in $SrRuO_3$: statics, dynamics, and crystal structure correlation. *J. Appl. Phys.* **85**, 4131 (1999). URL https://doi.org/10.1063/1.370322.

[54] Dabrowski, B. *et al.* Reduced ferromagnetic transition temperatures in $SrRu_{1-v}O_3$ perovskites from Ru-site vacancies. *Phys. Rev. B* **70**, 014423 (2004). URL https://doi.org/10.1103/PhysRevB.70.014423.

[55] Kan, D., Aso, R., Kurata, H. & Shimakawa, Y. Thickness-dependent structure–property relationships in strained (110) $SrRuO_3$ thin films. *Adv. Funct. Mater.* **23**, 1129–1136 (2013). URL https://onlinelibrary.wiley.com/doi/abs/10.1002/adfm.201202402.

[56] Zayak, A., Huang, X., Neaton, J. & Rabe, K. M. Manipulating magnetic properties of srruo$_3$ and caruo$_3$ with epitaxial and uniaxial strains. *Phys. Rev. B* **77**, 214410 (2008). URL https://link.aps.org/doi/10.1103/PhysRevB.77.214410.

[57] Lu, W. *et al.* Strain engineering of octahedral rotations and physical properties of $SrRuO_3$ films. *Sci. Rep.* **5**, 10245 (2015). URL https://doi.org/10.1038/srep10245.

[58] Gan, Q., Rao, R., Eom, C., Garrett, J. & Lee, M. Direct measurement of strain effects on magnetic and electrical properties of epitaxial $SrRuO_3$ thin films. *Appl. Phys. Lett.* **72**, 978 (1998). URL https://doi.org/10.1063/1.120603.

[59] Thomas, S. *et al.* Localized control of Curie temperature in perovskite oxide film by capping-layer-induced octahedral distortion. *Phys. Rev. Lett.* **119**, 177203 (2017). URL https://link.aps.org/doi/10.1103/PhysRevLett.119.177203.

[60] Okamoto, J. *et al.* Correlation effects in the electronic structure of $SrRuO_3$. *Phys. Rev. B* **60**, 2281–2285 (1999). URL https://doi.org/10.1103/PhysRevB.60.2281.

[61] López de la Torre, M. A. *et al.* Electron-electron interaction and weak localization effects in badly metallic $SrRuO_3$. *Phys. Rev. B* **63**, 052403 (2001). URL https://doi.org/10.1103/PhysRevB.63.052403.

[62] Herranz, G. *et al.* Enhanced electron-electron correlations in nanometric $SrRuO_3$ epitaxial films. *Phys. Rev. B* **67**, 174423 (2003). URL https://doi.org/10.1103/PhysRevB.67.174423.

[63] Chaudhari, P., Koch, R. H., Laibowitz, R. B., McGuire, T. R. & Gambino, R. J. Critical-current measurements in epitaxial films of $YBa_2Cu_3O_{7-x}$ compound. *Phys. Rev. Lett.* **58**, 2684–2686 (1987). URL https://link.aps.org/doi/10.1103/PhysRevLett.58.2684.

[64] Deak, D. S. Strontium titanate surfaces. *Mater. Sci. Technol.* **23**, 127–136 (2007). URL https://doi.org/10.1179/174328407X154383.

[65] Riste, T., Samuelsen, E. J., Otnes, K. & Feder, J. Critical behaviour of $SrTiO_3$ near the 105 K phase transition. *Solid State Commun.* **9**, 1455–1458 (1971). URL https://doi.org/10.1016/0038-1098(71)90155-4.

[66] Hayward, S. A. & Salje, E. K. H. Cubic-tetragonal phase transition in $SrTiO_3$ revisited: Landau theory and transition mechanism.

Phase Transitions **68**, 501–522 (1998). URL https://doi.org/10.1080/01411599908224530.

[67] Piskunov, S., Heifets, E., Eglitis, R. & Borstel, G. Bulk properties and electronic structure of $SrTiO_3$, $BaTiO_3$, $PbTiO_3$ perovskites: an ab initio HF/DFT study. *Comput. Mater. Sci.* **29**, 165 – 178 (2004). URL http://www.sciencedirect.com/science/article/pii/S0927025603001812.

[68] Astala, R. & Bristowe, P. D. Ab initio study of the oxygen vacancy in $SrTiO_3$. *Modell. Simul. Mater. Sci. Eng.* **9**, 415–422 (2001). URL https://doi.org/10.1088/0965-0393/9/5/306.

[69] De Souza, R. A. Oxygen diffusion in $SrTiO_3$ and related perovskite oxides. *Adv. Funct. Mater.* **25**, 6326–6342 (2015). URL https://onlinelibrary.wiley.com/doi/abs/10.1002/adfm.201500827.

[70] Zhang, Y., Hu, J., Cao, E., Sun, L. & Qin, H. Vacancy induced magnetism in $SrTiO_3$. *J. Magn. Magn. Mater.* **324**, 1770 – 1775 (2012). URL http://www.sciencedirect.com/science/article/pii/S0304885311009218.

[71] Coey, J. M. D., Venkatesan, M. & Stamenov, P. Surface magnetism of strontium titanate. *J. Phys.: Condens. Matter* **28**, 485001 (2016). URL https://doi.org/10.1088/0953-8984/28/48/485001.

[72] González, M. S. M. *et al.* In situ reduction of (100) $SrTiO_3$. *Solid State Sci.* **2**, 519 – 524 (2000). URL http://www.sciencedirect.com/science/article/pii/S1293255800010682.

[73] Adachi, Y., Kohiki, S., Wagatsuma, K. & Oku, M. Changes in the chemical state of monocrystalline $SrTiO_3$ surface by argon ion bombardment. *Appl. Surf. Sci.* **143**, 272 – 276 (1999). URL http://www.sciencedirect.com/science/article/pii/S0169433299000999.

[74] Tan, H. *et al.* Oxygen vacancy enhanced photocatalytic activity of pervoskite $SrTiO_3$. *ACS Appl. Mater. Interfaces* **6**, 19184–19190 (2014). URL https://doi.org/10.1021/am5051907.

[75] Schmidbauer, M., Kwasniewski, A. & Schwarzkopf, J. High-precision absolute lattice parameter determination of $SrTiO_3$, $DyScO_3$ and $NdGaO_3$ single crystals. *Acta Cryst.* **B68**, 8–14 (2012). URL https://doi.org/10.1107/S0108768111046738.

[76] Uecker, R. *et al.* Properties of rare-earth scandate single crytals (Re = Nd - Dy). *J. Cryst. Growth* **310**, 2649–2658 (2008). URL https://doi.org/10.1016/j.jcrysgro.2008.01.019.

[77] Velickov, B., Kahlenberg, V., Bertram, R. & Bernhagen, M. Crystal chemistry of $GdScO_3$, $DyScO_3$, $SmScO_3$ and $NdScO_3$. *Z Kristallogr.* **222**, 466–473 (2007). URL https://doi.org/10.1524/zkri.2007.222.9.466.

[78] Biegalski, M. D. *et al.* Thermal expansion of the new perovskite substrates $DyScO_3$ and $GdScO_3$. *J. Mater. Res.* **20**, 952–958 (2005). URL https://doi.org/10.1557/JMR.2005.0126.

[79] Haeni, J. H. *et al.* Room-temperature ferroelectricity in strained $SrTiO_3$. *Nature* **430**, 758 (2004). URL https://doi.org/10.1038/nature02773.

[80] Derks, C. *et al.* Band-gap variation in $rScO_3$ (r = Pr, Nd, Sm, Eu, Gd, Tb, and Dy): X-ray absorption and O k-edge x-ray emission spectroscopies. *Phys. Rev. B* **86**, 155124 (2012). URL https://doi.org/10.1103/PhysRevB.86.155124.

[81] Zhao, C. *et al.* Ternary rare-earth metal oxide high-k layers on silicon oxide. *Appl. Phys. Lett.* **86**, 132903 (2005). URL https://doi.org/10.1063/1.1886249.

[82] Ke, X. *et al.* Low temperature magnetism in the perovskite substrate $DyScO_3$. *Appl. Phys. Lett.* **94**, 152503 (2009). URL https://doi.org/10.1063/1.3117190.

[83] Himpsel, F. J., Ortega, J. E., Mankey, G. J. & Willis, R. F. Magnetic nanostructures. *Adv. Phys.* **47**, 511–597 (1998). URL https://doi.org/10.1080/000187398243519.

[84] Furdyna, J. K. Diluted magnetic semiconductors. *J. Appl. Phys.* **64**, R29–R64 (1988). URL https://doi.org/10.1063/1.341700.

[85] Dietl, T. A ten-year perspective on dilute magnetic semiconductors and oxides. *Nat. Mater.* **9**, 965–974 (2010). URL https://doi.org/10.1038/nmat2898.

[86] Stoner, E. C. Collective electron ferronmagnetism. *Proc. R. Soc. London, Ser. A* **165**, 372–414 (1938). URL https://royalsocietypublishing.org/doi/abs/10.1098/rspa.1938.0066.

[87] Li, D., Freitag, M., Pearson, J., Qiu, Z. Q. & Bader, S. D. Magnetic phases of ultrathin fe grown on Cu(100) as epitaxial wedges. *Phys. Rev. Lett.* **72**, 3112–3115 (1994). URL https://link.aps.org/doi/10.1103/PhysRevLett.72.3112.

[88] Prinz, G. Metastability in epitaxial magnetic metal films. *J. Magn. Magn. Mater.* **100**, 469 – 480 (1991). URL http://www.sciencedirect.com/science/article/pii/030488539190835X.

[89] Mills, D. L. The ferromagnetism of ultrathin films; from two to three dimensions. *J. Magn. Magn. Mater.* **100**, 515–526 (1991). URL https://doi.org/10.1016/0304-8853(91)90838-2.

[90] Elmers, H. J. *et al.* Submonolayer magnetism of Fe(110) on W(110): Finite width scaling of stripes and percolation between islands. *Phys. Rev. Lett.* **73**, 898–901 (1994). URL https://doi.org/10.1103/PhysRevLett.73.898.

[91] Li, Y. & Baberschke, K. Dimensional crossover in ultrathin Ni(111) films on W(110). *Phys. Rev. Lett.* **68**, 1208–1211 (1992). URL https://doi.org/10.1103/PhysRevLett.68.1208.

[92] Rong, C.-b. *et al.* Size-dependent chemical and magnetic ordering in $L1_0$-FePt nanoparticles. *Adv. Mater.* **18**, 2984–2988 (2006). URL https://onlinelibrary.wiley.com/doi/abs/10.1002/adma.200601904.

[93] Sun, L., Searson, P. C. & Chien, C. L. Finite-size effects in nickel nanowire arrays. *Phys. Rev. B* **61**, R6463–R6466 (2000). URL https://link.aps.org/doi/10.1103/PhysRevB.61.R6463.

[94] Johnson, M. T. Magnetic anisotropy in metallic multilayers. *Rep. Prog. Phys.* **59**, 1409 (1996). URL https://doi.org/10.1088/0034-4885/59/11/002.

[95] Carcia, P. F., Meinhaldt, A. D. & Suna, A. Perpendicular magnetic anisotropy in Pd/Co thin film layered structures. *App. Phys. Lett.* **47**, 178–180 (1985). URL https://doi.org/10.1063/1.96254.

[96] Pappas, D. P. Temperature dependent magnetic surface anisotropy in ultrathin Fe films. *J. Vac. Sci. Technol., B* **14**, 3203 (1996). URL https://doi.org/10.1116/1.588808.

[97] Engel, B. N., England, C. D., Van Leeuwen, R. A., Wiedmann, M. H. & Falco, C. M. Interface magnetic anisotropy in epitaxial superlattices. *Phys. Rev. Lett.* **67**, 1910–1913 (1991). URL https://doi.org/10.1103/PhysRevLett.67.1910.

[98] Tkachenko, V. S., Kuchko, A. N. & Kruglyak, V. V. An effect of the curvature induced anisotropy on the spectrum of spin waves in a curved

magnetic nanowire. *Low Temp. Phys.* **39**, 163–166 (2013). URL https://doi.org/10.1063/1.4792133.

[99] Varón, M. *et al.* Longitudinal domain wall formation in elongated assemblies of ferromagnetic nanoparticles. *Sci. Rep.* **5**, 14536 (2015). URL https://doi.org/10.1038/srep14536.

[100] Fert, A. & Piraux, L. Magnetic nanowires. *J. Magn. Magn. Mater.* **200**, 338 – 358 (1999). URL http://www.sciencedirect.com/science/article/pii/S0304885399003753.

[101] Stano, M. & Fruchart, O. Magnetic nanowires and nanotubes. *arXiv e-prints* arXiv:1808.04656 (2018). 1808.04656.

[102] Leslie-Pelecky, D. L. & Rieke, R. D. Magnetic properties of nanostructured materials. *Chem. Mater.* **8**, 1770–1783 (1996). URL https://doi.org/10.1021/cm960077f.

[103] Martin, J. I., Nogues, J., Liu, K., Vicent, J. L. & Schuller, I. K. Ordered magnetic nanostructures: fabrication and properties. *J. Magn. Magn. Mater.* **256**, 449–501 (2003). URL https://doi.org/10.1016/S0304-8853(02)00898-3.

[104] Krishnan, K. M. *et al.* Nanomagnetism and spin electronics: materials, microstructure and novel properties. *J. Mater. Sci.* **41**, 793–815 (2006). URL https://doi.org/10.1007/s10853-006-6564-1.

[105] Neel, L. Théorie du traînage magnétique des substances massives dans le domaine de Rayleigh. *J. Phys. Radium,* **11**, 49–61 (1950). URL https://doi.org/10.1051/jphysrad:0195000110204900.

[106] Kechrakos, D. & Trohidou, K. N. Magnetic properties of dipolar interacting single-domain particles. *Phys. Rev. B* **58**, 12169–12177 (1998). URL https://doi.org/10.1103/PhysRevB.58.12169.

[107] Yellen, B., Friedman, G. & Feinerman, A. Analysis of interactions for magnetic particles assembling on magnetic templates. *J. App. Phys.* **91**, 8552–8554 (2002). URL https://doi.org/10.1063/1.1453951.

[108] García-Otero, J., Porto, M., Rivas, J. & Bunde, A. Influence of dipolar interaction on magnetic properties of ultrafine ferromagnetic particles. *Phys. Rev. Lett.* **84**, 167–170 (2000). URL https://doi.org/10.1103/PhysRevLett.84.167.

[109] Guslienko, K. Y., Novosad, V., Otani, Y., Shima, H. & Fukamichi, K. Magnetization reversal due to vortex nucleation, displacement, and annihilation in submicron ferromagnetic dot arrays. *Phys. Rev. B* **65**, 024414 (2001). URL https://link.aps.org/doi/10.1103/PhysRevB.65.024414.

[110] Fernandez, A., Bedrossian, P. J., Baker, S. L., Vernon, S. P. & Kania, D. R. Magnetic force microscopy of single-domain cobalt dots patterned using interference lithography. *IEEE Trans. Magn.* **32**, 4472–4474 (1996). URL https://link.aps.org/doi/10.1109/20.538901.

[111] Sommerfeld, A. Zur Elektronentheorie der Metalle auf Grund der Fermischen Statistik. *Zeitschrift für Physik* **47**, 1–32 (1928). URL https://doi.org/10.1007/BF01391052.

[112] Wigner, E. On the interaction of electrons in metals. *Phys. Rev.* **46**, 1002–1011 (1934). URL https://link.aps.org/doi/10.1103/PhysRev.46.1002.

[113] Hubbard, J. & Flowers, B. H. Electron correlations in narrow energy bands. *Proc. R. Soc. London, Ser. A* **276**, 238–257 (1963). URL https://royalsocietypublishing.org/doi/abs/10.1098/rspa.1963.0204.

[114] Mannhart, J., Boschker, H., Kopp, T. & Valenti, R. Artificial atoms based on correlated materials. *Rep. Prog. Phys.* **79**, 084508 (2016). URL https://doi.org/10.1088/0034-4885/79/8/084508.

[115] Keimer, B., Kivelson, S. A., Norman, M. R., Uchida, S. & Zaanen, J. From quantum matter to high-temperature superconductivity in copper oxides. *Nature* **518**, 179 (2015). URL https://doi.org/10.1038/nature14165.

[116] Mott, N. F. Metal-insulator transition. *Rev. Mod. Phys.* **40**, 677–683 (1968). URL https://link.aps.org/doi/10.1103/RevModPhys.40.677.

[117] Imada, M., Fujimori, A. & Tokura, Y. Metal-insulator transitions. *Rev. Mod. Phys.* **70**, 1039–1263 (1998). URL https://link.aps.org/doi/10.1103/RevModPhys.70.1039.

[118] Dagotto, E. Complexity in strongly correlated electronic systems. *Science* **309**, 257–262 (2005). URL http://science.sciencemag.org/content/309/5732/257.

[119] Bloch, F. Über die Quantenmechanik der Elektronen in Kristallgittern. *Zeitschrift für Physik* **52**, 555–600 (1929). URL https://doi.org/10.1007/BF01339455.

[120] Mimura, T., Hiyamizu, S., Fujii, T. & Nanbu, K. A new field-effect transistor with selectively doped GaAs/n-$Al_xGa_{1-x}As$ heterojunctions. *Jpn. J. Appl. Phys.* **19**, L225–L227 (1980). URL https://doi.org/10.1143/jjap.19.l225.

[121] Das Sarma, S., Adam, S., Hwang, E. H. & Rossi, E. Electronic transport in two-dimensional graphene. *Rev. Mod. Phys.* **83**, 407–470 (2011). URL https://link.aps.org/doi/10.1103/RevModPhys.83.407.

[122] Ganatra, R. & Zhang, Q. Few-layer MoS_2: A promising layered semiconductor. *ACS Nano* **8**, 4074–4099 (2014). URL https://doi.org/10.1021/nn405938z.

[123] Davies, J. H. *Quantum well and low-dimensional systems.The Physics of Low-dimensional Semiconductors: An Introduction*, 118–149 (Cambridge University Press, 1997). URL https://doi.org/10.1017/CBO9780511819070.006.

[124] Ando, T., Fowler, A. B. & Stern, F. Electronic properties of two-dimensional systems. *Rev. Mod. Phys.* **54**, 437–672 (1982). URL https://link.aps.org/doi/10.1103/RevModPhys.54.437.

[125] Schmidt, V., Wittemann, J. V., Senz, S. & Gösele, U. Silicon nanowires: A review on aspects of their growth and their electrical properties. *Adv. Mater.* **21**, 2681–2702 (2009). URL https://onlinelibrary.wiley.com/doi/abs/10.1002/adma.200803754.

[126] Shankar, K. S. & Raychaudhuri, A. Fabrication of nanowires of multicomponent oxides: Review of recent advances. *Mater. Sci. Eng., C* **25**, 738 – 751 (2005). URL http://www.sciencedirect.com/science/article/pii/S0928493105001542.

[127] Royo, M., Luca, M. D., Rurali, R. & Zardo, I. A review on III–V core–multishell nanowires: growth, properties, and applications. *J. Phys. D: Appl. Phys.* **50**, 143001 (2017). URL https://doi.org/10.1088/1361-6463/aa5d8e.

[128] Hyun, J. K., Zhang, S. & Lauhon, L. J. Nanowire heterostructures. *Annu. Rev. Mater. Res.* **43**, 451–479 (2013). URL https://doi.org/10.1146/annurev-matsci-071312-121659.

[129] Eletskii, A. V. Transport properties of carbon nanotubes. *Phys. Usp.* **52**, 209–224 (2009). URL https://doi.org/10.3367/ufne.0179.200903a.0225.

[130] Ashoori, R. Electrons in artificial atoms. *Nature* **379**, 413 (1996). URL https://doi.org/10.1038/379413a0.

[131] Ekimov, A., Efros, A. & Onushchenko, A. Quantum size effect in semiconductor microcrystals. *Solid State Commun.* **56**, 921 – 924 (1985). URL http://www.sciencedirect.com/science/article/pii/S0038109885800259.

[132] Buluta, I., Ashhab, S. & Nori, F. Natural and artificial atoms for quantum computation. *Rep. Prog. Phys.* **74**, 104401 (2011). URL https://doi.org/10.1088/0034-4885/74/10/104401.

[133] Nurmikko, A. What future for quantum dot-based light emitters? *Nat. Nanotechnol.* **10**, 1001 (2015). URL https://doi.org/10.1038/nnano.2015.288.

[134] Laskin, G. *et al.* Magnetic properties of epitaxially grown $SrRuO_3$ nanodots. *Nano Lett.* **19**, 1131–1135 (2019). URL https://doi.org/10.1021/acs.nanolett.8b04459.

[135] Cheng, G. *et al.* Sketched oxide single-electron transistor. *Nat. Nanotechnol.* **6**, 343–347 (2011). URL https://doi.org/10.1038/nnano.2011.56.

[136] Jäger, M., Teker, A., Mannhart, J. & Braun, W. Independence of surface morphology and reconstruction during the thermal preparation of perovskite oxide surfaces. *Appl. Phys. Lett.* **112**, 116601 (2018). URL https://doi.org/10.1063/1.5023318.

[137] CrysTec GmbH, specialist in crystal processing. http://www.crystec.de/crystec-e.html. Accessed: 2018-10-25.

[138] Shinkosha, crystals for a bright future. http://www.shinkosha.com/english/index.html. Accessed: 2018-10-25.

[139] Kawasaki, M. *et al.* Atomic control of the $SrTiO_3$ crystal surface. *Science* **266**, 1540–1542 (1994). URL https://doi.org/10.1126/science.266.5190.1540.

[140] Koster, G., Kropman, B. L., Rijnders, G. J. H. M., Blank, D. H. A. & Rogalla, H. H. Quasi-ideal strontium titanate crystal surfaces through formation of strontium hydroxide. *Appl. Phys. Lett.* **73**, 2920–2922 (1998). URL https://doi.org/10.1063/1.122630.

[141] Spindler, H. L., Gilgenbach, R. M. & Lash, J. S. Effects of laser-ablation target damage on particulate production investigated by laser scattering

with deposited thin film and target analysis. *Appl. Phys. Lett.* **68**, 3245 (1996). URL https://doi.org/10.1063/1.116562.

[142] Christen, H. M. & Eres, G. Recent advances in pulsed-laser deposition of complex oxides. *J. Phys.: Condens. Matter* **20** (2008). URL https://doi.org/10.1088/0953-8984/20/26/264005.

[143] Willmott, P. R. & Huber, J. R. Pulsed laser vaporization and deposition. *Rev. Mod. Phys.* **72** (2000). URL https://doi.org/10.1103/RevModPhys.72.315.

[144] Smith, H. M. & Turner, A. F. Vacuum deposited thin films using a ruby laser. *Appl. Opt.* **4**, 1 (1965). URL https://doi.org/10.1364/AO.4.000147.

[145] Inam, A. *et al.* As-deposited high T_C and J_C superconducting thin films made at low temperatures. *Appl. Phys. Lett.* **53**, 10 (1988). URL https://doi.org/10.1063/1.100155.

[146] Eason, R. *Pulsed laser deposition of thin films. Application-led growth of functional materials* (Wiley-Interscience. A John Wiley and Sons, Inc., 2007).

[147] Nishikawa, S. & Kikuchi, S. Diffraction of cathode rays by calcite. *Nature* **122**, 726 (1928). URL https://doi.org/10.1038/1211019a0.

[148] Harris, J. J., Joyce, B. A. & Dobson, P. J. Oscillations in the surface structure of Sn-doped GaAs during growth by MBE. *Surf. Sci.* **103**, 90–96 (1981). URL https://doi.org/10.1016/0039-6028(81)90091-1.

[149] Germer, L. H. Electron diffraction experiments upon crystals of galena. *Phys. Rev.* **50**, 659–671 (1936). URL https://doi.org/10.1103/PhysRev.50.659.

[150] Itaka, I., Miyake, S. & Iimori, T. Examination of passive iron by electron diffraction. *Nature* **139**, 156 (1937). URL https://doi.org/10.1038/139156a0.

[151] Hove, J. M. V. & Cohen, P. I. Reflection high energy electron diffraction measurement of surface diffusion during the growth of gallium arsenide by MBE. *J. Cryst. Growth* **81**, 13–18 (1987). URL https://doi.org/10.1016/0022-0248(87)90357-5.

[152] Joyce, B. A. *et al.* RHEED studies of heterojunction and quantum well formation during MBE growth — from multiple scattering to band offsets. *Surf. Sci.* **168**, 423–438 (1986). URL https://doi.org/10.1016/0039-6028(86)90873-3.

[153] Bauer, E. & van der Merwe, J. H. Structure and growth of crystalline superlattices: From monolayer to superlattice. *Phys. Rev. B* **33**, 3657–3671 (1986). URL https://doi.org/10.1103/PhysRevB.33.3657.

[154] Van Der Merwe, J. H. Theoretical considerations in growing uniform epilayers. *Interface Sci.* **1**, 77–86 (1993). URL https://doi.org/10.1007/BF00203267.

[155] Hong, W. *et al.* Persistent step-flow growth of strained films on vicinal substrates. *Phys. Rev. Lett.* **95**, 095501 (2005). URL https://doi.org/10.1103/PhysRevLett.95.095501.

[156] Choi, J., Eom, C.-B., Rijnders, G., Rogala, H. & Blank, D. H. A. Growth mode transition from layer by layer to step flow during the growth of heteroepitaxial $SrRuO_3$ on (001) $SrTiO_3$. *Appl. Phys. Lett.* **79**, 1447–1449 (2001). URL https://doi.org/10.1063/1.1389837.

[157] Rijnders, G., Blank, D. H. A., Choi, J. & Eom, C.-B. Enhanced surface diffusion through termination conversion during epitaxial $SrRuO_3$ growth. *Appl. Phys. Lett.* **84**, 505–507 (2004). URL https://doi.org/10.1063/1.1640472.

[158] Zhou, Z. J. *Electron Beam Lithography*, 287–321 (Springer US, Boston, MA, 2005). URL https://doi.org/10.1007/1-4020-8006-9_10.

[159] Hawkes, P. W. & Spence, J. C. *Science of Microscopy* (Springer Science + Business Media, LLC, 2007).

[160] Broers, A. N. Resolution limits of PMMA resist for exposure with 50 kV electrons. *J. Electrochem. Soc.* **128**, 166–170 (1981). URL http://jes.ecsdl.org/content/128/1/166.abstract.

[161] Jeol JBX-6300FS. Electron beam lithography system. https://www.jeol.co.jp/en/products/detail/JBX-6300FS.html. Accessed: 2019-03-19.

[162] Allresist GmbH, PMMA (AR-P 630-670). http://www.allresist.com/ebeamresists-ar-p-631-679/. Accessed: 2018-10-30.

[163] Allresist GmbH, CSAR 62 (AR-P 6200). http://www.allresist.com/csar-62-ar-p-6200/. Accessed: 2018-10-30.

[164] Showa Denko. Espacer, Electrification Dissipating Material. http://www.showadenko.us/products/espacer/. Accessed: 2018-10-30.

[165] Kaufman, H. R. & Robinson, R. S. Ion source design for industrial applications. *AIAA Journal* **20(6)**, 745–760 (1982). URL https://doi.org/10.2514/3.51131.

[166] Cypher S AFM. Asylum Research, Oxford Instruments. https://afm.oxinst.com/products/cypher-afm-systems/cypher-s-afm. Accessed: 2018-11-06.

[167] Grebinskij, S. *et al.* Electronic structure of epitaxial $SrRuO_3$ films studied by resonant photoemission. *Radiat. Phys. Chem.* **80**, 1140–1144 (2011). URL https://doi.org/10.1016/j.radphyschem.2011.02.012.

[168] Estève, D., Maroutian, T., Pillard, V. & Lecoeur, P. Step velocity tuning of $SrRuO_3$ step flow growth on $SrTiO_3$. *Phys. Rev. B* **83**, 193401 (2011). URL https://link.aps.org/doi/10.1103/PhysRevB.83.193401.

[169] Rao, R. A., Gan, Q. & Eom, C. B. Growth mechanisms of epitaxial metallic oxide $SrRuO_3$ thin films studied by scanning tunneling microscopy. *Appl. Phys. Lett.* **71**, 1171 (1997). URL https://doi.org/10.1063/1.119616.

[170] Robinson, I. K. Crystal truncation rods and surface roughness. *Phys. Rev. B* **33**, 3830–3836 (1986). URL https://link.aps.org/doi/10.1103/PhysRevB.33.3830.

[171] Vailionis, A. *et al.* Misfit strain accommodation in epitaxial ABO_3 perovskites: Lattice rotations and lattice modulations. *Phys. Rev. B* **83**, 064101 (2011). URL https://link.aps.org/doi/10.1103/PhysRevB.83.064101.

[172] Klein, L. *et al.* Anomalous spin scattering effects in the badly metallic itinerant ferromagnet $SrRuO_3$. *Phys. Rev. Lett.* **77**, 2774 (1996). URL https://doi.org/10.1103/PhysRevLett.77.2774.

[173] van der Pauw, L. J. A method of measuring specific resistivity and Hall effect of discs of arbitrary shape. *Philips Res. Repts* **13**, 1–9 (1958).

[174] Fisher, M. E. & Langer, J. S. Resistive anomalies at magnetic critical points. *Phys. Rev. Lett.* **20**, 665 (1968). URL https://doi.org/10.1103/PhysRevLett.20.665.

[175] Alexander, S. & nad I. Balberg, J. S. H. Critical behavior of the electrical resistivity in magnetic systems. *Phys. Rev. B* **13**, 304 (1976). URL https://doi.org/10.1103/PhysRevB.13.304.

[176] Capogna, L. *et al.* Sensitivity to disorder of the metallic state in the ruthenates. *Phys. Rev. Lett.* **88**, 076602 (2002). URL https://doi.org/10.1103/PhysRevLett.88.076602.

[177] Herranz, G. *et al.* Weak localization effects in some metallic perovskites. *Eur. Phys. J. B* **40**, 439–444 (2004). URL https://doi.org/10.1140/epjb/e2004-00207-9.

[178] Nair, H. P. *et al.* Synthesis science of $SrRuO_3$ and $CaRuO_3$ epitaxial films with high residual resistivity ratios. *APL Materials* **6**, 046101 (2018). URL https://doi.org/10.1063/1.5023477.

[179] Max Planck Institute for Solid State Research. Stuttgart Center for Electron Microscopy (StEM). https://www.fkf.mpg.de/StEM. Accessed: 2019-03-08.

[180] Egoavil, R. *et al.* Atomic scale investigation of a $PbTiO_3/SrRuO_3/DyScO_3$ heterostructure. *Appl. Phys. Lett.* **102**, 223106 (2013). URL https://doi.org/10.1063/1.4809597.

[181] Choi, K. J. *et al.* Phase-transition temperatures of strained single-crystal $SrRuO_3$ thin films. *Adv. Mater.* **22**, 759–762 (2010). URL https://onlinelibrary.wiley.com/doi/abs/10.1002/adma.200902355.

[182] Fagaly, R. L. Superconducting quantum interference device instruments and applications. *Rev. Sci. Instrum.* **77**, 101101 (2006). URL https://doi.org/10.1063/1.2354545.

[183] Foner, S. Versatile and sensitive vibrating-sample magnetometer. *Rev. Sci. Instrum.* **30**, 548–557 (1959). URL https://doi.org/10.1063/1.1716679.

[184] Quantum Design. Magnetic Property Measurement System. https://www.qdusa.com/sitedocs/productBrochures/1014-003.pdf. Accessed: 2019-02-08.

[185] Meredith, D. J., Pickett, G. R. & Symko, O. G. Application of a SQUID magnetometer to NMR at low temperatures. *J. Low Temp. Phys.* **13**, 607–615 (1973). URL https://doi.org/10.1007/BF00656548.

[186] Kumar, S., Thorson, B. D. & Avrin, W. F. Broadband SQUID NMR with room-temperature samples. *J. Magn. Reson., Ser. B* **107**, 252 – 259 (1995). URL http://www.sciencedirect.com/science/article/pii/S1064186685710850.

[187] Chieh, J. J. *et al.* In vivo and real-time measurement of magnetic nanoparticles distribution in animals by scanning SQUID biosusceptometry for biomedicine study. *IEEE Trans. Biomed. Eng.* **58**, 2719–2724 (2011). URL https://doi.org/10.1109/TBME.2010.2090042.

[188] Everitt, C. W. F. *et al.* Gravity probe B: Final results of a space experiment to test general relativity. *Phys. Rev. Lett.* **106**, 221101 (2011). URL https://link.aps.org/doi/10.1103/PhysRevLett.106.221101.

[189] McElfresh, M. *Fundamentals of magnetism and magnetic measurements. Featuring Quantum Design's Magnetic Property Measurement System* (Quantum Design, 1994).

[190] Sawicki, M., Stefanowicz, W. & Ney, A. Sensitive SQUID magnetometry for studying nano-magnetism. *Semicond. Sci. Technol.* **26**, 064006 (2011). URL https://doi.org/10.1088/0268-1242/26/6/064006.

[191] du Tremolet de Lacheisserie, E., Gignoux, D. & Schlenker, M. (eds.). *Magnetism. Materials and Applications*, 242–249 (Springer US, 2005). URL https://www.springer.com/de/book/9780387230009#aboutBook.

[192] Stamenov, P. & Coey, J. M. D. Sample size, position, and structure effects on magnetization measurements using second-order gradiometer pickup coils. *Rev. Sci. Instrum.* **77**, 015106 (2006). URL https://doi.org/10.1063/1.2149190.

[193] MPMS application note 1014-213. Subtracting the sample holder background from dilute samples. https://www.qdusa.com/sitedocs/appNotes/mpms/1014-213.pdf. Accessed: 2019-04-16.

[194] Quantum Design. Application note 1500-018. Using straw sample holder with DC scan mode. https://www.qdusa.com/sitedocs/appNotes/mpms_3/1500-018.pdf. Accessed: 2019-01-31.

[195] Fabian, K., Shcherbakov, V. P. & McEnroe, S. A. Measuring the Curie temperature. *Geochem. Geophys. Geosyst.* **14**, 947–961 (2013). URL https://doi.org/10.1029/2012GC004440.

[196] Domb, C., Sykes, M. F. & Randall, J. T. On the susceptibility of a ferromagnetic above the Curie point. *Proc. R. Soc. London, Ser. A* **240**, 214–228 (1957). URL https://doi.org/10.1098/rspa.1957.0078.

[197] Bovensiepen, U., Poulopoulos, P., Farle, M. & Baberschke, K. The Curie temperature in ultrathin Ni/Cu(001) films determined by ac susceptibility

and MOKE. *Surf. Sci.* **402-404**, 396 – 400 (1998). URL https://doi.org/10.1016/S0039-6028(97)01102-3.

[198] Molegraaf, H. J. A. *et al.* Magnetoelectric effects in complex oxides with competing ground states. *Adv. Mater.* **21**, 3470–3474 (2009). URL https://doi.org/10.1002/adma.200900278.

[199] Ade-Hall, J. M., Smith, P. J. & Wilson, R. L. The Petrology, Curie Points and Natural Magnetizations of Basic Lavas. *Geophys. J. Int.* **9**, 323–336 (1965). URL https://doi.org/10.1111/j.1365-246X.1965.tb03890.x.

[200] Lagroix, F., Banerjee, S. K. & Moskowitz, B. M. Revisiting the mechanism of reversed thermoremanent magnetization based on observations from synthetic ferrian ilmenite (y = 0.7). *J. Geophys. Res. B: Solid Earth* **109** (2004). URL https://doi.org/10.1029/2004JB003076.

[201] Cheng, J.-G., Zhou, J.-S., Goodenough, J. B. & Jin, C.-Q. Critical behavior of ferromagnetic perovskite ruthenates. *Phys. Rev. B* **85**, 184430 (2012). URL https://doi.org/10.1103/PhysRevB.85.184430.

[202] Boschker, H. *et al.* Preventing the reconstruction of the polar discontinuity at oxide heterointerfaces. *Adv. Funct. Mater.* **22**, 2235–2240 (2012). URL https://doi.org/10.1002/adfm.201102763.

[203] Moskowitz, B. M. Methods for estimating Curie temperatures of titanomaghemites from experimental $J_s - T$ data. *Earth Planet. Sci. Lett.* **53**, 84 – 88 (1981). URL http://www.sciencedirect.com/science/article/pii/0012821X81900285.

[204] Blundell, S. *Magnetism in condensed matter* (Oxford University Press, 2001).

[205] Khalid, M. *et al.* Ubiquity of ferromagnetic signals in common diamagnetic oxide crystals. *Phys. Rev. B* **81**, 214414 (2010). URL https://link.aps.org/doi/10.1103/PhysRevB.81.214414.

[206] Frederikse, H. P. R. & Candela, G. A. Magnetic susceptibility of insulating and semiconducting strontium titanate. *Phys. Rev.* **147**, 583–584 (1966). URL https://link.aps.org/doi/10.1103/PhysRev.147.583.

[207] Freiman, Y. & Jodl, H. Solid oxygen. *Phys. Rep.* **401**, 1 – 228 (2004). URL http://www.sciencedirect.com/science/article/pii/S037015730400273X.

[208] Nomura, T., Matsuda, Y. H. & Kobayashi, T. C. $H-T$ phase diagram of solid oxygen. *Phys. Rev. B* **96**, 054439 (2017). URL https://link.aps.org/doi/10.1103/PhysRevB.96.054439.

[209] Quantum Design. Application note 1014-210. Oxygen contamintaion. https://www.qdusa.com/sitedocs/appNotes/mpms/1014-210.pdf. Accessed: 2019-02-08.

[210] Hensling, F. V. E. *et al.* UV radiation enhanced oxygen vacancy formation caused by the PLD plasma plume. *Sci. Rep.* **8**, 8846 (2018). URL https://doi.org/10.1038/s41598-018-27207-5.

[211] Norton, D. P., Park, C., Budai, J. D., Pennycook, S. J. & Prouteau, C. Plume-induced stress in pulsed-laser deposited CeO_2 films. *Appl. Phys. Lett.* **74**, 2134–2136 (1999). URL https://doi.org/10.1063/1.123780.

[212] Joy, P. & Date, S. Comparison of the zero-field-cooled magnetization behavior of some ferromagnetic and ferrimagnetic systems. *J. Magn. Magn. Mater.* **218**, 229 – 237 (2000). URL http://www.sciencedirect.com/science/article/pii/S0304885300004054.

[213] Timm, R., Willmott, P. R. & Huber, J. R. Ablation and blow-off characteristics at 248 nm of Al, Sn and Ti targets used for thin film pulsed laser deposition. *J. Appl. Phys.* **80**, 1794–1802 (1996). URL https://doi.org/10.1063/1.362990. https://doi.org/10.1063/1.362990.

[214] Chan, N.-H., Sharma, R. K. & Smyth, D. M. Nonstoischiometry in $SrTiO_3$. *J. Electrochem. Soc.* **128**, 1762–1769 (1981). URL https://doi.org/10.1149/1.2127727.

[215] Potzger, K. *et al.* Defect-induced ferromagnetism in crystalline $SrTiO_3$. *J. Magn. Magn. Mater.* **323**, 1551 – 1562 (2011). URL http://www.sciencedirect.com/science/article/pii/S0304885311000308.

[216] Lagendijk, A., Glasbeek, M. & Voorst, J. V. Paramagnetic oxygen centres in $SrTiO_3$ induced by light. *Chem. Phys. Lett.* **20**, 92 – 95 (1973). URL http://www.sciencedirect.com/science/article/pii/0009261473852261.

[217] Shein, I. & Ivanovskii, A. First principle prediction of vacancy-induced magnetism in non-magnetic perovskite $SrTiO_3$. *Phys. Lett. A* **371**, 155 – 159 (2007). URL http://www.sciencedirect.com/science/article/pii/S0375960107008638.

[218] Li, Y.-L., Zhang, D.-N., Qu, S.-B., Yang, M. & Feng, Y.-P. The effect of oxygen vacancies on the electronic structures, magnetic properties and the

stability of $SrTiO_3$(001) surface. *Surf. Sci.* **641**, 37 – 50 (2015). URL http://www.sciencedirect.com/science/article/pii/S0039602815001119.

[219] Chen, L. *et al.* Enhancing the Curie temperature of ferromagnetic semiconductor (Ga,Mn)As to 200 K via nanostructure engineering. *Nano Lett.* **11**, 2584–2589 (2011). URL https://doi.org/10.1021/nl201187m.

[220] Noyan, I. C., Huang, T. C. & York, B. R. Residual stress/strain analysis in thin films by X-ray diffraction. *Crit. Rev. Solid State Mater. Sci.* **20**, 125–177 (1995). URL https://doi.org/10.1080/10408439508243733.

[221] Hytch, M. J., Snoeck, E. & Kilaas, R. Quantitative measurement of displacement and strain fields from HREM micrographs. *Ultramicroscopy* **74**, 131–146 (1998). URL https://doi.org/10.1016/S0304-3991(98)00035-7.

[222] Hytch, M. J., Purtaux, J.-L. & Penisson, J.-M. Measurement of the displacement field of dislocations to 0.03 å by electron microscopy. *Nature* **423**, 270–273 (2003). URL https://doi.org/10.1038/nature01638.

[223] Himcinschi, C. *et al.* Strain relaxation in nanopatterned silicon round pillars. *Appl. Phys. Lett.* **90**, 021902 (2007). URL https://doi.org/10.1063/1.2431476.

[224] Ramesh, V., Kikuchi, A., Kishino, K., Funato, M. & Kawakami, Y. Strain relaxation effect by nanotexturing InGaN/GaN multiple quantum well. *J. Appl. Phys.* **107**, 114303 (2010). URL https://doi.org/10.1063/1.3369434.

[225] Wenisch, J. *et al.* Control of magnetic anisotropy in (Ga, Mn)As by lithography-induced strain relaxation. *Phys. Rev. Lett.* **99**, 077201 (2007). URL https://doi.org/10.1103/PhysRevLett.99.077201.

[226] Gercek, H. Poisson's ratio values for rocks. *Int. J. Rock Mech. Min. Sci.* **44**, 1 – 13 (2007). URL http://www.sciencedirect.com/science/article/pii/S136516090600075X.

[227] Masys, S. & Jonauskas, V. A first-principles study of structural and elastic properties of bulk $SrRuO_3$. *J. Chem. Phys.* **139**, 224705 (2013). URL https://doi.org/10.1063/1.4840435.

[228] Raghunathan, A., Melikhov, Y., Snyder, J. E. & Jiles, D. C. Theoretical model of temperature dependence of hysteresis based on mean field theory. *IEEE Trans. Magn.* **46**, 1507–1510 (2010). URL https://doi.org/10.1109/TMAG.2010.2045351.

[229] Park, T.-J., Papaefthymiou, G. C., Viescas, A. J., Moodenbaugh, A. R. & Wong, S. S. Size-dependent magnetic properties of single-crystalline multiferroic $BiFeO_3$ nanoparticles. *Nano Lett.* **7**, 766–772 (2007). URL https://doi.org/10.1021/nl063039w.

[230] Lu, W. *et al.* The role of octahedral tilting in the structural phase transition and magnetic anisotropy in $SrRuO_3$ thin film. *J. Appl. Phys.* **113**, 063901 (2013). URL https://doi.org/10.1063/1.4790699.

[231] Jung, C. U., Yamada, H., Kawasaki, M. & Tokura, Y. Magnetic anisotropy control of $SrRuO_3$ films by tunable epitaxial strain. *Appl. Phys. Lett.* **84**, 2590–2592 (2004). URL https://doi.org/10.1063/1.1695195.

[232] Brown, W. F. Theory of the approach to magnetic saturation. *Phys. Rev.* **58**, 736–743 (1940). URL https://link.aps.org/doi/10.1103/PhysRev.58.736.

[233] Zhang, H., Zeng, D. & Liu, Z. The law of approach to saturation in ferromagnets originating from the magnetocrystalline anisotropy. *J. Magn. Magn. Mater.* **322**, 2375 – 2380 (2010). URL http://www.sciencedirect.com/science/article/pii/S0304885310001472.

[234] Hauser, H., Jiles, D., Melikhov, Y., Li, L. & Grössinger, R. An approach to modeling the dependence of magnetization on magnetic field in the high field regime. *J. Magn. Magn. Mater.* **300**, 273 – 283 (2006). URL http://www.sciencedirect.com/science/article/pii/S0304885305005354.

[235] Boschker, H. *et al.* Uniaxial contribution to the magnetic anisotropy of $La_{0.67}Sr_{0.33}MnO_3$ thin films induced by orthorhombic crystal structure. *J. Magn. Magn. Mater.* **323**, 2632 – 2638 (2011). URL http://www.sciencedirect.com/science/article/pii/S0304885311003283.

[236] Kanbayasi, A. Magnetocrystalline anisotropy of $SrRuO_3$. *J. Phys. Soc. Jpn.* **41**, 1879–1883 (1976). URL https://doi.org/10.1143/JPSJ.41.1879.

[237] Ogasawara, T. *et al.* General features of photoinduced spin dynamics in ferromagnetic and ferrimagnetic compounds. *Phys. Rev. Lett.* **94**, 087202 (2005). URL https://link.aps.org/doi/10.1103/PhysRevLett.94.087202.

[238] Landau, L., Reiner, J. W. & Klein, L. Low temperature magnetic force microscope study of magnetization reversal in patterned nanoislands of srruo3. *J. Appl. Phys.* **111**, 07B901 (2012). URL https://doi.org/10.1063/1.3673827.

[239] Gross, H., Bansal, N., Kim, Y.-S. & Oh, S. In situ study of emerging metallicity on ion-bombarded $SrTiO_3$ surface. *J. Appl. Phys.* **110**, 073704 (2011). URL https://doi.org/10.1063/1.3650254.

[240] Wu, X. D., Foltyn, S. R., Dye, R. C., Coulter, Y. & Muenchausen, R. E. Properties of epitaxial $SrRuO_3$ thin films. *Appl. Phys. Lett.* **62**, 2434–2436 (1993). URL https://doi.org/10.1063/1.109388.

[241] Kleibeuker, J. E. *et al.* Atomically defined rare-earth scandate crystal surfaces. *Adv. Func. Mater.* **20**, 3490–3496 (2010). URL https://onlinelibrary.wiley.com/doi/abs/10.1002/adfm.201000889.

[242] Dirsyte, R. *et al.* Impact of epitaxial strain on the ferromagnetic transition temperature of $SrRuO_3$ thin films. *Thin Solid Films* **519**, 6264 – 6268 (2011). URL http://www.sciencedirect.com/science/article/pii/S0040609011007905.

[243] Takahashi, K. *et al.* Effect of strain in epitaxially grown $SrRuO_3$ thin films on crystal structure and electric properties. *Jpn. J. Appl. Phys.* **41**, 5376–5380 (2002). URL https://doi.org/10.1143/JJAP.41.5376.

[244] Wang, Z. & Shapiro, A. Studies of $LaAlO_3$ "100" surfaces using RHEED and REM. I: twins, steps and dislocations. *Surf. Sci.* **328**, 141 – 158 (1995). URL http://www.sciencedirect.com/science/article/pii/0039602895000143.

[245] Podlesnyak, A. *et al.* Crystal-field and magnetic properties of the distorted perovskite $NdGaO_3$. *J. Phys.: Condens. Matter* **5**, 8973–8982 (1993). URL https://doi.org/10.1088/0953-8984/5/48/008.